Fakultät für Mathematik und Naturwissenschaften | RWTH AACHEN UNIVERSITY

Degradation and Failure Mechanisms of Gas Diffusion Electrodes for Electroreduction of CO_2 in Aqueous Electrolytes

Degradations- und Versagensmechanismen von Gasdiffusionselektroden für die Elektroreduktion von CO_2 in wässrigen Elektrolyten

Von der Fakultät für Mathematik und Naturwissenschaften der RWTH Aachen University zur Erlangung des akademischen Grades eines Doktors der Naturwissenschaften genehmigte Dissertation

vorgelegt von

Dipl.-Ing. Verena Theußl

aus

Deutschlandsberg, Österreich

Berichter: Univ.-Prof. Dr. rer. nat. Rüdiger-A. Eichel
Univ.-Prof. Dr. Ing. Matthias Wessling

Tag der mündlichen Prüfung: 17.12.2025

Diese Dissertation ist auf den Internetseiten der Universitätsbibliothek verfügbar.

This page is intentionally left blank.

“The future belongs to those
who believe in the beauty of their dreams"

Eleanor Roosevelt

This page is intentionally left blank.

Acknowledgement

At the outset of this thesis, I would like to express my heartfelt gratitude to all those who have supported me throughout this journey. Completing the thesis has been a long and sometimes challenging process, often giving rise to speculation about when it would finally be finished. Therefore, I am all the more grateful and proud to present this completed version.

First and foremost, I am sincerely grateful to **Prof. Dr. Rüdiger-A. Eichel** for the opportunity to conduct my research within IEK-9 (now IET-1**)**. His exceptional supervision and guidance played a vital role in shaping this dissertation. I also extend my sincere thanks to **Prof. Dr.-Ing. Matthias Wessling** for kindly agreeing to serve as the second reviewer and for his valuable contribution to evaluating this work.

I am especially thankful to the entire **Tempel Department**, who not only supported my academic progress but also enriched my experience through their collaboration and friendship. I would like to express my particular appreciation to **Dr. Hermann Tempel**, **Dr. Henning Weinrich**, and **Dr. Sergio Sanz Calvo** for their guidance, thoughtful advice, and consistent encouragement throughout the four years of my doctoral work.

My heartfelt thanks go to the **CO_2 electrolysis group**, with whom I shared not only fruitful scientific discussions but also many memorable moments during my time at IEK-9 (now IET-1). In particular, I would like to thank **Albert Luft** for his reliability, technical assistance, and good humour, especially when I found myself short on IC sample vials or needed help with GC and IC analyses. I am also grateful to **Dr. Burkhard Hecker**, **Bernhard Schmid**, and **Marcel Turiaux** for the engaging conversations and shared experiences in the laboratory and during social activities.

I would also like to thank my colleagues in **Building 09.7**—**Bastian, Kira, Christine, Fabian, Max,** and **Jule**—for their moral support and the countless moments that made this period not only productive but truly enjoyable. I also appreciate **Fabrizio Lisi's** contributions during his internship and the support from **Ansgar**, **Sebastian**, and **Christine** with the vapour sorption, TGA, and XCT measurements.

Finally, I would like to thank my family and friends for their constant encouragement and belief in me throughout this journey. In particular, my heartfelt thanks go to **Daniel**, whose patience, understanding, and unwavering support during the many late nights and weekends made this achievement possible. Your love was a steady source of strength and motivation.

To everyone who contributed to this work, in ways both large and small, thank you.

Declaration Statement

I, *Verena Theußl*,

declare that this thesis and the work presented in it are my own and have been generated by me as the result of my original research.

I do solemnly swear that:

1. This work was done wholly or mainly while in candidature for the doctoral degree at this faculty and university.
2. Where any part of this thesis has previously been submitted for a degree or any other qualification at this university or any other institution, this has been clearly stated.
3. Where I have consulted the published work of others or myself, this is always clearly attributed.
4. Where I have quoted from the work of others or myself, the source is always given. This thesis is entirely my own work, except for such quotations.
5. I have acknowledged all major sources of assistance.
6. Where the thesis is based on work done by me jointly with others, I have made clear exactly what others did and what I contributed.
7. Parts of this work have been published before as:
    a. Theußl, V. (corresponding author); Sanz, S.; von Foerster, K.; Weinrich, H., Rutjens, B., Tempel, H.; Eichel, R.-A., Electrochem. Sci. Adv., e202400014, **2024** *Special Issue*: Bridging the Gap – Advancing Electrochemical Power-to-X Technologies towards Industrial Applications. DOI: https://doi.org/10.1002/elsa.202400014
    b. Theußl, V. (corresponding author), Weinrich, H.; Lisi, F.; Tempel, H., Eichel, R.-A., RSC. *Sustainable Energy Fuels*, **2024**, 8, 1483–1494 DOI: https://doi.org/10.1039/D3SE01347B

c. Theußl, V. (corresponding author); Weinrich, H.; Heume, C.; Dzieciol, K.; Schmid, B.; Kungl, H.; Tempel, H.; Eichel, R.-A., ChemElectroChem, **2023**, *202300121* (10), 13, DOI: https://doi.org/10.1002/celc.202300121

Date Signature

Abstract

To counteract global warming, triggered by the rising levels of anthropogenic greenhouse gas CO_2 in the atmosphere, carbon capture and utilisation technology (CCU), which includes the electroreduction of CO_2, is a promising strategy. This technology not only valorises an otherwise harmful gas but also enables the closing of the anthropogenic carbon cycle, which could help to reduce the CO_2 levels in the atmosphere. Gas diffusion electrodes (GDE) play a central role in investigating the electroreduction of CO_2, as they ensure optimal contact between the catalyst, CO_2, and the electrolyte/ions, thereby defining an optimal reaction environment. To advance the technical maturity of the electroreduction of CO_2 to formate, this thesis investigates factors influencing the optimal reaction environment, i.e., wettability, degradation mechanisms, and cell structure, based on the electrode architecture.

This dissertation emphasises the importance of a microporous layer (MPL) for achieving relevant current densities and Faradaic Efficiencies (FE). The MPL influences the focus of the catalyst layer on the GDE surface, the wetting, and the electrical conductivity, leading to an improved interface between the catalyst, the electrolyte and CO_2. This improved catalyst interface enables obtaining relevant current densities and $FE_{Formate}$ >80%. The effects of the improved catalyst interface can only be exceeded by a high through-plane conductivity. In this context, the high through-plane conductivity even enables GDEs without MPL to achieve the highest FEs of all investigated GDEs (>90%), hence surpassing the obtained FE of GDEs with MPL. In addition to the MPL, the extent of the hydrophobic treatment is also decisive, as it determines the electrode wetting and the extent of the GDE/electrolyte interface. Hereby, in the case of GDEs without MPL, a lower hydrophobic treatment (10 % vs 30 % PTFE) was particularly advantageous for achieving high FEs.

Regarding the influence of the hydrophobic treatment on the GDE's durability and performance, early-stage performance changes were already apparent after 1 hour of CO_2 electroreduction. These changes manifested in catalyst agglomeration and loss of hydrophobicity. The latter is most probably triggered by

structural changes of the binder's side chains and/or sulfonic groups, indicating the unsuitability of the binder in the investigated setup. Interestingly, the increase of the catalyst loading improved the electrode performance only to a certain point, with a medium catalyst loading of 2.3 $mg \cdot cm^{-2}$ showing the best performance.

Various ion exchange ionomers were tested for their suitability to investigate further the influence of the loss of hydrophobicity and its prevention. The outcome indicates a relationship between the structural composition of the binder and the obtained cathodic current densities at –1.15 V_{RHE} and $FE_{Formate}$. The imidazolium-based binder Sustainion obtained stable $FEs_{Formate}$ >90% during repeated cycling due to the CO_2 affinity of the imidazolium structure. The stable FEs >90% obtained with Sustainion as a binder would possibly enable the transition from a gas-fed batch cell to a flow cell. However, in preceding tests with the flow cell, the increasing HER and the premature electrode flooding over time demonstrated its detrimental use. With certain adaptations to the GDE architecture, the addition of an MPL, and a change of binder to a mixture of Aemion + Nafion, comparable results were obtained between the gas-fed batch cell and the flow cell. This engineered GDE architecture was furthermore stable during a 6-hour operation.

Kurzfassung

Um der globalen Erwärmung entgegenzuwirken, die durch den steigenden Anteil des anthropogenen Treibhausgases CO_2 in der Atmosphäre verursacht wird, ist die Technologie der Kohlenstoffabscheidung und -nutzung (CCU), zu der auch die elektrische Reduktion von CO_2 gehört, eine vielversprechende Strategie. Diese Technologie wertet nicht nur ein ansonsten schädliches Gas auf, sondern ermöglicht auch die Schließung des anthropogenen Kohlenstoffkreislaufs, was dazu beitragen könnte, den CO_2-Gehalt in der Atmosphäre zu senken. Gasdiffusionselektroden (GDE) spielen bei der Untersuchung der Elektroreduktion von CO_2 eine zentrale Rolle, da sie einen optimalen Kontakt zwischen dem Katalysator, CO_2 und Elektrolyt/Ionen gewährleisten und somit eine optimale Reaktionsumgebung schaffen. Um die technische Reife der Elektroreduktion von CO_2 zu Formiat voranzutreiben, untersucht diese Dissertation Faktoren, die die optimale Reaktionsumgebung beeinflussen, d.h. Benetzbarkeit, Degradationsmechanismen und Zellstruktur, basierend auf der Elektrodenarchitektur.

In dieser Arbeit wird die Bedeutung einer mikroporösen Schicht (MPL) für das Erreichen relevanter Stromdichten und Faraday-Effizienzen (FE) hervorgehoben. Die MPL beeinflusst die Fokussierung der Katalysatorschicht auf der GDE-Oberfläche, die Benetzung und die elektrische Leitfähigkeit, was zu einer verbesserten Katalysatorgrenzfläche führt. Die verbesserte Katalysatorgrenzfläche ermöglicht das Erreichen relevanter Stromdichten und $FE_{s_{Formiat}}$ >80 %. Der Effekt der verbesserten Katalysatorgrenzfläche kann nur durch eine hohe Durchgangsleitfähigkeit übertroffen werden. In diesem Zusammenhang ermöglicht die hohe Durchgangsleitfähigkeit sogar GDEs ohne MPL, die höchsten FEs aller untersuchten GDEs (>90 %) zu erreichen und damit die FEs von GDEs mit MPL zu übertreffen. Neben der MPL ist auch der Grad der Hydrophobierung entscheidend, da dieser die Elektrodenbenetzung und die Größe der GDE/Elektrolyt-Grenzfläche bestimmt. Bei GDEs ohne MPL war eine geringere hydrophobe Behandlung (10 % vs. 30 % PTFE) besonders vorteilhaft für das Erreichen einer hohen FE.

Hinsichtlich des Einflusses der Hydrophobierung auf die Haltbarkeit und Leistung der GDE wurden bereits nach einer Stunde CO_2-Elektroreduktion erste Leistungsänderungen festgestellt. Diese Veränderungen äußerten sich in einer Agglomeration des Katalysators und einem Verlust der Hydrophobizität. Letzteres ist höchstwahrscheinlich durch strukturelle Veränderungen der Seitenketten und/oder der Sulfongruppen des Bindemittels zurückzuführen, was auf die Ungeeignetheit des Binders in der untersuchten Anordnung hinweist. Interessanterweise verbesserte eine Erhöhung der Katalysatorbeladung die Elektrodenleistung nur bis zu einem gewissen Punkt, wobei eine mittlere Katalysatorbeladung von 2.3 $mg \cdot cm^{-2}$ die beste Leistung zeigte.

Um den Einfluss des Hydrophobizitätsverlustes und dessen Verhinderung weiter zu untersuchen, wurden verschiedene Ionenaustauscher-Ionomere auf ihre Eignung getestet. Die Ergebnisse deuten auf einen Zusammenhang zwischen der strukturellen Zusammensetzung des Bindemittels und den erzielten kathodischen Stromdichten bei –1.15 V_{RHE} und den $FEs_{Formiat}$ hin. Das Imidazolium-Bindemittel Sustainion erzielte aufgrund der CO_2-Affinität der Imidazolium-Struktur stabile $FEs_{Formiat}$ von >90 % während wiederholter Zyklisierung, was den Übergang von einer gasgespeisten Batchzelle zu einer Durchflusszelle ermöglichen könnte. Die mit der Zeit zunehmende HER und die vorzeitige Elektrodenflutung in Vortests mit der Flusszelle zeigte jedoch, dass Sustainion als Binder nicht geeignet ist für den Einsatz in einer Durchflusszelle. Mit bestimmten Anpassungen an der GDE-Architektur, das Auftragen einer MPL und einem Wechsel des Binders zu einer Bindermischung aus Aemion + Nafion wurden vergleichbare Ergebnisse zwischen der gasgespeisten Batchzelle und der Durchflusszelle erzielt. Dabei konnte die konstruierte GDE-Architektur im Rahmen einer sechsstündigen Testphase ihre Stabilität unter Beweis stellen.

List of Publications

Parts of this thesis are based on the following publications:

Technological Advances in Electroreduction of CO_2-to-HCOOH: The Impact of Catalyst, Gas Diffusion Electrode, and Cell Design.[1]

Theußl, V.; Sanz, S.; von Foerster, K.; Weinrich, H., Rutjens, B., Tempel, H.; Eichel, R.-A., Electrochem. Sci. Adv., e202400014, **2024**

Special Issue: Bridging the Gap – Advancing Electrochemical Power-to-X Technologies towards Industrial Applications

DOI: https://doi.org/10.1002/elsa.202400014

Contributions: V. Theußl is one of the three main contributors to this publication. She wrote the part about the gas diffusion electrodes. The publication was written in consultation with S. Sanz and K. von Foerster. S. Lehmann contributed the graphical design for Figures 5 and 7.

In this thesis, parts of **Chapter 2** are based on this publication

Early-Stage Performance Changes of Gas Diffusion Electrodes for Electroreduction of CO_2 to Formate[2]

Theußl, V., Weinrich, H.; Lisi, F.; Tempel, H., Eichel, R.-A., RSC. *Sustainable Energy Fuels*, **2024**, 8, 1483-1494

DOI: https://doi.org/10.1039/D3SE01347B

Contributions: V. Theußl is the main contributor to this publication. She conducted the electrochemical and physicochemical characterisation methods. F. Lisi conducted parts of the electrochemical characterisation in the first part of this chapter. S. Ziemer conducted the TGA measurements, and A. Kretzschmar conducted the vapor sorption measurements. S. Lehmann contributed the graphical design for the graphical abstract of this publication. The publication was written in consultation with H. Weinrich.

In this thesis, **Chapter 4.2** is based on this publication.

Impact of the Carbon Substrate for Gas Diffusion Electrodes on the Electroreduction of CO_2 to Formate[3]

Theußl, V.; Weinrich, H.; Heume, C.; Dzieciol, K.; Schmid, B.; Kungl, H.; Tempel, H.; Eichel, R.-A., ChemElectroChem, **2023**, *202300121* (10), 13,

DOI: https://doi.org/10.1002/celc.202300121

Contributions: V. Theußl is the main contributor to this publication. She conducted the electrochemical and physicochemical characterisation methods. C. Heume conducted the XCT measurements. S. Lehmann contributed to the graphical design of Figure 22. The publication was written in consultation with H. Weinrich.

In this thesis, **Chapter 4.1** is based on this publication.

List of Conferences

Poster

Conference: Fuel Science: From Production to Propulsion, Aachen, Germany, June 22nd – 24th 2021
Title: Structural Analysis of SnO_2 nanoparticle coated Gas Diffusion Electrode for Electrochemical Reduction of CO_2

Conference: 4th Electra Symposium, Jülich, Germany, September 14th – 15th 2023
Title: Tuning the electrochemical CO_2-to-HCOO(H) reduction to improve selectivity and energy efficiency.

Talks

Conference: 8th Regional Symposium on Electrochemistry for South-East Europe, RSE-SEE 8, Graz, Austria, July 11th – 15th 2022
Title: Influence of the Carbon Substrate on the Electroreduction of CO_2 to Formate using various Gas Diffusion Layers.

Conference: 3rd Electra Symposium, Aachen, Germany, August 31st – September 01st 2022
Title: Gas Diffusion Electrode Development for Power-to-Formate.

Summer School

Joint European Summer School JESS, Week 1 – Introductory Modules, Module: Low-Temperature fuel cells and electrolysers (PEM and alkaline), September 07th– 11^{th,} 2020, Vouliagmeni, Athens, Greece

This page is intentionally left blank.

Contents

ACKNOWLEDGEMENT I
DECLARATION STATEMENT III
ABSTRACT V
KURZFASSUNG VII
LIST OF PUBLICATIONS IX
LIST OF CONFERENCES XI
CONTENTS XIII

CHAPTER 1 INTRODUCTION 1

1.1 MOTIVATION 1
1.2 SCOPE AND AIM OF RESEARCH 4
1.3 OUTLINE 5

CHAPTER 2 ELECTROREDUCTION OF CO_2: STATE OF THE ART 7

2.1 A GENERAL DESCRIPTION OF ELECTROREDUCTION OF CO_2 7
2.2 POWER-TO-FORMATE 9
2.3 CATALYST DESIGN 10
2.4 GAS DIFFUSION ELECTRODES 11
2.5 CELL DESIGN 22

CHAPTER 3 EXPERIMENTAL 27

3.1 PREPARATION OF GAS DIFFUSION ELECTRODES 27
3.2 CHARACTERISATION OF GAS DIFFUSION ELECTRODES 31
3.3 ELECTROCHEMICAL CHARACTERISATION 35
3.4 PRODUCT ANALYSIS 38
3.5 REPRODUCIBILITY OF THE MEASUREMENTS 40

CHAPTER 4 RESULTS AND DISCUSSION 43

4.1 IMPACT OF CARBON SUBSTRATE FOR GAS DIFFUSION ELECTRODES ON THE ELECTROREDUCTION OF CO_2 TO FORMATE 43
4.2 EARLY-STAGE PERFORMANCE CHANGES OF GAS DIFFUSION ELECTRODES FOR ELECTROREDUCTION TO FORMATE 72
4.3 IMPACT OF THE BINDER MATRIX ON GAS DIFFUSION ELECTRODES FOR CO_2 ELECTROREDUCTION TO FORMATE 91
4.4 INVESTIGATION OF THE INFLUENCE OF THE CELL SETUP: OUTLOOK FOR FUTURE EXPERIMENTS 106

CHAPTER 5 CONCLUSION 114

CHAPTER 6 BIBLIOGRAPHY 119

APPENDIX 131

COPYRIGHTS OF FIGURES AND TABLES 135
LIST OF ABBREVIATIONS 139
LIST OF FIGURES 141
LIST OF TABLES 146
CURRICULUM VITAE 147
..... 147

This page is intentionally left blank.

Chapter 1
Introduction

1.1 Motivation

The beginning of the Industrial Revolution signified a substantial enhancement in the quality of life for humanity. Concurrently, it precipitated a precipitous rise in anthropogenic CO_2 emissions, which accumulated in the atmosphere. These elevated levels of CO_2, a by-product of human activity, served to exacerbate the greenhouse effect, thereby inducing the observed global warming and climate change. The consequences of climate change are far-reaching, including a decline in agricultural productivity and disruption to global food supplies, which endangers food security, health, and social stability.[4] In response to this challenge, the United Nations Conference on Climate Change (UNCCC) held in Paris in 2015 established a target to limit the increase in global temperatures to well below 2°C by the year 2050.[5]

Several strategies are currently available to achieve this target, including deploying alternative renewable energies to avoid the emission of anthropogenic CO_2 into the atmosphere and improving the energy efficiency of existing systems. Another strategy, probably the easiest, would be the capture and sequestration of anthropogenic CO_2. This technology facilitates the use of fossil fuels in processes that, until now, have not been suitable for renewable energy sources and, in turn, enables the storage of CO_2 for subsequent utilisation. Certain technologies can benefit from the storage of CO_2, as illustrated in **Figure 1**, which enables the closure of the anthropogenic carbon cycle and may even help to diminish the harmful environmental effects caused by the high CO_2 concentration levels in the atmosphere, thus helping to mitigate global warming.[6–10] Currently available carbon utilisation technologies range from electrochemical and photoelectrochemical reduction of CO_2 and biological conversion to thermally driven CO_2 hydrogenation systems.

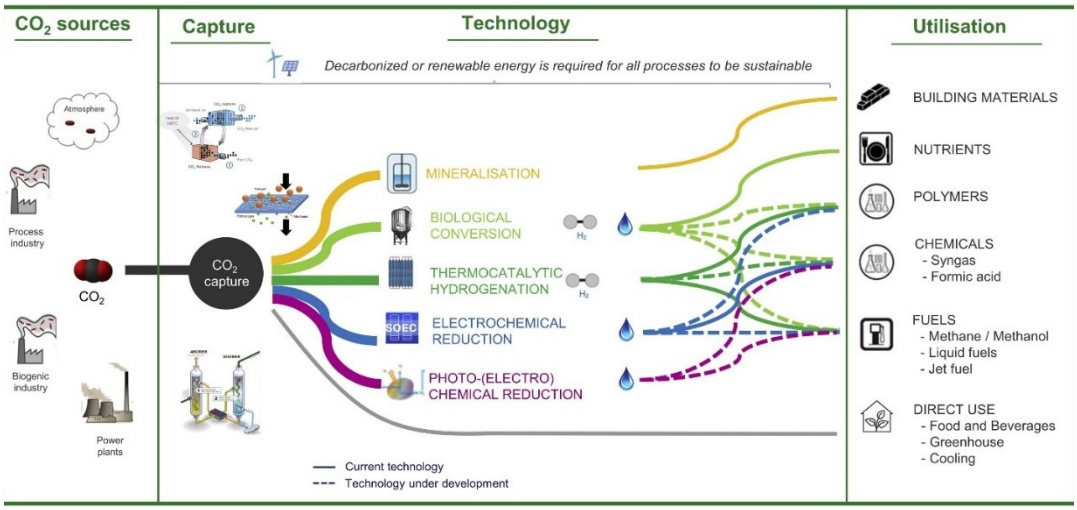


Figure 1. Carbon Capture and Utilisation technologies for the valorisation of the greenhouse gas CO_2. Reproduced from [10] with permission from Elsevier.

These technologies facilitate the valorisation of otherwise harmful CO_2 into valuable products such as polymers, building materials, or chemicals (**Figure 1**).[10,11] The electroreduction of CO_2 is particularly interesting as it enables the use of renewable energy to produce fuels that can be stored and utilised during periods of limited renewable energy availability. Furthermore, it closes the anthropogenic carbon cycle and facilitates a synthesis route for base chemicals to be employed in the chemical industry. The electroreduction of CO_2 not only valorises the harmful CO_2 but also contributes to mitigating global warming.

Despite the numerous advances and novel approaches witnessed in recent decades, the electroreduction of CO_2 remains a challenging process. The challenges arise from high overpotentials,[12] low solubility of CO_2 in aqueous electrolytes, and electrode degradation.[13] Problems arising due to the low solubility of CO_2 in aqueous electrolytes, accompanied by the low diffusion coefficient of dissolved CO_2, can be overcome using gas diffusion electrodes (GDEs). They enable the direct feed of CO_2 to the catalyst layer, circumventing the solubility step and diffusion to the catalyst necessary in other electrode designs. However, GDEs are susceptible to electrode degradation and associated low lifetime despite the advanced state of GDE technology in other electrochemical processes, including chlorine-,[14–16] PEM-[17–19] and water electrolysis.[20–22] The impaired GDE's lifetime stems most probably from their bifunctional nature, complicating a direct comparison with GDEs for

other electrochemical processes. A comparison with water electrolysis highlights the differences in product formation: in water electrolysis, the products are initially formed in the liquid phase and depending on the local mass transfer situation and surface properties of the electrode, an oversaturation and, hence, bubble formation can occur. In contrast, the electroreduction of CO_2 necessitates the diffusion of the gaseous reactant to the catalyst layer and its direct binding to the catalyst at the triple-phase boundary before electrochemical conversion. Furthermore, it leads to product formation not only in one physical state, such as in water electrolysis, but in two: liquid and gaseous.[2,20,23] Additionally, the nature of the liquid CO_2 electroreduction products, formic acid and ethanol, alters surface wetting due to their low surface tension, possibly leading to severe damage and limited lifetime, e.g. electrode flooding.[24]

A further reason for the limited lifetime of GDEs is that most studies found in the literature have concentrated exclusively on catalyst designs and enhancements. However, there is a lack of systematic studies on GDEs, cell designs, and the overall impact of the reaction environment. A review[25] of literature published between 2010 and 2022 revealed a paucity of studies focusing on developing an optimal electrode and cell design, with a recent surge of interest in this area (**Figure**

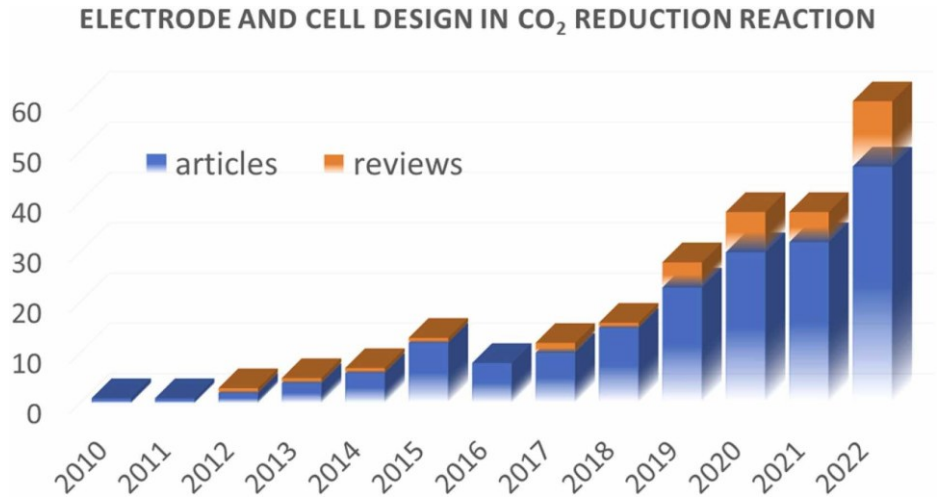


Figure 2. The number of articles published between 2010 and 2022 investigating suitable electrode- and cell designs. The following keywords were used by the authors of the article to review the data in the Scopus Database: CO_2 reduction, electrode- and cell design. Reproduced from [25] enabled by the Creative Commons CC-BY license (https://creativecommons.org/licenses/by/4.0/).

2). However, these investigations are essential to achieve technical maturity at industrially relevant conditions, i.e., high current densities >300 $mA \cdot cm^{-2}$ [26] and high FEs. The present dissertation, therefore, aims to establish a deeper understanding of how electrode properties can influence the optimal reaction environment for the electroreduction of CO_2 to formate. Furthermore, the failure and degradation mechanisms have been investigated to develop enhanced GDE stability in response to these mechanisms.

1.2 Scope and Aim of Research

The literature about the electroreduction of CO_2 to formate is replete with studies about the design and development of catalysts. However, there has been a recent shift in focus towards GDE architecture and cell design, with an increasing number of researchers recognising the significance of systematic studies on these aspects. These studies have revealed that the GDE architecture and cell design have a more significant impact on catalyst activity than improper catalyst design alone. It is imperative to emphasise the technical maturity of GDEs for the electroreduction of CO_2 to be operated at industrially relevant conditions (high current densities and long lifetimes), necessitating a comprehensive investigation of the entire reaction environment. The GDE architecture is of particular importance as it defines the reaction environment for the catalyst and can create an optimal interface between CO_2, catalyst, and electrolyte. The present dissertation aims to deepen the knowledge about the influencing factors of the reaction interface, i.e. wettability, degradation mechanisms and cell structure based on the electrode architecture to enhance the reaction environment for the electroreduction of CO_2 to formate. This is especially important as there are currently no systematic studies to investigate the reaction environment of GDEs, especially regarding the electrode architecture and the mechanisms impairing the stability and lifetime of the GDE.

The objective of this dissertation can, therefore, be addressed in the following steps:

- a systematic investigation of GDE properties based on its composition,
- deepen the knowledge about how the individual GDE properties can influence the electrode performance in terms of average electrode potential and FE,
- develop a knowledge-based optimisation strategy for GDEs to counteract any possible failure mechanisms.

1.3 Outline

The results presented in this dissertation were obtained in the period from March 2020 to February 2024 at the Institute of Energy and Climate Research – Fundamental Electrochemistry (IEK-9, now Institute for Energy Technologies IET-1) in the department of Dr Tempel at Forschungszentrum Jülich. With financial support from the German Federal Ministry of Education and Research within the project 'iNEW – Inkubator Nachhaltige Elektrochemische Wertschöpfungsketten'.

The present dissertation addresses several issues pertaining to the lifetime and the mechanisms impairing GDEs, as well as the suitable architecture for the electroreduction of CO_2 to formate. It begins with a comprehensive literature review and state-of-the-art analysis in **Chapter 2,** providing a detailed overview of the electroreduction of CO_2 in general, along with an examination of the factors influencing the reaction environment at the GDE interface and cell setups. **Chapter 3** presents the methodology employed in this dissertation, focusing on the electrochemical analysis procedure and the ex-situ analysis of the investigated GDEs. The results obtained over a four-year period are presented and discussed in **Chapter 4.** The discussion commences in **Chapter 4.1** with an investigation into the impact of the carbon substrate for GDEs on the electroreduction of CO_2 with GDLs from two manufacturers (Freudenberg GmbH & Toray Carbon Paper). The GDLs are then analysed concerning the influence of the presence of a microporous layer (MPL), the amount of the hydrophobic treatment and the thickness of the GDL. In **Chapter**

4.2, early-stage performance changes of GDEs for CO_2 electroreduction to formate are investigated based on the influence of the catalyst loading. **Chapter 4.3** systematically investigates how the binder matrix can influence the reaction environment at the GDE and the resulting FEs. **Chapter 4.4** emphasises the importance of the cell setup on the performance of the electrodes, i.e. average electrode potential and FE. The dissertation concludes with **Chapter 5**, which summarises the results and discussions about GDEs for the electroreduction of CO_2 to formate and prospects for further investigation of GDE. The additional **Appendix** provides supplementary information necessary for the discussion in the respective chapters.

Chapter 2

Electroreduction of CO_2: State of the Art

2.1 A General Description of Electroreduction of CO_2

The first pioneer work in the field of CO_2 electroreduction started as early as the late 19th century,[27,28] but only until the classification by Hori et al., the starting point of today's research, was established.[29] The electroreduction of CO_2 consolidates a promising approach, substituting synthesis modes for various base chemicals (CO, formic acid, methanol, etc.) from fossil fuel-based to renewables. Sixteen different carbon products can be obtained from this synthesis mode. The main classification can thereby be implemented according to the desired product and divided into three main groups: CO_2-to-carbon monoxide (CO), CO_2-to-formic acid/formate ($HCOOH/HCOO^-$) and CO_2-to-C_{2+} products, the latter covering sought-after products such as ethanol and higher alcohols, ethylene, acetaldehyde and propylene. The required electrocatalysts for the first group (CO_2-to-CO) include late transition metals like Au, Ag and Zn (depicted in blue in **Figure 3**). For the second group (CO_2-to-$HCOOH/HCOO^-$), the main group metals, such as Sn, In, and Bi, are active (green blocks in **Figure 3**). For the third group (CO_2-to-C_{2+}), Cu is the only pure

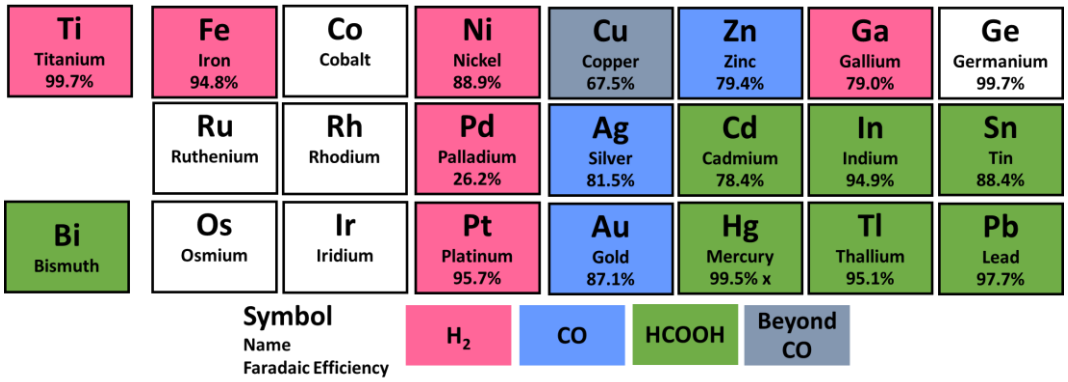


Figure 3. Elements active for the CO_2 electroreduction in a cropped periodic table. Elements in blue are active for CO_2-to-CO, green for CO_2-to-HCOOH, and grey for the CO_2-to-C_{2+} product fraction. In pink is the HER active group. Figure 3 is adapted from reference [30] and reproduced with permission from Wiley.

metal element reducing CO_2 with considerable selectivity to ethanol, ethylene, and C_2/C_3 products (depicted in grey in **Figure 3**).[11,29,30] A further classification element for CO_2 electroreduction is the number of transferred electrons during the electroreduction reaction, which is a multi-step process, and therefore, depending on the number of electrons transferred. Thereby, at the cathode side, the CO_2 is reduced to the desired products as a function of the electrocatalyst, while at the anode side, water is oxidised to oxygen via the oxygen evolution reaction (OER). **Table 1** lists the electroreduction products with the related standard electrode potentials (E^0) vs RHE, the number of electrons required during the reaction (z) and the reaction equations. The required electrons for the CO_2 electroreduction range from a two-electron transfer, which produces CO and HCOOH, to a six-electron transfer resulting in methanol, an eight-electron transfer to produce methane and a twelve-electron transfer with which ethanol and ethylene are produced.[31]

Table 1. List of CO_2 electroreduction products with their respective cathode reaction, number of electrons exchanged (z) and standard reaction potential (E^0). E^0 values are reported in aqueous media under standard conditions: 1 atm and 25°C.[32]

Product	**Cathode Reaction**	**z**	**E^0 / [V_{RHE}]**
H_2	$2\ H_2O + 2e^- \rightarrow H_2 + 2\ OH^-$	2	0.00
HCOOH	$CO_2 + 2\ H_2O + 2e^- \rightarrow HCOOH + 2\ OH^-$	2	–0.25
CO	$CO_2 + 2\ H_2O + 2e^- \rightarrow CO + 2\ OH^-$	2	–0.11
CH_3OH	$CO_2 + 5\ H_2O + 6e^- \rightarrow CH_3OH + 6\ OH^-$	6	0.02
CH_4	$CO_2 + 6\ H_2O + 8e^- \rightarrow CH_4 + 8\ OH^-$	9	0.17
C_2H_4	$2\ CO_2 + 8\ H_2O + 12e^- \rightarrow C_2H_4 + 12\ OH^-$	12	0.06
C_2H_5OH	$2\ CO_2 + 9\ H_2O + 12e^- \rightarrow C_2H_5OH + 12\ OH^-$	12	0.08

Comparing E^0 listed in Table 1, it attracts attention that the undesired parasitic hydrogen evolution reaction (HER) will always occur alongside the desired electroreduction of CO_2, which is also true for the CO production as a side reaction, making the proper design of the reaction environment (catalyst, GDE and cell design) even more critical.[31,33]

The main target of this dissertation will be the investigation of the electroreduction of CO_2 to formate, the respective salt of formic acid, as the production of formic acid/formate is pH dependent. Formate will be named as a representative of both formic acid and formate in this chapter.

2.2 Power-to-Formate

Methanoic acid, more commonly known as formic acid, is the simplest carboxylic acid, a colourless, corrosive liquid with a pungent odour. Its name is derived from ants (lat. Formica), from which it was first obtained by dry distillation.[34] Among the CO_2 electroreduction products, formate is next to CO, one of the easiest targets, as only two electrons are needed to implement CO_2 electroreduction.[35] Moreover, formate is a particularly profitable product, given its capacity to be produced with high faradaic efficiencies using inexpensive, earth-abundant metals that exhibit high overpotentials for H_2 production. Further, its liquid nature facilitates easy storage and distribution within existing infrastructures, enhancing economic viability. Hence, the electroreduction of CO_2 to formate is a promising synthesis route in contrast to the conventional route via methyl formate hydrolysis, which demands substantial energy requirements. Moreover, the conventional synthesis route is heavily reliant on fossil fuels, as the required CO for the carbonylation of methanol in the initial step of the synthesis route ($CO + CH_3OH \rightarrow HCOOCH_3$) is currently obtained from steam reforming, partial oxidation of fossil feedstocks or the gasification of coal. A slow reaction rate and undesirable byproducts further impair the conventional route. Consequently, the CO_2 electroreduction to formate becomes an even more viable synthesis route, particularly in combination with renewable

energy sources, with which electricity prices could be optimised. However, achieving economies of scale is the key factor to ensuring industrial viability. [36–38]

Concerning formate utilisation, global formate production has shown a linear growth in the past years. In 2022, global production was around 750 thousand tonnes, and according to forecasts, it is projected to increase further to 1300 thousand tonnes by 2035.[39] The primary applications of formate are diverse, encompassing the textile industry and leather tanning as well as pharmaceuticals, crop protection and its use as a de-icing agent for aircraft. Notwithstanding, the most promising application is as a hydrogen carrier or as a fuel for the direct formic acid fuel cell (DFAFC). Significantly, the application as a liquid hydrogen carrier is quite promising since formic acid has a volumetric H_2 capacity of 53.4 g H_2/L [40], which is equivalent to an energy density of 1.77 kWh/L, and this amount exceeds the commercial 70 MPa hydrogen pressure tanks (e.g. 1.4 kWh/L for the Toyota Mirai).[41] This makes formate more than suitable for the application as a H_2 carrier for automotive and mobile applications. Further, formate is a non-toxic, environmentally friendly, benign liquid with low flammability under ambient conditions. This renders it, in contrast to H_2, methane and ammonia, more favourable for storage as neither pressurised storage tanks nor cooling in expensive storage tanks is needed, and the existing gasoline infrastructure may be easily adapted for distribution.[36]

2.3 Catalyst Design

The design of suitable catalysts for the electroreduction of CO_2 to formate is a major focus for many research groups, ranging from material design to elucidating possible reaction mechanisms.[42–47] The central topic of this dissertation, however, is the investigation of GDEs and the associated degradation and failure effects. This chapter, therefore, only presents a brief discussion on the utilisation of Sn-based materials for the CO_2 electroreduction reaction to formate compared to the alternative potential catalysts (Pb, Bi, Cd, Tl, Hg, In).

Among the catalysts for CO_2 electroreduction to formate, Sn- and Bi-based materials are not only the most frequently investigated ones but also the most promising. Sn is a comparatively inexpensive, non-toxic material, abundant in the Earth's crust and environmentally benign. In addition, Sn-based catalysts have the highest selectivity for formate production. The major drawback, however, of these catalysts is their high overpotential and susceptibility to degradation mechanisms. Addressing these challenges necessitates implementing targeted catalyst design strategies, encompassing alloying, creating porous structures or defects, and two-dimensional engineering.[47–55] While the Bi-based catalysts tend to have a higher stability,[56,57] the target investigation of occurring degradation mechanisms is harder to achieve on a reasonably small time scale. Hence, Sn-based catalysts appear to be the optimal option for investigating potential degradation and failure mechanisms during the electroreduction of CO_2 to formate.

2.4 Gas Diffusion Electrodes

This chapter is based on the publication "*Technological Advances in Electroreduction of CO_2-to-HCOOH: The Effect of Catalyst, Gas Diffusion Electrode, and Cell Design"* by Theußl et al., published in October 2024 in *Electrochemical Science Advances*. The author's contribution is shown in the publication list. This publication is published under a CC-BY 4.0 license. S. B. C. Lehmann contributed the graphical design for **Figure 5** and **Figure 7**.

GDE: Fundamentals and Introduction

In the last decades, the research in CO_2 electroreduction has mainly focused on synthesising active and selective catalysts. However, the classical cell setups commonly employed to investigate these materials are constrained by the low diffusion coefficient of the dissolved CO_2 in the bulk electrolyte.[58] These factors hinder the sufficient availability of CO_2 on the catalyst surface, leading to a CO_2-starved catalyst layer and a favoured parasitic HER as a side reaction. Furthermore, it restricts the achievable current densities to a few mA cm^{-2},[59] which considerably lags behind

the high current densities (> 300 mA cm^{-2}) necessary for industrial application.[26] To overcome these diffusion and mass transport limitations, GDEs can be used due to their unique structure.[3] GDEs enable the direct feeding of the CO_2 gas to the catalyst layer, facilitating reactant transport and distribution while enhancing CO_2 electroreduction through their unique multilayer configuration.[59] The first two layers of a GDE are called the gas diffusion layer (GDL), and only when the catalyst is added on top does it become a complete GDE. The material of a GDL can consist not only of carbonaceous materials[60–62] but also of metals[63] or polytetrafluoroethylene (PTFE).[64] In carbonaceous-based GDEs, [2,3,65,66] the multilayer structure consists of i) the carbon fibres, ii) an optional MPL, and most importantly, iii) the catalyst layer. A schematic representation of a GDE can be seen in **Figure 4**.

GDEs: Individual Influencing Parameters of the Composition

Delving into discussing the individual parts of a GDE. The gas diffusion layer (GDL), i.e. carbon fibre substrate, as the first layer of a GDE (first layer in **Figure 4**), is not only the bearer of the catalyst layer but can also promote the whole electroreduction of CO_2 with its individual structure and morphology. The GDL is responsible for the efficient transport of CO_2 gas to the catalyst layer, ensuring its mechanical stability and participates in water management.[61] There are, in general, two types of carbon-based GDLs: single-layer and dual-layer. The single-layer GDL consists only of the carbon fibre substrate, while dual-layer GDEs have an additional microporous layer (MPL) on top of the fibres, shown as the middle layer in **Figure 4**. Typically, the carbon fibres and the MPL are composed of carbon and some hydrophobic treatment. Across the different GDE layers, PTFE is commonly employed to prevent

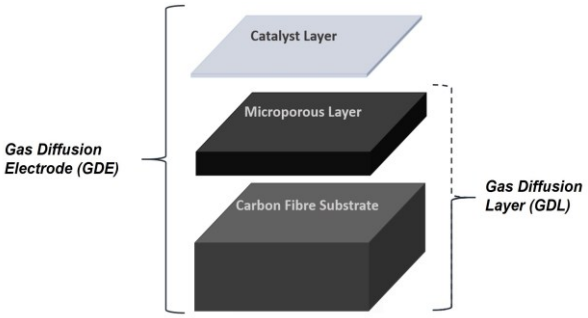


Figure 4. Schematic representation of the investigated gas diffusion electrodes (GDEs) based on a commercial gas diffusion layer (GDL). Reproduced from [3], enabled by the Creative Commons CC-BY license (https://creativecommons.org/licenses/by/4.0/).

early electrode flooding. The additional MPL on top of the carbon fibres is among the various components of the multilayer structure of a carbonaceous-based GDE of particular importance. Its presence can reduce the contact resistance between the carbon fibres and the catalyst layer by forming a flat and strong interfacial layer. Conversely, coating the catalyst directly onto the carbon fibres might lead to irregularly distributed particles.[33] Further, the MPL is the first defence line against electrode flooding, as a high surface tension of the liquid-gas-solid interface exists within the pores.[67–69] In a recent study, it was observed how the presence of a MPL enhances both the cathodic current density at −1.15 V_{RHE} during linear sweep volt-

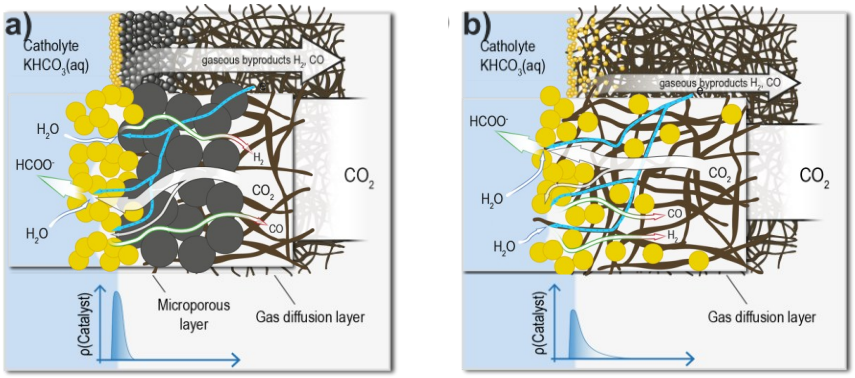


Figure 5. Schematic illustration of the reaction conditions at the investigated gas diffusion electrodes (GDEs) surface, displaying an enlarged depiction as an inset. (a) GDE with a microporous layer (MPL) that leads to a focused catalyst layer on the GDE surface. (b) GDE without MPL, thus, missing physical barrier for the catalyst nanoparticles (SnO_2, shown in yellow colour) during the GDE manufacturing. Reproduced from [1], enabled by the Creative Commons CC-BY license (https://creativecommons.org/licenses/by/4.0/).

ammetry (LSV) and the FE compared to GDEs without one.[3] These findings revealed that the MPL acts as a physical barrier for the nanoparticles during deposition, leading to a focused catalyst layer on top of the GDE and enhanced contact with the electrolyte (**Figure 5 a**). However, the open structure of the GDEs without MPL leads to deep penetration of the catalyst nanoparticles into the inner GDL volume. As a result, some catalyst nanoparticles were positioned beyond the reach of the electrolyte (**Figure 5 b**), leading to lower FE.[61,67,70]

While these GDLs are mainly optimised in other electrochemical fields, they still need improvement in CO_2 electroreduction, as the optimal conditions in terms

of process temperature, presence of physical water, CO_2 and carbonate/bicarbonate ions differ vastly from other electrochemical reactions and reactors. Even within the field of electroreduction of CO_2, the requirements of the GDEs can vary due to the divergent properties of the product range, which encompasses gases and liquids, lowering the surface tension to various extents. In literature, several aspects have already been investigated regarding thickness and wet proofing of the carbon fibres and the MPL,[61,67,70,71] but are mainly for the electroreduction of CO_2-to-CO. As stated here,[67] they found the suitable wet proofing of MPL and carbon fibres to be at 20 wt.% and 10 wt.% PTFE, respectively. Exceeding these amounts results in lower catalytic activity, as manifested in lower achievable current densities. Further, they showed that, in their case, the optimal thickness of the carbon fibres was 190 µm, whereas a higher thickness led to lower activity due to the prolonged diffusion length of CO_2 to the catalyst layer. At the same time, the thinnest GDL led to premature electrode flooding. A systematic screening of GDLs for high-performance CO_2 electrolysis to CO[61] showed that GDLs with the additional MPL achieved high FEs (>90%) in contrast to the GDLs without one. This could be attributed to two reasons. First, the PTFE in the MPL created a hydrophobic microenvironment, and second, an increased contact area between CO_2 and the catalyst led to a homogenous high surface area. However, the amount of the hydrophobic treatment had no significant effect on the selectivity of the electroreduction reaction. In CO_2 electroreduction to formate, PTFE is an unsuitable binder, as it imparts hydrophobicity but lacks ionic character. Besides, to produce liquid products, a certain wettability of the electrode is essential for its performance, which will be discussed in more detail in the section on electrode wettability.

As for the influence of the GDL on the electroreduction of CO_2 to formate, similar effects are valid for the role of the binder in the catalyst layer. Different binders can be more suitable for CO_2 electroreduction to formate than for CO and other evolving products. The role of the binder in the catalyst layer is, in general, to anchor the catalyst particles onto the GDL and create hydrophobic passages to provide CO_2 access to the catalyst layer. However, next to the anchoring part of binders, these with ionic character are utilised for CO_2 electroreduction, as they can

promote the reduction reaction itself. The binder should create an optimum microenvironment with a film of electrolyte within the catalyst layer pores, which is thick enough to maintain the ionic conductivity within the catalyst layer and thin enough to minimise the CO_2 transport resistance to the catalyst. Thus, a balance between hydrophobic and hydrophilic parts in the GDE needs to be achieved with the help of the binder for an optimum microenvironment.[72] Literature showed that binders with ionic character are preferable in the case of the electroreduction of CO_2 to formate.[73,74] They improve the CO_2 availability and adsorption of the key reaction intermediates by creating a hierarchical catalyst layer design with an ionomer interface, leading to a reduction of the undesired HER.[75,76]

Regarding the classification of the ionic binders, two groups are present: anion exchange and cation exchange ionomers. As the name already describes, the ionomers can exchange either anions (anion exchange ionomer) or cations (cation exchange ionomer). The transport mechanisms of the ions through the binder/membrane are based on two transport mechanisms: vehicle transport and Grotthuss hopping. Vehicle transport is a molecular diffusion process, where hydrated protons or hydroxide ions aggregate and move through the aqueous environment as a single entity based on a gradient movement triggered by a concentration or an electrical potential gradient. The Grotthuss hopping can be described as a structure diffusion, where protons are transferred via a hydrogen bond network of water molecules via formation and cleavage of covalent bonds with the neighbouring molecules, followed by reorientation of the water dipoles.[77–79] In the case of the cation exchange membranes/ionomers, a third transport mechanism is apparent: proton hopping along the sulfonic acid groups that line the pore wall.[80]

GDEs: How to prepare and what to consider

The investigated GDEs play a pivotal role in the electroreduction of CO_2, as the performance and durability of the electroreduction reaction strongly depend on the processes occurring at the catalyst-electrolyte interface.[81] Thereby, the proper catalyst layer preparation method of the GDEs significantly influences the occurring process at the electrode-electrolyte interface, as with it a suitable interface by

forming microchannels and microstructures containing a thin electrolyte layer, ensuring sufficient gas supply and electrolyte-catalyst contact is provided.[82] Thus, this significantly spotlights the investigation of the influence of the immobilisation methods of the required catalysts on the GDEs.

To achieve a well-defined catalyst layer and a uniform distribution of particles, several catalyst coating methods have already been established and can be divided into two groups: ink-based and ink-free. With the ink-based methods, a catalyst ink is commonly prepared before deposition. One of the advantages of the ink-based method is the wide variety of compositions of the catalyst layer. Methods to prepare the catalyst layer include spray deposition,[2,62,83] screen- [84–86] and roll printing.[87,88] The ink-free techniques, on the other hand, for instance, electrodeposition[89–91], sputter deposition[92–94] and dry-pressing method[95–97] allow for lower catalyst loadings and enable uniform distribution without the need for an (ionic) binder.[82,98]

In two studies,[81,99] ink-based methods were compared to determine the influence of the catalyst deposition methodology on the electrode performance. Both studies stated spray deposition methods as the most suitable catalyst coating method, yielding the most uniform catalyst layers and the lowest number of agglomerates. Furthermore, spray deposition methods even enable better control of the structure of the deposited catalyst layer, making this method an excellent tool for scalability up to large electrodes.[81,82,100] Moreover, the effortless adaptability of the catalyst ink in ink-based methods enables a fast counteract to possibly occurring effects during the electroreduction of CO_2 (electrode flooding, etc.). Thus, the composition of the catalyst layer not only improves the whole reduction reaction with its influence on the mass transport of reactants and products through the catalyst layer but also determines the concentration of the gaseous reactants on the catalyst layer, formation of triple-phase interfaces, and the morphology, ohmic resistance and electrical conductivity of the catalyst layer.[82,101–104]

GDE: From wettability and other influencing parameters on the electroreduction of CO_2 to formate

Another aspect influencing the GDE performance, directly related to the properties of the individual GDE layers (carbon fibres, MPL, and catalyst layer), is the GDE's wettability. In general, the wettability of the GDE describes the state of the optimal equilibrium between hydrophilic and hydrophobic states in the junction between the catalyst layer and the electrolyte. The significance of this optimal equilibrium between hydrophilic and hydrophobic states, e.g. an optimised microenvironment, can be explained by the diffusion paths available for the CO_2 molecule to the catalyst layer, depicted in **Figure 6**. The initial step involves the diffusion of CO_2 towards the catalyst layer. Now, three scenarios emerge to represent the appearance of the GDE: 1) most of the passages are hydrophobic, and the CO_2 adsorbs to the dry catalyst surface (dry region in **Figure 6**), representing an unoptimised state, as the required protons for the electroreduction of CO_2, from the electrolyte, might not be accessible. 2) An equilibrium between the hydrophilic and hydrophobic states is present, where the CO_2 molecule can adsorb on the liquid surface. With the adsorption on the liquid surface, a concentrated film of solvated CO_2 molecules is apparent, enabling the CO_2 to diffuse across this film to the catalyst layer, describing the

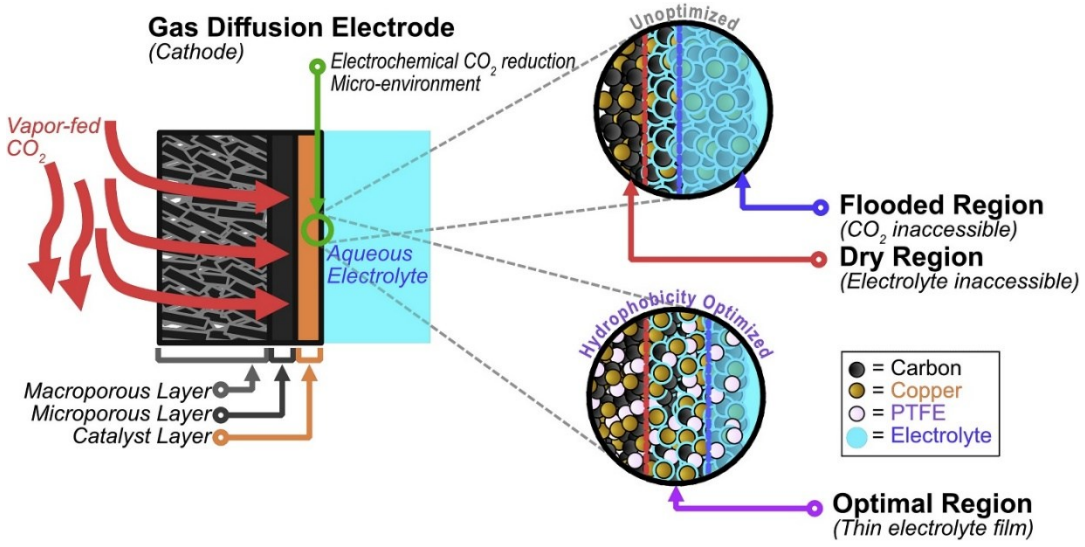


Figure 6. Schematic depiction of a GDE with two representative operating states during CO_2 electroreduction: unoptimised (top) and optimised (bottom). The schematic is reused from [106] with permission from Elsevier.

optimal region of the GDE in **Figure 6**, allowing for fast gas and electron transport, providing sufficient supply and shortened distances of CO_2, hence achieving low overpotentials and high FEs and stability at commercially relevant current densities.[105] 3) The third scenario describes the diffusion through the electrolyte-flooded pores, representing another unoptimized state of **Figure 6**, mainly occurring in the flooded regions of the GDE, a common mechanism occurring in flow cells, impairing the electrode performance.[23,106]

The equilibrium state between the hydrophobic and hydrophilic parts within the GDE pores can also be related to the often-used description of an existing triple-phase boundary.[105] The triple phase boundary is the widely used term for describing an optimal reaction condition for the CO_2 electroreduction reaction, as all three phases (gas-liquid-solid) in the form of CO_2, electrolyte, and catalyst are present at the same interface. This description dates back to the H_2 fuel cell, as in the field of CO_2 electroreduction, many descriptions were adopted from other electrochemical fields, i.e. fuel cells and batteries, due to the later start of investigations regarding CO_2 electroreduction.[23] However, in a publication about liquid-solid boundaries affecting the activity of CO_2 electroreduction,[23] the authors distinguished between a triple-phase and a double-phase boundary. In the atomistic context, the triple phase boundary describes the direct binding of gaseous CO_2 to the catalyst at the gas-liquid-solid junction. In contrast, at the atomistic double-phase boundary, CO_2 electroreduction occurs similarly as in an H-cell, where the CO_2 gas diffuses to the liquid and is reduced at the liquid-solid interface. Assuming the catalyst is always surrounded by a film of water/electrolyte due to its rather hydrophilic characteristic, the atomistic double-phase boundary is most likely responsible for the reactivity of the CO_2 electroreduction reaction. Additionally, with flooded GDE pores, CO_2 electroreduction can also be maintained; if triple-phase boundaries were the only reaction zones, this would be unfeasible.[107] Thus, tuning the microenvironment of the GDE with the optimal amount of electrode wetting without completely flooding the GDE pores is a widely discussed topic.

A variety of strategies are already available in the literature to improve the microenvironment of the GDE. The most promising approaches involve adding

hydrophobic agents and varying the amount of binder in specific GDE layers until the optimal microenvironment is achieved. In a recent publication, not only the amount and type of binder was changed, but with a vacuum-assisted infiltration method, PTFE particles and carbon black were deposited at the interface between carbon fibres and MPL to prevent electrode flooding through the MPL cracks.[71] Another interesting strategy to improve the hydrophobicity was obtained using GDLs directly made from PTFE, circumventing the need to optimise binder strategies within the GDL layers. In a recent publication, FEs > 90% were achieved for the electroreduction of CO_2-to-CO over a time of > 100 h at current densities > 150 $mA \cdot cm^{-2}$ with a PTFE-based GDL.[108] In another publication, a thin metal film (Ag[109] or Cu[110]) was used to contact the PTFE GDL, resulting in stable FEs for >40 h.

Another important topic related to the optimal microenvironment, and especially its maintenance, is the duration of the electroreduction of CO_2. While there are already a few studies investigating the implementation of GDEs for CO_2 electroreduction in the long term (> 100 h), most of the studies, however, restrict their investigations to a short time (< 10 h).[111–114] Reasons for the short observation period are easy to explain; a lot of studies found in the literature focus on the design and enhancement of catalyst materials, where only short-time experiments in small lab-scale reactors, e.g. H-cells, are possible. Furthermore, failure mechanisms that deteriorate the electrode performance additionally influence the electrolysis time to a great extent. Especially for flow cells, mechanisms deteriorating the electrode performance are not always easy to overcome, as no global solution for every occurring problem exists. Thereby, the loss of hydrophobicity and/or binder degradation during operation are the primary mechanisms triggering a decline in electrochemical performance due to electrode flooding.[24,52,60,95,115–117] Other factors contributing to electrode deactivation include carbonate formation,[118–120] catalyst agglomeration, and chemical changes, including catalyst poisoning.[121,122] A schematic

depiction of the most important failure mechanisms possibly occurring during CO_2 electroreduction is shown in **Figure 7**.

The most investigated failure mechanisms in CO_2 electroreduction are the loss of hydrophobicity and the accompanying electrode flooding.[52] This stems from the fact that, especially in flow cells, the reaction environment with the flowing electrolyte can lead to a harsher reaction environment, delamination of the catalyst layer and hence abrasion of the additional hydrophobic particles. Moreover, with the higher applied current densities in flow cells, the electrowetting effect further decreases the hydrophobicity of the GDEs, commencing the risk of loss of hydrophobicity and electrode flooding.[116] The loss of hydrophobicity and the electrode flooding is especially a problem, as, without sufficient hydrophobicity, the separation between CO_2 and liquid becomes insufficient, resulting in reversal of the positive properties of a GDE, i.e. diminished mass transport of CO_2 to the catalyst layer and an optimal reaction zone, moved towards the carbon fibres and MPL, favouring HER. Furthermore, the electrolyte can also initiate binder degradation and even worsen the electrode wetting, halting the electrolyser's function.[52,121] Additionally, the degradation of the binder also influences changes in hydrophobicity. Throughout repeated operations of GDEs utilising Nafion as a binder, a decrease in FE and a reduction in electrode potential, fostering the unwanted HER, were observed.[2] These effects likely stemmed from a progressive loss of hydrophobicity due to structural changes of the side chains and/or sulfonic groups, and stated a rather unsuitability of Nafion as a binder in the investigated setup. Possible strategies to counteract electrode flooding include applying negative pressure differences (pressure on the gas side is higher than on the catholyte side) or establishing a strategy

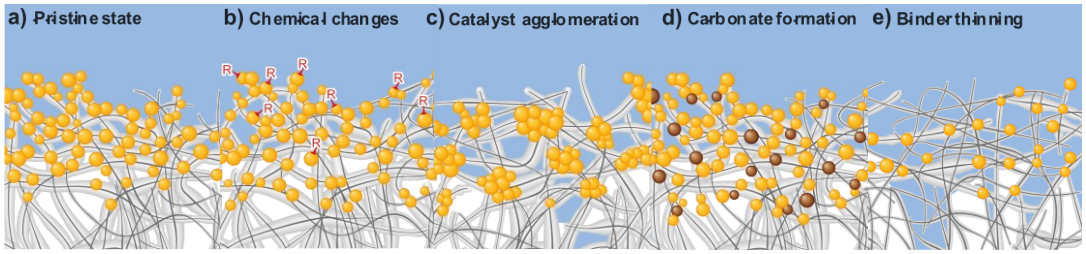


Figure 7. Representation of structural changes on the GDE during operation. (a) Pristine GDE state at t = 0, and final states showcasing deterioration by (b) chemical changes occurring at the catalyst, (c) catalyst agglomeration, (d) carbonate formation – depicted in brown colour, and (e) binder thinning. Reproduced from [1], enabled by the Creative Commons CC-BY license (https://creativecommons.org/licenses/by/4.0/).

for enhancing the hydrophobicity within the GDE, i.e. varying the hydrophobic content within the catalyst layer [75,118,123,124] and GDL [60,70,71] or directly using a PTFE-based GDL.[108–110] Thus, the interplay between the hydrophobic and hydrophilic parts within a GDE, in combination with a proper electrode design, becomes of paramount importance, as the hydrophobic treatment plays a pivotal role in obtaining high FE since the electrode wetting determines the extent of the CO_2 electroreduction at the GDE/electrolyte interface.[23]

Carbonate formation and precipitation are other effects accompanying the electrode flooding, impeding the performance of the GDEs. Thereby, carbonates are formed in the reaction between CO_2 and hydroxide ions in alkaline electrolytes, blocking active sites and the GDL pores. A possible solution for this problem is washing the GDE during the operation. On the other side, changing the electrolyte cation from K^+ to Cs^+ appears to attenuate carbonate precipitation but not fully prevent it, as smaller and well-dispersed deposits were obtained with CsOH as an electrolyte in comparison to KOH.[120,121,125]

Changes to the catalyst itself can include chemical changes or catalyst agglomeration. The chemical changes of the catalyst are triggered mainly by the adsorption of unwanted species from the electrolyte, reaction intermediates, and impurities in the CO_2 to the catalytic active sites. These chemical changes are obstructive, as the impurities will block active catalyst sites, decreasing the ability to perform CO_2 electroreduction. Possible counter strategies include purifying the used electrolytes and the CO_2 feed. On the other hand, in particular, the chemical changes due to reaction intermediates are reversible processes. Renewing the electrolyte or shortly reversing the polarity of the electrolyser could circumvent this problem.[52,121,126–131] The second type of possible catalyst change is agglomeration. With the catalyst agglomeration, the nanoparticulate catalyst particles are combined into bigger particles, which reshapes the catalyst layer and decreases the catalytic active sites. Furthermore, catalyst agglomeration can be accompanied by particle detachment in the form of pulverisation or dissolution, leading to damage to the catalyst layer.[52] Strategies to counteract catalyst agglomeration target a particle confinement strategy to preserve the morphology of the catalyst.[52,132] This can happen, for

instance, by confining the catalyst inside a 3D structure[133] or wrapping the catalyst with rGO as a stabilisation method.[134]

To sum up, deactivating factors in the GDE, such as chemical changes (**Figure 7 b**), catalyst agglomeration (**Figure 7 c**), carbonate formation (**Figure 7 d**), and electrode flooding induced by the loss of hydrophobicity or thinning of the binder (**Figure 7 e**), directly affect the CO_2 electroreduction efficiency. Hence, a meticulous GDE design, with minimal structural changes, particularly over extended operation times, is fundamental to guarantee high and stable formate yields.[121,122,135]

2.5 Cell Design

Another essential aspect in the field of CO_2 electroreduction for discussion includes the design and optimisation of electrolysers. An optimal cell design should enable high current densities and low cell voltages by enhancing mass transport and reducing ohmic resistances.[61 25] As stated in the previous chapter, the GDE design is an essential factor in the electroreduction of CO_2, however, if the GDEs are not tested at industrially relevant conditions (CD > 200 $mA \cdot cm^{-2}$), the electroreduction of CO_2 may never become an economically viable process.[107]

Electrolyser designs for the field of CO_2 electroreduction can generally be divided into two main groups: aqueous-fed and gas-fed CO_2 electrolysers.[107] In the context of aqueous-fed electrolysers, the CO_2 is first solubilised in the electrolyte and diffuses afterwards to the catalyst layer, e.g. H-cells. In the case of gas-fed electrolysers, CO_2 is brought to the catalyst interface in a gaseous state, where GDEs find their application. **Figure 9** shows four often used electrolyser types for the CO_2 electroreduction to formate/formic acid: H-cell as representative of the aqueous fed electrolysers, and for the gas-fed compartment, the zero-gap, anion exchange membrane (AEM)-free and the direct formic acid production (DFAP) electrolyser. The DFAP electrolyser is the only electrolyser enabling direct formic acid production.

A widely used electrolyser design for the investigation of CO_2 electroreduction is the H-cell (**Figure 9 a**), as it is the easiest to use to investigate catalyst properties, for instance, structure, surface tailoring or catalyst composition.[25,107,136] An H-cell consists, in general, of two compartments separated via an ion-exchange membrane to prevent product crossover and reoxidation of the evolved liquid products to CO_2 again. The electrodes are immersed in an aqueous electrolyte; the cathodic compartment contains the working electrode and the reference electrode, while in the anodic compartment, the counter electrode is placed to close the electric circuit as an auxiliary electrode. The cathodic compartment is continuously fed with CO_2 gas to ensure that enough reactant for the reduction reaction is available. The major drawback of the H-cell, however, is the limitation of CO_2 mass transport to the electrode due to the slow diffusion rates of CO_2 in aqueous electrolytes, resulting in low current densities and hindering the investigation at industrially relevant current densities (> 200 $mA \cdot cm^{-2}$).[107,137] Therefore, gas-fed electrolysers, which enable the use of GDE as working electrodes, are a viable approach for the implementation of the CO_2 electroreduction at industrially relevant current densities, as a result of the direct flow of CO_2 to the catalyst layer.[107,137] When discussing electrolysers enabling GDEs as working electrodes, several approaches are available: semi-continuous batch cells and continuous flow-cell electrolysers. Semi-continuous batch cells, for instance, the FlexCell by Gaskatel, are a compromise between the H-cell and the flow cell, enabling the use of GDEs within an H-cell-like reactor. The FlexCell, which is shown in **Figure 8**, has the significant advantage of a simple cell set-up, comprising three parts that are assembled in a building block style and fastened with 4 screws to ensure tightness (e.g. gas and liquid).[138] Furthermore, the FlexCell facilitates a quick investigation of the influence of certain aspects of the GDE design on the electroreduction of CO_2. Even though this semi-continuous batch cell is specially designed for the reproducible study of GDEs and, therefore, particularly suitable, it is rarely reported for the targeted investigation of CO_2 electroreduction.[139]

Continuous flow-cell electrolysers have a significant advantage; in addition to continuous CO_2 fed from the backside of the GDE, they also employ a flowing

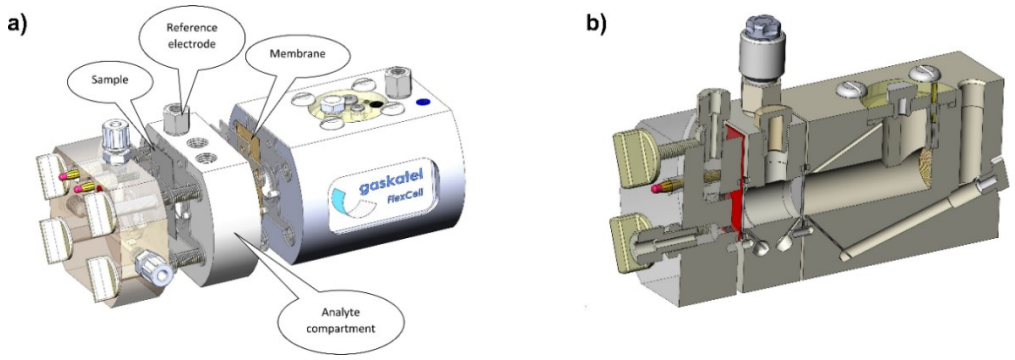


Figure 8: Illustrations of the cell set-up of the semi-continuous batch cell used in this dissertation: FlexCell PTFE, Gaskatel, Germany, a) Exterior view and b) Cross-section.[137]

electrolyte, enabling current densities at industrial-relevant levels. Therefore, the electroreduction of CO_2 should be investigated in continuous flow-cell electrolysers to become an economically viable process. Continuous flow-cell electrolysers reported in the literature and some commercially available, range from zero-gap flow cells (**Figure 9 b**) and AEM-free (**Figure 9 c**) to DFAP cells (**Figure 9 d**). A zero-gap electrolyser (**Figure 9 b**), commonly utilised in the field of water electrolysis[140,141] and PEM fuel cells[142], consists generally of two electrodes separated by an ion exchange membrane. At the cathodic compartment, humidified CO_2 is directly fed to the GDE, while at the anode side, the electrolyte is fed to the electrode. With the zero-gap configuration, mass transport limitations are reduced, which allows for higher CO_2 concentrations in the cathodic compartment and, therefore, an increase in reaction rate and cell efficiency. Further advantages of the zero gap include high FEs, the ability to scale up without FE decreasing and low internal resistance. An important aspect to consider here is the electrolyte and choice of membrane to achieve the desired FE, as the electrolyte significantly affects the pH, which further influences CO_2 electroreduction.[137] As a development of the zero gap cell, the direct acid formic production (DFAP) flow cell can be implemented (**Figure 9 d**).[113] With this cell setup, an additional acidic centre compartment is implemented. It has, therefore, three compartments: anodic, centre and cathodic. The centre compartment is sandwiched between two ion exchange membranes (AEM for the cathode and CEM for the anode), allowing direct formic acid production. To guarantee proton conduction, this compartment is filled with an acidic ion-exchange resin (e.g. Amberlite IR-120H[65,143]). The formate produced at the cathode side migrates

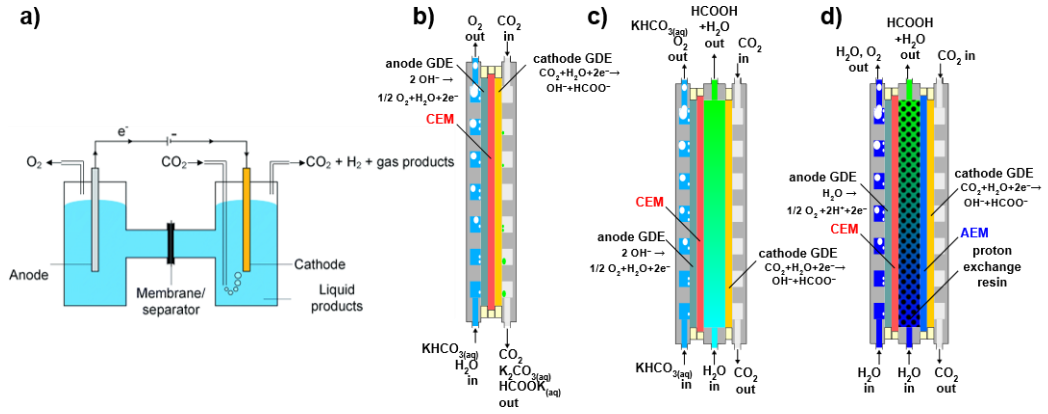


Figure 9. Possible cell setups for the electroreduction of CO_2 to formate/formic acid. a) H-cell, b) zero gap, c) anion exchange membrane (AEM) free flow cell, d) the direct acid formic production (DFAP) flow cell (water-fed). Figure 8 a reproduced from [136] under permission from RSC, Figure 9 b - d reproduced from [1], enabled by the Creative Commons CC-BY license (https://creativecommons.org/licenses/by/4.0/).

through the AEM and reacts there with the protons (coming from the anode) to form formic acid with a high selectivity of up to 90 % FE[143] and concentrations of up to 13 wt%.[143] With this unique setup, electrode flooding is drastically reduced, a higher cell performance can be achieved, and a stable pH near the GDE to suppress HER is established. Further, this design only uses deionized water (avoiding the use of liquid electrolytes) in both the anode and centre compartment, in this latter fluxing formic acid out as a pure product.[137] In the case of the AEM-free electrolysers (**Figure 9 c**), the cell consists of two compartments, similar to the H-cell. Still, instead of a stationary electrolyte, the catholyte and anolyte are continuously cycled to the cathode and anode chambers. An ion exchange membrane separates the compartments to reduce product crossover and -oxidation. With the implementation of GDEs and the additional flowing electrolyte, the mass transport of CO_2 to the catalyst is maximised (ca. 3 magnitude faster than in the H-cell). The flowing electrolyte, furthermore, enhances the transport of the evolving products away from the catalyst layer, enabling high CO_2 electroreduction activity. Moreover, it is also possible to add a reference electrode (RE) to this cell set up near the working electrode to enable potential control.[144–146]

This page is intentionally left blank.

Chapter 3
Experimental

This chapter is based on the publications "*Impact of the Carbon Substrate for Gas Diffusion Electrodes on the Electroreduction of CO_2 to Formate*"[3] by Theußl et al., published in July 2023 in *ChemElectroChem.* And "*Early-Stage Performance Changes of Gas Diffusion Electrodes for Electroreduction of CO_2 to Formate*"[2] by Theußl et al., published in February 2024 in *Sustainable Energy Fuels.*

3.1 Preparation of Gas Diffusion Electrodes

The gas diffusion electrodes (GDEs) were prepared via a manual spray deposition method utilising an airbrush (HG Trigger type 0.3 mm Double Action, Tamiya, Japan).[2,3] Commercial gas diffusion layers were employed as catalyst support and spray deposited with a catalyst ink. The catalyst ink consisted of SnO_2 nanoparticles (<100 nm, Sigma Aldrich, Germany) and a binder dispersion in a ratio of 90:10 wt%. The components were dispersed in isopropyl alcohol (3 ml, 99.5+%, Thermo Scientific, USA) and ultrasonicated for 30 min. The result was a homogeneous GDE with a catalyst loading of 2.0 $mg \cdot cm^{-2} \pm 0.3$ $mg \cdot cm^{-2}$. The active area varied depending on the investigated cell set-up, either 2.81 cm^2 (FlexCell) or 10 cm^2 (ElyFlow). For this thesis, the production of the catalyst ink was carried out similarly in all chapters, and any changes made are indicated in the respective individual chapter descriptions.

The chapter "*Impact of Carbon Substrate for Gas Diffusion Electrodes on the Electroreduction of CO_2 to Formate"*[3] investigated the variation of Gas Diffusion Layers (GDL) from two distinct manufacturers (Toray Industries, Japan and Freudenberg GmbH, Germany). The main differences between the investigated

GDLs were the presence of a microporous layer and the hydrophobic treatment. Regarding the GDLs of Toray Industries, Japan, the objective was additionally to ascertain any differences in the amount of hydrophobic treatment (10 wt.% vs 30 wt.%) and the influence of the thickness (190 µm vs. 370 µm). In the case of the investigated Freudenberg, the GDLs differed in thickness by only about 15%, and the manufacturer did not state the amount of hydrophobic treatment. **Table 2** provides an overview of the investigated GDLs.

Table 2. Overview of the investigated gas diffusion layers (GDLs, TP = Toray Paper Industries, FB = Freudenberg GmbH) either with (w) or without (w/o) microporous layer (MPL) and with (w) or without (w/o) hydrophobic treatment. The hydrophobic treatment for Toray Papers was either 10% or 30% PTFE related to the carbon fibre substrate.

Gas Diffusion Layer (GDL)	**w hydrophobic treatment**	**w/o hydrophobic treatment**
w MPL	TP-060 MPL (30%) (*250 µm)* TP-120-MPL (30%) (*430 µm)* FB-H23C6 (*250 µm*) FB-H23C3 (*290 µm*)	FB-H23C2 (*255 µm*) FB-H24C5 (*270 µm*)
w/o MPL	TP-060 (10%) (*190 µm*) TP- 120 (10%) (*370 µm*) TP-060 (30%) (*190 µm*) TP-120 (30%) (*370 µm*) FB-E20H (*214 µm*)	

The chapter "*Early-Stage Performance Change of Gas Diffusion Electrodes on the Electroreduction of CO_2 to Formate*"[2] investigated the effect of the catalyst loading on the GDE performance and the accompanying early-stage performance changes observed by a loss of GDE activity in terms of maximum current density at –1.15 V_{RHE}. Beginning from this chapter, FB-E20H will be used as GDL. **Table 3** provides an overview of the investigated catalyst loadings and the corresponding weight of the applied catalyst and binder.

Table 3. Investigated catalyst loadings and the corresponding weight of catalyst and binder (in the ratio: 90:10wt%). Reproduced from [2], enabled by the Creative Commons CC-BY license (https://creativecommons.org/licenses/by/4.0/)

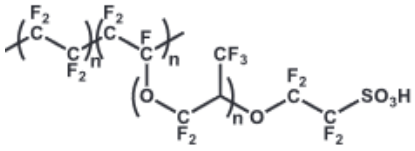
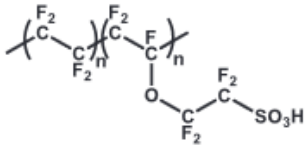
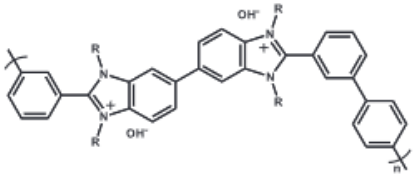
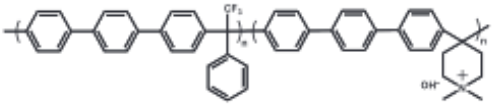
Catalyst loading / [mg·cm^{-2}]	**Absolute Amount / [mg]**	
	SnO_2	**Nafion**
1.1	9.5	1.3
1.3	11.9	1.3
2.3	20.3	1.6
4.2	37.8	4.3
5.8	51.9	5.2
13.0	116.9	9.2

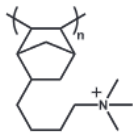
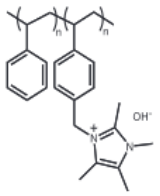
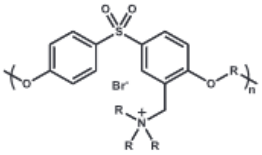
The chapter "*Impact of the Binder Matrix on Gas Diffusion Electrodes for CO_2 Electroreduction to Formate"* investigated the influence of different binder types. The investigated binder ionomers can be classified into cation- and anion exchange ionomers. **Table 4** provides a list of the investigated binders: **Aquivion** (25 wt% in H_2O, DB98-25BS, Sigma Aldrich, USA), **Nafion** (15 wt% in H_2O/EtOH, LQ-1115, IonPower, Germany), **Aemion** (HNN-8, Ionomr, Canada), **Pention** (5 wt%, S35, FuelCell Store, USA), **Piperion** (5 wt% in EtOH, A-5HCO3-EtOH, Versogen, USA), **Fumion** (10 wt% in NMP, FAA-3, FuelCell Store, USA) and **Sustainion** (XA-9, 5 wt% in EtOH, Dioxide Materials, USA), and additionally, also a mixture of **Nafion** and **Aemion** was investigated in the ratio 90:10 wt.%. Due to the different solubility properties of the binder ionomers, different dispersion solvents were implemented. **Table 5** shows the respective chemical formulas of the investigated binders.

Table 4. Overview of the investigated ionomer types as binders for the gas diffusion electrodes.

Binder	Ion Exchange Type		Solvent
	Cation	Anion	
Aquivion	✓		Isopropyl alcohol
Nafion	✓		Isopropyl alcohol
Aemion		✓	Ethanol & Acetone (65:35 wt%)
Pention		✓	Isopropyl alcohol
Piperion		✓	Ethanol
Fumion		✓	Ethanol
Sustainion		✓	Ethanol
Aemion + Nafion	✓	✓	Ethanol & Acetone (65:35 wt%)

Table 5: Types and structural formulas of the investigated binders. Reused from [147] with permission from Elsevier.

Binder	Type of ionomer	Structure
Nafion	Cation exchange	
Aquivion	Cation exchange	
Aemion	Anion exchange	
Piperion	Anion exchange	

Pention	Anion exchange	
Sustainion	Anion exchange	
Fumion	Anion exchange	

In the last chapter, *Influence of the cell setup on gas diffusion electrodes for electroreduction of CO_2 to formate*, the impact of disparate cell setups on GDEs was evaluated. Therefore, commercially available cell designs from Gaskatel GmbH, FlexCell (a gas-fed batch cell), and ElyFlow (a flow cell) were investigated. The required GDEs for this investigation differed in size, depending on the used cell setup: the batch cell GDEs with 2.81 cm^2 active area and the flow cell GDEs with 10 cm^2. To meet the requirements of a flow cell, the catalyst ink of the GDEs was also adapted. A mixture of Nafion and Aemion was used as a binder, and additionally, Vulcan XC72 (0.4 $mg \cdot cm^{-2} \pm 0.03$ $mg \cdot cm^{-2}$, Cabot Corporation, USA) was mixed into the catalyst ink to enhance stability against electrode flooding.

3.2 Characterisation of Gas Diffusion Electrodes

Scanning Electron Microscopy

The GDE topography was investigated with a scanning electron microscope (SEM, Quanta FEG 650 ESEM, FEI, The Netherlands) coupled with an energy-dispersive X-ray detector (EDX, Octane Super-A, Ametek, USA). The SEM was operated at

20 kV, and the images were recorded at 100x, 250x, 400x and 550x magnifications. The EDX detector was used for visualising the catalyst distribution across the GDE surface.

X-Ray Computer Tomography

For the detailed investigation of the GDEs after electrochemical testing, 3D images were acquired by X-ray computed tomography (XCT, Xradia Versa 620, Zeiss, Germany). The samples were taken from the electrolyte-exposed area only and cut into small pieces with a width of 2-3 mm. The XCT was operated at 80 kV, and the images were recorded with a 20x magnification. The tomograms were acquired using 2400 projections over a radiation of 360° with an exposure time of 2 s (TP-120 (30%) and 20 s (TP-120 (30%) MPL) per angle, and a voxel size of 0.633 µm (TP-120 (30%)) and 0.661 µm (TP-120 (30%) MPL). For the further processing of the obtained data and to create the XCT images, the software Dragonfly (Comet Technologies Canada Inc., version 2022.02, Canada) was employed.

The XCT measurements were conducted by C. Heume.

Contact Angle Measurements

The sessile drop contact angles of 1 M $KHCO_3$ in air were measured on an optical contact angle goniometer (OCA100, DataPhysics Instruments, Germany). For each measurement, 2 µl droplets were dispensed onto three different locations to determine an average contact angle. To ensure comparable conditions for the GDEs before and after the electroreduction of CO_2, it was necessary to thoroughly rinse each sample with deionised water and dry it in air to remove residual electrolyte.

Porosimetry

The mean flow pore diameter was determined using the liquid expulsion technique with a capillary flow porometer (Porometer 3GzH, ex Quantachrome - now 3P

Instruments, Germany). For this purpose, a wet and a dry run were performed. Prior to the wet run, circular samples were punched out from the investigated samples and were immersed in a wetting fluid to fill the pores of the sample (Porofil, ex Quantachrome - now 3P Instruments, Germany). For the investigation of the GDEs after the electrochemical testing, the circular samples were taken only from the electrolyte-exposed and uncompressed electrode area.

Electrical Conductivity

Electrical conductivity was determined using a multimeter attached to the conductive tips of a foil thickness gauge (**Figure 10**, Käfer, W&Z-Vertrieb, Germany). The resulting electrical through-plane resistance and the thickness of the samples were determined for a mechanical load of 12 kPa. The electrical through-plane conductivity was then calculated for a contact area of 50 mm^2, based on these two values.

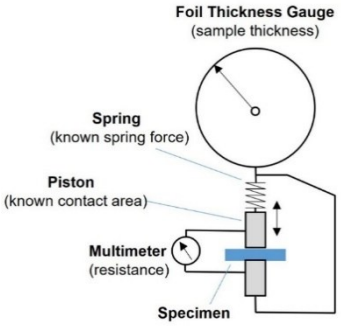


Figure 10. Schematic illustration of the foil thickness gauge used for the determination of the electrical through-plane conductivity. Reproduced from [3], enabled by the Creative Commons CC-BY license (https://creativecommons.org/licenses/by/4.0/).

Raman

The Raman investigations (Senterra, Bruker, Germany) were conducted using a 532 nm laser with a spectral resolution of 9 – 18 cm^{-1}. The middle part of the pristine GDEs and the electrolyte-exposed area of the GDEs after electrochemical characterisation were investigated using a confocal setup with a spatial resolution of 2 µm per pixel (50x magnification) and a laser power of 20 mW. For each GDE, a total of 32 Raman spectra were recorded, and the measurement time per Raman spectrum was 10 seconds.

Thermal Gravimetric Analysis

For determining the thermal stability and exact composition of the investigated GDEs, thermogravimetric analyses were conducted using a thermogravimetric analyser (TGA, STA 449 F1 Jupiter, Netzsch, Germany). Parts of the pristine GDE and parts of the electrolyte exposed area of the GDEs were cut into small pieces, and a sample weight of around 10 mg was deployed to the TGA with a ramp program from room temperature up to 1200°C with a heating rate of 10 K min^{-1} in an oxygen atmosphere.

The TGA measurements were conducted by S. Ziemer.

Vapor Sorption Measurements

To determine the "internal hydrophilicity" of GDEs vapor sorption measurements were carried out using a System Dynamic Vapor Sorption (DVS, Surface Measurement System Ltd., USA). Before the measurements, the samples were degassed for 2 h at 100°C, and an additional turbo vacuum of 10^{-6} mbar was applied. The measurements were conducted at 25°C with a sample size ranging from 10 to 30 mg and varying humidity levels (0–80%).

The vapor sorption measurements were conducted by A. Kretzschmar.

Inductively Coupled Plasma - Mass Spectrometry (ICP-MS)

To determine the amount of catalyst in the electrolyte as a measure for the stability of the catalyst layer during the six-hour CO_2 electroreduction experiments, Inductively Coupled Plasma Mass Spectrometry (ICP-MS, Agilent 7900, Agilent, USA) was used. The electrolyte samples (each 2 ml) were taken at specific time frames during the six-hour CO_2 electroreduction: after

2 min, 16 min, 45 min, 140 min, and 360 min. The electrolyte samples were then analysed with three parallel dilutions of each sample (100-fold).

The ICP-MS measurements were conducted by the Central Institute of Engineering – Electronics and Analytics (ZEA-3) at Forschungszentrum Jülich.

3.3 Electrochemical Characterisation

The electrochemical experiments were performed in two different cell types with the as-prepared GDEs. The measurements related to the electrode architecture (Chapters 4.1-4.3) were conducted in the FlexCell, a gas-fed, three-electrode batch cell from Gaskatel. For the last results chapter, the ElyFlow, a three-electrode flow cell from Gaskatel, was employed.[138,148] Depending on the used cell setup, different potentiostats were used as well; for the flex cell, the multi-channel VSP-300 from BioLogic (France) and in the case of the flow cell measurements, the multi-channel PSG300 from Metrohm (Switzerland). **Figure 11** shows the whole measurement setup.

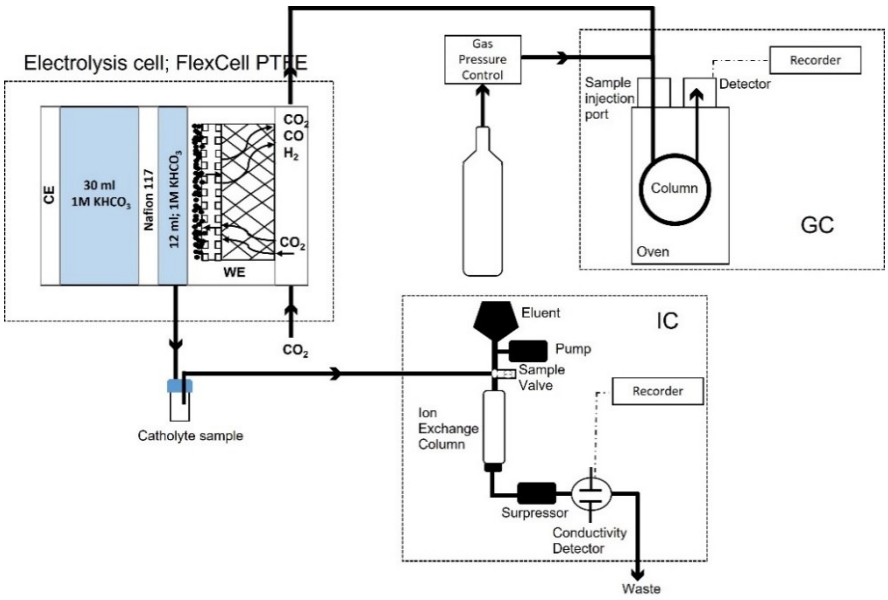


Figure 11. Schematic illustration of the experimental setup: test cell (FlexCell PTFE, Gaskatel, Germany), online GC and offline IC. Reproduced from [3], enabled by the Creative Commons CC-BY license (https://creativecommons.org/licenses/by/4.0/).

In both measurement setups, three electrode assemblies were employed, where the GDEs were the working electrodes (WE), and an Ag/AgCl electrode (RE, RE-1BP, ALS, Japan) was the reference electrode. Depending on the cell setup, the counter electrode (CE) was either a Pt wire (FlexCell) or a mixed metal oxide Ti/IrO_2 metal electrode (ElyFlow) (Gaskatel, Germany). For the ElyFlow setup, additionally, a Ti plate (Ti grade 1 (3.7025)) was added to enhance the electrical contact, shown in **Figure 12 b**. The active electrode areas, i.e., the cathode area exposed to the electrolyte, were 2.81 cm^2 (FlexCell) and 10 cm^2 (ElyFlow). 1 M $KHCO_3$ (≥99.5%, AnalaR NORMAPUR, VWR, Germany) was used for both catholyte and anolyte. The two compartments of the cell were separated by a Nafion 117 membrane (Ion-

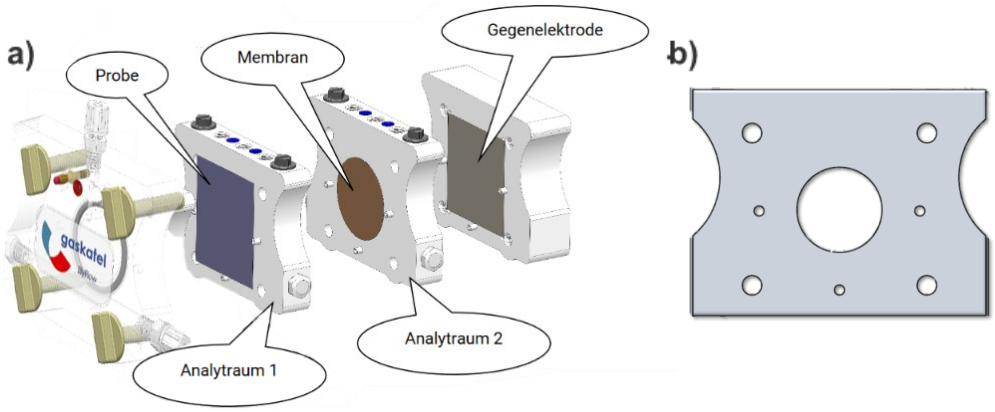


Figure 12. Illustrations of the flow cell set-up (ElyFlow PTFE, Gaskatel, Germany) used in this dissertation. a) Cross section view [148] and b) the additional Ti plate, which is placed between the WE holder and analyte room 1.

Power, Germany). During the electrochemical measurements, a continuous CO_2 flow (99,995%, Air Products GmbH, Germany) of either 20 sccm (FlexCell) or 300 sccm (ElyFlow) was applied to the cell, controlled by a mass flow controller (ELY-FLOW, 10 ml to 500 ml, Bronkhorst, The Netherlands). The flow cell was operated in flow-through mode (20 $ml \cdot min^{-1}$) at the catholyte side and in a re-cycle mode with 30 $ml \cdot min^{-1}$ at the anolyte side, controlled by two peristaltic pumps (Ismatec, Masterflex, Germany). All measurements were conducted at ambient conditions.

The electrochemical analysis was conducted according to a specific procedure, as illustrated in **Figure 13**. Each GDE was investigated at three different current densities (Run 1: –36 $mA \cdot cm^{-2}$, Run 2: –71 $mA \cdot cm^{-2}$ and Run 3: –107 $mA \cdot cm^{-2}$) for 45 min per electrolysis run. Before each run, a "before" measurement sequence was conducted, consisting of three repetitive linear sweep voltammetry (LSV) scans from OCV to –2.0 $V_{Ag/AgCl}$. The LSV scans were repeated three times to ensure experimental stability. Only the last scan is utilised for comparison of the different GDEs. Furthermore, between each

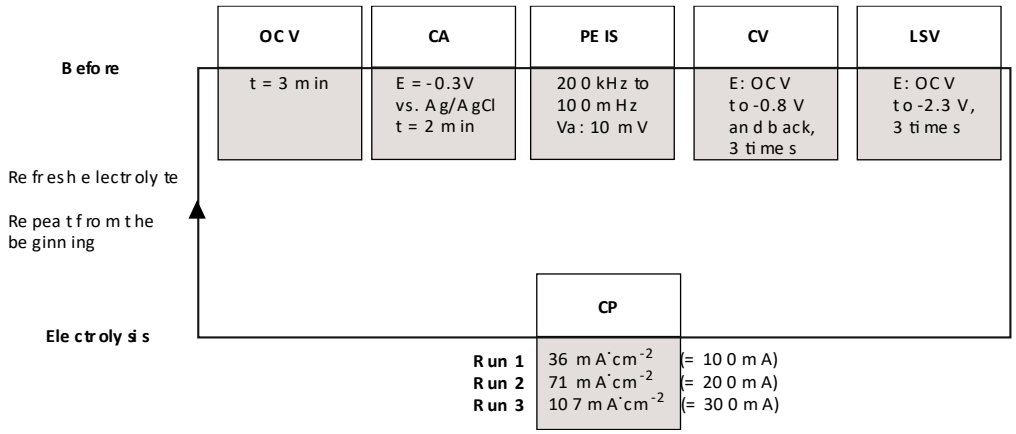


Figure 13. Procedure for the electrochemical characterisation of the investigated gas diffusion electrodes (GDEs). "Before" each electrolysis run, induced by a chronopotentiometric program step (CP), each GDE is subjected to the full set of analysis techniques, i.e., OCV, CA, PEIS, (3x CV) and 3x LSV, shown in the top line of the schematic. Reproduced from [2], enabled by the Creative Commons CC-BY license (https://creativecommons.org/licenses/by/4.0/).

electrolysis run (Run 1 - 3), the electrolyte was manually exchanged and refreshed, thereby ensuring comparable starting conditions for each subsequent run. The electrochemical analysis in the flow cell was conducted similarly, except for the duration of the electrolysis, 30 min instead of 45 min. Further measurements with higher current densities (160 $mA \cdot cm^{-2}$ - 540 $mA \cdot cm^{-2}$) and a longer-term 6 h electrolysis experiment at 160 $mA \cdot cm^{-2}$ were also conducted.

All potentials shown in this thesis are reported with reference to the reversible hydrogen electrode (RHE). Therefore, the recalculation of the obtained electrode potentials is conducted according to equation 1, under the

assumption of a constant pH of the CO_2-saturated electrolyte, 1 M $KHCO_3$, of $pH = 7.6$.[149]

$$E(RHE) = E(Ag/AgCl) + 0.059\,V * pH + 0.210\,V \qquad \text{(Eq. 1)}$$

Moreover, all potentials are iR Drop corrected. In the batch cell, the resistance of the measurement setup (0.7 Ω) was determined by a reference experiment using a silver plate as the working electrode at various electrode potentials. In the flow cell, the iR Drop correction is implemented via the PEIS measurement conducted during the "before" measurement sequence. For both measurements, the iR-Drop correction was calculated using equation 2 below:

$$E(RHE) = E(Ag/AgCl) + 0.059\,V * pH + 0.210\,V - i * R \qquad \text{(Eq. 2)}$$

3.4 Product Analysis

The evolving products were quantified via online gas chromatography (GC, Trace 1310, Thermo Fisher Scientific, USA) and offline ion exclusion chromatography (IC, S150, Sykam, Germany). The GC system was equipped with two channels, utilising a Haysep Q and a Molecular Sieve 5 Å packed column, and a thermal conductivity detector. For the determination of H_2 and CO, Ar (6N, Linde, Germany) and He (6N, AirProducts, Germany) were used as carrier gases, respectively. Sample acquisition took place every nine minutes, for the gas products automatically via a transfer line and for the determination of the formate concentration manually by collecting a 0.5 ml sample of catholyte (without refilling with fresh electrolyte).

For the quantification, both methods were calibrated using external standards. For the gas products H_2 and CO, the calibration measurements were conducted using certified calibration gases (Linde, Germany) in a 3-point

calibration with fixed amounts of H_2 (1000 ppm, 16700 ppm, 99700 ppm) and CO (979 ppm, 19900 ppm, 99900 ppm). Prior to the electrochemical measurements, the gas flow rate out of the cell was determined. This was achieved by utilising a gas counter, either the MGC–1 V3.4 PPMA (Milli-Gascounter, Ritter, Germany) for the gas-fed batch cell or a drum gas counter (TG0.5−PP-PP, Ritter, Germany) for the flow cell. The flow was determined three times, and the average was used to calculate the Faradaic Efficiency (FE).

The FE for gaseous products i (= H_2, CO) was calculated as a momentary value FE, using the following equation (3):

$$FE_i = \frac{z_i \cdot F \cdot \frac{p}{R \cdot T} \cdot V_{out} \cdot c_i}{I} \cdot 100\% \qquad \text{(Eq. 3)}$$

Here, z denotes the number of electrons transferred (=2), F the Faraday's constant, p the outlet pressure (1.013 bar), R the universal gas constant, T the temperature, V_{out} the flow rate of the eluent gas, c_i the determined product gas concentration, and I the total applied current.

The ion exchange chromatography (IC) system was equipped with a SykroGel-Ex 450 SA-E01 column, utilising an aqueous eluent solution comprised of 7% acetonitrile (≥99.3%, HiPerSolv CHROMANORM®, VWR, USA) and 0.7 mmol perflourobutyric acid (99%, Thermo Scientific, USA). Before each analysis run, a calibration series for formate was recorded in the range from $3.3 \cdot 10^{-4}$ mol·l^{-1} to $2.2 \cdot 10^{-2}$ mol l^{-1}.

Comparing the concentration of formate in the static catholyte of the cell at certain time intervals during the measurement, the Faradaic efficiency (FE) for the electroreduction of CO_2 to formate was calculated as an interval value FE, using the following equations (4) – (6):

$$\Delta FE = \frac{Q_{theo.(x+1)} - Q_{theo.(x)}}{Q_{tot.(x+1)} - Q_{tot.(x)}} \quad \text{(Eq. 4)}$$

$$Q_{theo.} = n \cdot z \cdot F \cdot 0.277 \quad \text{(Eq. 5)}$$

$$Q_{tot.} = \Sigma (I \cdot t) \quad \text{(Eq. 6)}$$

Q_{theo} denotes the theoretical charge, determined based on the produced amount of formate n during a certain time interval x (e.g. t min to $t + y$ min). Q_{tot} denotes the total charge consumed during the respective interval.

3.5 Reproducibility of the Measurements

Concerning GDE reproducibility, the preparation, electrochemical and physico-chemical analysis of each GDE were repeated three times. The standard deviation was estimated conservatively based on the scattering of the individual results for these three measurements. The estimated standard deviations are as follows and were added as error bars to the corresponding results.

Impact of Carbon Substrate for Gas Diffusion Electrodes on the Electroreduction of CO_2 to Formate

- LSV current density: ±15% on the reported value
- FE - Formate: ±10% on the reported value
- FE - H_2: ±33% on the reported value
- FE - CO: ±50% on the reported value
- Avr. electrode potential: ±0.05 V_{RHE} on the reported value
- Avr. flow pore diameter: ±10% on the reported value
- Area specific internal resistance: ±10% on the reported value

Early-Stage Performance Change of Gas Diffusion Electrodes for Electroreduction of CO_2 to Formate

- LSV current density: ±20% on the reported value
- FE - Formate: ±10% on the reported value
- Avr. electrode potential: ±0.05 V_{RHE} on the reported value

Impact of the Binder Matrix on Gas Diffusion Electrodes for Electroreduction of CO_2 to Formate

- LSV current density: ±20% on the reported value
- FE - Formate: ±15% on the reported value
- FE - H_2: ±36% on the reported value
- FE - CO: ±38% on the reported value
- Avr. electrode potential: ±0.06 V_{RHE} on the reported value

Influence of the Cell Setup on Gas Diffusion Electrodes for Electroreduction of CO_2 to Formate

- LSV current density: ±10% on the reported value
- FE - Formate: ±11% on the reported value
- FE - H_2: ±30% on the reported value
- FE - CO: ±25% on the reported value

Avr. electrode potential: ±0.07 V_{RHE} on the reported value

This page is intentionally left blank.

Chapter 4

Results and Discussion

4.1 Impact of Carbon Substrate for Gas Diffusion Electrodes on the Electroreduction of CO_2 to Formate

The results shown in this chapter, "*Impact of the Carbon Substrate for GDEs on the Electroreduction of CO_2 to Formate*"[3] are partially published in ChemElectroChem from Wiley (DOI: https://doi.org/10.1002/celc.202300121). The published parts include the Toray Carbon Paper GDLs investigation and are published under a CC-BY 4.0 license. The XCT measurements were conducted by C. Heume, and S. B. C. Lehmann contributed the graphical design of **Figure 22**.

A valuable approach for implementing CO_2 electroreduction is using carbon paper-based gas diffusion electrodes (GDEs) as cathodes.[150–152] The performance of the GDEs highly depends on their architecture and material properties, including the choice of the GDL. Concerning the GDL, key factors such as (i) the presence of a MPL, (ii) the thickness, and (iii) the hydrophobic treatment of both the carbon fibre substrate and the MPL can influence electrode performance. As a result, many studies have been published on designing and investigating GDEs for Power-to-X applications in general, and for CO_2 electroreduction to formate in particular.[153–157] However, limited research has focused on the impact of the GDL on GDE performance for CO_2-to-formate, despite the unique demands of GDEs in this context. This chapter, therefore, offers a comprehensive investigation of how the choice of GDL affects the performance of spray-coated GDEs during the electroreduction of CO_2 to formate. The focus is on GDLs from Toray Paper and Freudenberg, due to their vast coverage in literature, broad variety and wide global availability. **Table 2**

provides an overview of the investigated GDLs., which mainly vary in their hydrophobic treatment, GDL thickness and presence of a microporous layer (MPL).

4.1.1 Physico-chemical characterisation of the investigated carbon substrates

Figure 14 and **Figure 15** present SEM images from two manufacturers, Toray and Freudenberg, in different states: pristine GDLs and GDEs before and after CO_2 electroreduction. The pristine GDLs (**Figure 14 a, d, g**, **j, m, p,** and **15 a, d, g, j, m**) display the typical appearance of carbon fibres and MPL before catalyst deposition. **Figure 14 j** and **Figure 15 d**, reveal that small cracks already appear in the pristine GDLs with MPL (TP-060 MPL (30%) and FB-H23C2).[158,159] Conversely, GDEs without MPL display a structure of overlapping carbon fibre layers interspersed with open spaces (see **Figure 14 a, d, g, m** and **Figure 15 a)**.

The effect of the catalyst coating can be described as a thick decoration of the carbon fibres, particularly for GDEs without MPL (shown in **Figure 14 b), e), h), n)** and **Figure 15 b)**). For the GDLs with MPL, a catalyst film forms on top of the MPL (**Figure 14 k, q** and **Figure 15 e, h, k, n**). Generally, the catalyst coating process (spray deposition) results in a homogeneous distribution of catalyst across the GDE surface, as illustrated in the EDX in **Figure 16**. However, at the catalyst loading of 2.0 ± 0.3 mg·cm^{-2}, neither the open spaces between the carbon fibres nor the cracks in the MPL are bridged by the catalyst layer. During the electrochemical measurements, the catalyst layer remains mostly intact with only minor topographical changes, suggesting that most of the catalyst stays on the GDE. The EDX images in **Figure 16** support this observation**.**

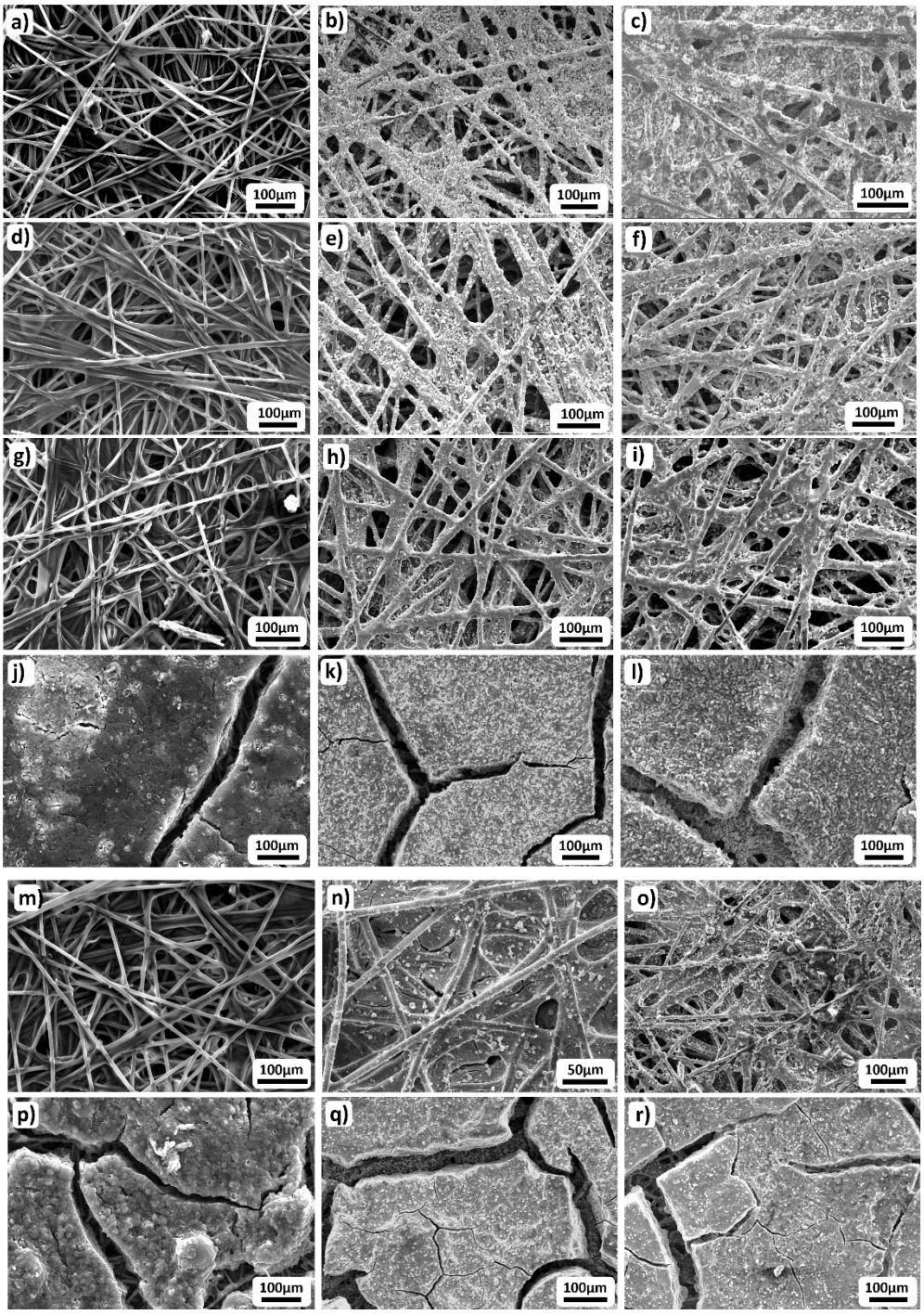


Figure 14. SEM images of the Toray-based pristine gas diffusion layers (GDLs) and the gas diffusion electrodes (GDEs) before and after use. Images for: a-c) TP-060 (10%), d-f) TP-120 (10%), g-i) TP-060 (30%), j-l) TP-060 (30%) MPL, m)-o) TP-120 (30%) and p)-r) TP-120 (30%) MPL. a), d), g), j), p) Pristine GDLs (without catalyst). b), e), h), k), n), q) GDEs before electrochemical testing. c), f), i), l), o), r) GDEs after electrochemical testing. Reproduced from [3], enabled by the Creative Commons CC-BY license (https://creativecommons.org/licenses/by/4.0/).

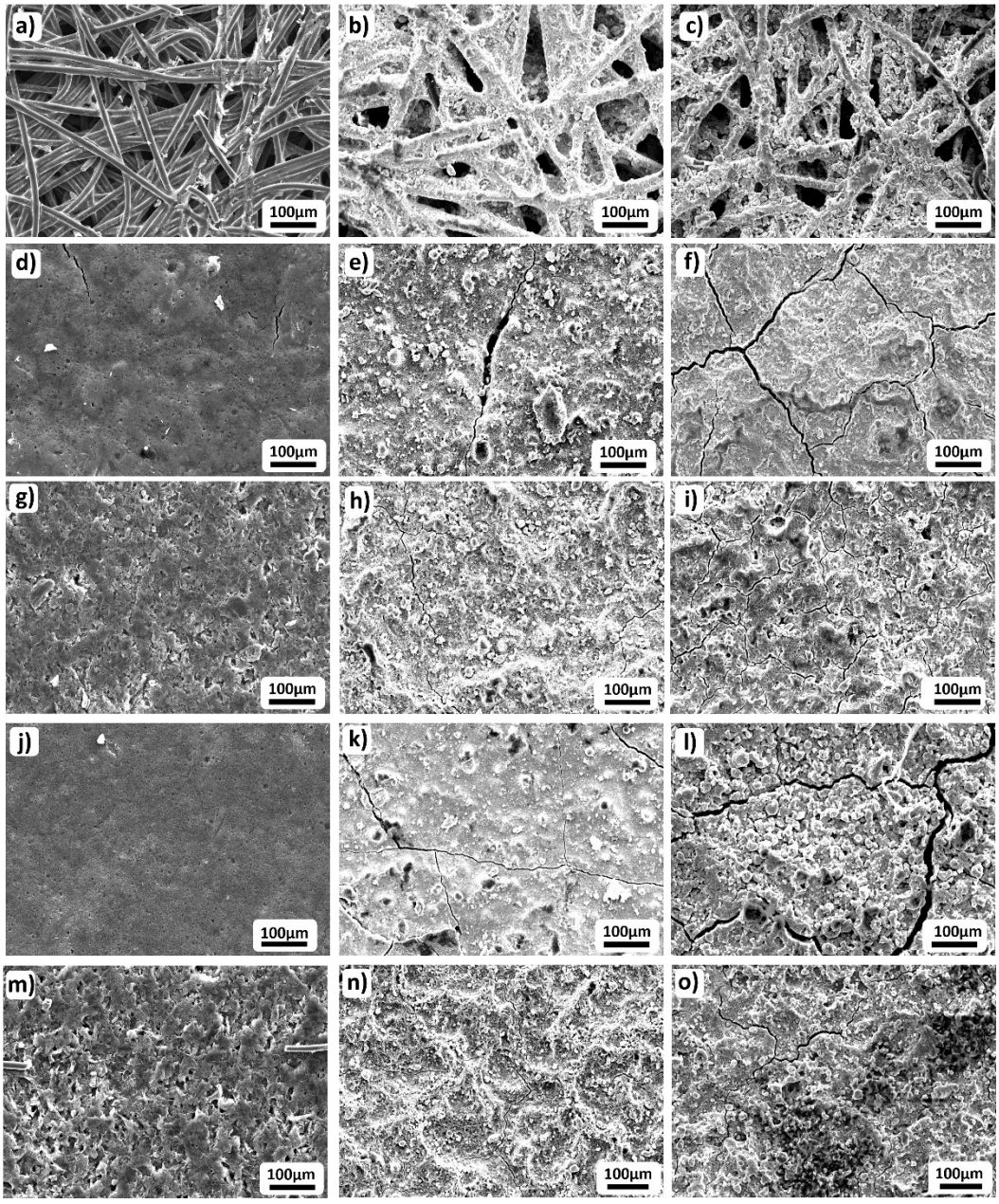


Figure 15.SEM images of the Freudenberg-based pristine gas diffusion layers (GDLs) and the gas diffusion electrodes (GDEs) before and after use. Images for: a-c) FB-E20H, d-f) FB-H23C2, g-i) FB-H23C3, j-l) FB-H23C6, g)-i) FB-H24C5. a), d), g), j), m) Pristine GDLs (without catalyst). b), e), h), k), n) GDEs before electrochemical testing. c), f), i), l), o) GDEs after electrochemical testing.

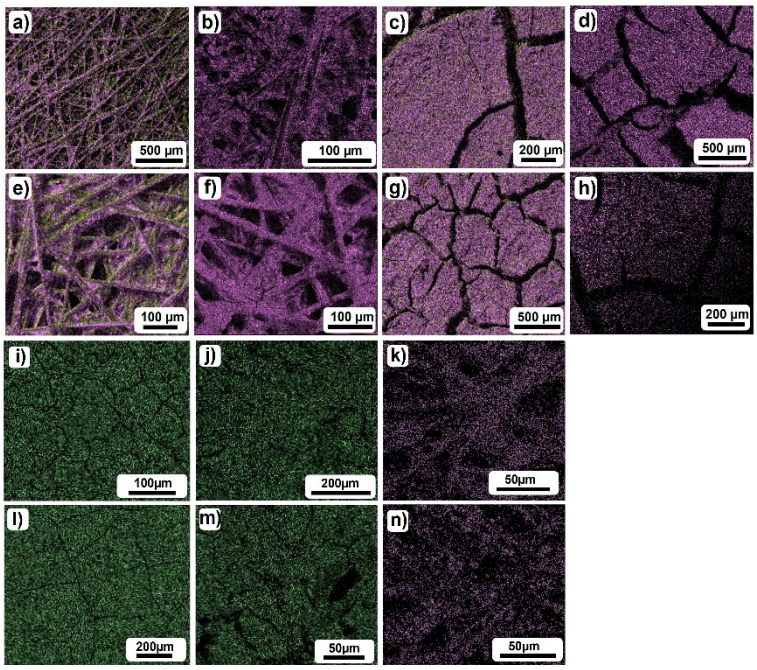


Figure 16. EDX maps for Toray Carbon Paper and Freudenberg a-b) TP-060 (30%), c-d) TP-060 MPL (30%), e-f) TP-120 (30%), g-h) TP-120 MPL (30%), i-l) FB-H23C2, j-m) FB-H23C6, k-n) FB-E20H, before (left) and after CO_2 electroreduction (right). Green/Purple colour identifies Sn. Partly reproduced from [3], enabled by the Creative Commons CC-BY license (https://creativecommons.org/licenses/by/4.0/).

Figure 17, along with the videos accessible via the QR code, presents 3D images of the GDEs TP-120 (30%) and TP-120 MPL (30%) after CO_2 electroreduction. Using high-resolution X-ray computed tomography (XCT), the location and distribution of the catalyst are visible through elemental contrast between C in grey and Sn in yellow. When comparing the two GDEs, differences in how deeply the catalyst penetrates can be determined. For TP-120 (30%), the catalyst layer appears spread out, while for TP-120 MPL (30%), the catalyst layer is concentrated on the GDE surface, with some particles beneath the cracks in the MPL. A previous study on SIGRACET GDLs for CO_2 electrolysis to CO showed a similar pattern, where a MPL helped form a more focused catalyst layer.[70]

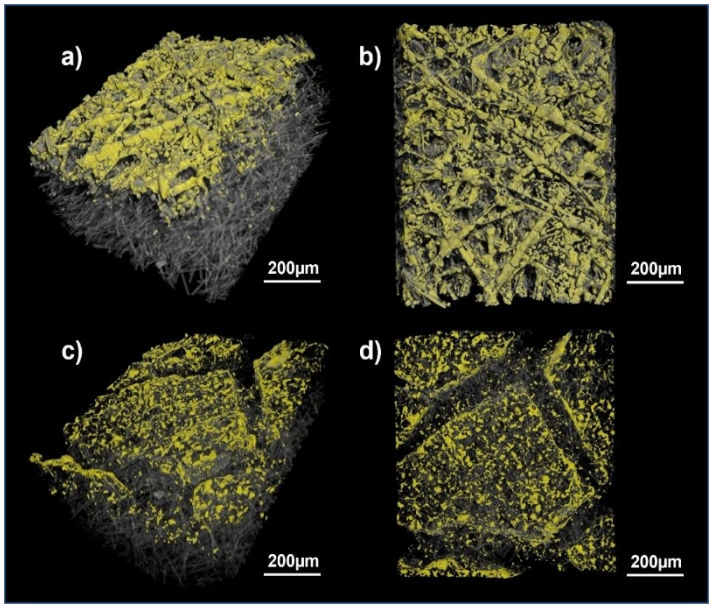


Figure 17. Exemplary XCT images of the investigated gas diffusion electrodes (GDEs) after CO_2 electroreduction. The yellow colour indicates regions with a high Sn mass density, i.e., SnO_2 as a part of the catalyst layer vs. the carbon-based substrate. a-b) Side and top view for TP-120 (30%), c-d) Side and top view for TP-120 MPL (30%). (More details in the Videos via the QR code). Reproduced from [3], enabled by the Creative Commons CC-BY license (https://creativecommons.org/licenses/by/4.0/).

For further investigation of the carbon substrate's influence, measurements of contact angle (CA), porosity, and through-plane conductivity were also performed (see **Table 6** to **Table 8**). The contact angles of the pristine GDLs, TP-060 (10%) and TP-120 (10%), are approximately 142°. In contrast, TP-060 (30%), TP-120 (30%), TP-060 MPL (30%) and TP-120 MPL (30%) show higher contact angles ranging from 143° to 147°. These results indicate a clear relationship between hydrophobicity and the presence of an MPL. The highest contact angles for the Toray Papers, around 147°, are observed with GDLs that have the highest hydrophobic treatment: TP-060 MPL (30%) and TP-120 MPL (30%). Regarding the Freudenberg GDEs, the lowest contact angle, 138 ± 5°, is obtained for the GDL without MPL, FB-E20H. GDLs with MPL show contact angles ranging from 140° to 149°. Notably, the highest contact angles are seen for FB-H23C2 and FB-H23C3, with 149 ± 4° and 147 ± 2°, respectively.

Furthermore, the deposition of the catalyst layer appears to impair the hydrophobicity of the investigated samples. The contact angles for all GDEs decrease after the catalyst layer deposition compared to the pristine GDL. For Toray Papers, the most considerable decrease in contact angle is around 10% from 147 ± 4° to 133 ± 2° (TP-120 MPL (30%)). In contrast, the FB-H23C2 shows the highest decrease, with about 20% from 149 ± 4° to 117 ± 5°. This suggests a strong influence of the binder Nafion in the catalyst layer on the hydrophobicity of the GDEs before the electrochemical measurements. In a reference experiment, the GDLs were only coated with Nafion, which mainly decreased the contact angle of the GDLs without MPL (**Table 6**). For the GDLs with MPL, however, the contact angle remains unchanged. Therefore, the catalyst layer likely obscures he hydrophobicity of the GDL in the absence of a MPL, most likely due to the differing surface topographies.

Although the surface topography remains relatively stable after the electrochemical measurements, as shown in **Figure 14** and **Figure 15**, the hydrophobicity of the GDEs seems affected. The lowest detectable contact angle is 36 ± 12° for FB-H24C5, likely due to the absence of hydrophobic treatment on the carbon fibres. CO_2 electroreduction significantly impacted TP-060 (30%) MPL and TP-120 (30%) MPL, causing the applied test liquid to be immediately absorbed. Conversely, FB-E20H showed the highest contact angle with 84 ± 10°. A possible explanation for the significant decrease in hydrophobicity would be a (partial) displacement or deterioration of the binder during electrochemical testing.[118] Similar effects have been reported for Nafion used as a binder in fuel cell electrodes.[160] Additionally, the cracks in the MPL for TP-060 MPL and TP-120 MPL (30%) (**Figure 14**) might explain the immediate absorption of the test liquid, as they could facilitate electrolyte drainage. Nevertheless, given the remaining hydrophobicity of the supporting carbon fibres and the MPL, the test liquid does not flood any of the electrodes.

Table 6: Comparison of the contact angles (1M $KHCO_3$) for pristine GDLs, GDLs with Nafion coating only and GDEs before and after CO_2 electroreduction. Contact angle measurements were performed using 1 M $KHCO_3$ electrolyte at room temperature. (Scattering of measurement results represents the standard deviation for the contact angle.) Partly reproduced from [3], enabled by the Creative Commons CC-BY license (https://creativecommons.org/licenses/by/4.0/).

Gas Diffusion Electrode [GDE]	Contact Angle			
	GDL (pristine) [°]	GDL (Nafion coating) [°]	GDE (before) [°]	GDE (after) [°]
TP-060 (10%)	141 ± 6	135 ± 2	140 ± 4	41 ± 12
TP-120 (10%)	142 ± 8	134 ± 2	138 ± 7	42 ± 20
TP-060 (30%)	143 ± 4	131 ± 2	141 ± 11	44 ± 14
TP-120 (30%)	145 ± 4	135 ± 2	139 ± 3	42 ± 11
TP-060 MPL (30%)	147 ± 2	145 ± 0.4	134 ± 4	absorbed
TP-120 MPL (30%)	147 ± 4	145 ± 1	133 ± 2	absorbed
FB-E20H	138 ±5	134 ± 1	126 ±5	84 ±10
FB-H23C2	149 ±4	148 ± 2	117 ±5	43 ±10
FB-H24C5	140 ±6	136 ± 3	124 ± 6	36 ±12
FB-H23C6	140 ±6	146 ± 1	110 ±0.4	63 ±13
FB-H23C3	147 ±2	143 ± 1	117 ± 5	53 ± 9

Regarding the GDL porosity (see **Table 7**), three out of five samples without MPL show a slight decrease in the mean flow pore diameter after catalyst deposition, followed by an increase after electrochemical tests. For example, TP-120 (10%) has a mean flow pore diameter of 25 ± 3 µm in the pristine state, which slightly decreases to 24 ± 2 µm after catalyst deposition and then increases to 30 ± 3 µm after electrochemical testing. A slight decrease in mean pore diameter is expected after catalyst deposition, as adding an extra layer can slightly decrease GDL porosity. However, SEM images in **Figure 14** and **Figure 15** show no clogged pores, as the catalyst coating results in a discontinuous layer. The increase in mean flow pore diameter suggests the removal of parts of the catalyst layer due to the CO_2 electroreduction reaction. This, however, is contradicted by the SEM images in **Figure 14** and **Figure 15**, and the EDX maps in **Figure 16**, which show that the catalyst layer remains intact after CO_2 electroreduction. Therefore, the measurements of mean flow pore diameter do not strongly indicate a change in electrode structure. The other tested GDEs without MPL show no difference in the absolute mean flow pore diameters due to either catalyst deposition or CO_2 electroreduction.

Comparing GDEs with and without MPL shows a distinct difference between the two manufacturers. For Toray Paper GDLs, the mean flow pore diameters of both types are quite similar, even though one type has an MPL with much smaller pores. For example, TP-120 (30%) and TP-060 MPL (30%) have mean flow pore diameters as high as 23 ± 2 µm. On the other hand, Freudenberg GDLs display a notable difference in porosity due to the presence of a MPL. FB-E20H, for example, has a mean flow pore diameter of 21 ± 2 µm, while the other four range from 0.1 to 0.8 µm. This absence of a difference in results of GDLs with and without MPL in Toray Paper GDLs can be explained by large cracks in the MPL, shown in **Figure 14**, that bypass the pores of the MPL. As a result, the GDE porosity was not significantly affected by catalyst deposition or electrode testing. However, cracks in the MPL of TP-060 MPL and TP-120 MPL (30%) allow bypassing of the MPL's narrow pores. Over a longer period, porosity changes may become relevant, as observed in proton exchange membrane fuel cells (PEMFCs).[161]

Table 7. Results for the porosity measurements of the pristine GDLs and the GDEs before and after the CO_2 electroreduction. (Scattering of measurement results represents the estimated standard deviation for the mean flow pore diameter measurement (±10%).) Partly reproduced from [3], enabled by the Creative Commons CC-BY license (https://creativecommons.org/licenses/by/4.0/)

Gas Diffusion Electrode [GDE]	Mean Flow Pore Diameter		
	GDL (pristine) [µm]	GDE (before) [µm]	GDE (after) [µm]
TP-060 (10%)	29 ± 3	27 ± 3	28 ± 3
TP-120 (10%)	25 ± 3	24 ± 2	30 ± 3
TP-060 (30%)	26 ± 3	25 ± 3	31 ± 3
TP-120 (30%)	23 ± 2	23 ± 2	22 ± 2
TP-060 MPL (30%)	23 ± 2	23 ± 2	24 ± 2
TP-120 MPL (30%)	22 ± 2	25 ± 3	24 ± 2
FB-E20H	21 ± 2	20 ± 2	20 ± 2
FB-H23C3	0.8 ±0.08	0.7 ±0.07	0.7 ±0.07
FB-H23C2	0.5 ±0.05	0.5 ±0.05	0.6 ±0.06
FB-H24C5	0.4 ±0.04	0.8 ±0.08	0.5± 0.05
FB-H23C6	0.1 ±0.01	0.6 ±0.06	0.5± 0.05

Opposed to the porosity results in **Table 7**, the through-plane conductivity of the investigated GDEs in **Table 8** varies significantly depending on the electrodes' conditions. This condition depends on their preparation, usage, and can also be non-uniform, as significant experimental scattering was found for conductivity measurements through the plane, particularly for GDEs before the electrochemical measurements. In this regard, the electrical conductivity of the pristine GDLs from Toray Carbon Paper remains very consistent across all samples, aligning with their hydrophobicity and porosity, ranging from 5 – 18 $mS \cdot cm^{-1}$. However, the pristine GDLs from Freudenberg showed substantially higher through-plane conductivity compared to Toray Carbon Paper GDLs. FB-E20H shows nearly a 10-fold higher through-plane conductivity over the GDL with the lowest through-plane conductivity (TP - 060 (30%)), 46 ± 5 $mS \cdot cm^{-1}$ vs 5 ± 1 $mS \cdot cm^{-1}$.

The through-plane electrical conductivity of the GDEs before electrochemical measurements is markedly lower than the conductivity of the corresponding GDLs. A possible explanation for this observation relates to the deposition of an electrically insulating binder and oxidic catalyst particles onto the GDE as part of the catalyst layer, i.e. Nafion and SnO_2. However, the strong scattering indicates a certain inhomogeneity in the distribution of the binder and/or catalyst on the GDE. **Table 8** shows a decrease of the through-plane conductivity due to the catalyst deposition of at least two orders of magnitude, ranging from 0.0006 ± 0.00002 $\mu S \cdot cm^{-1}$ to 2 ± 0.06 $mS \cdot cm^{-1}$. The insulating character of the catalyst layer, however, is not maintained during the electrochemical measurements. The increase in through-plane conductivity after the electrochemical measurements may be related to several mechanisms: the reduction of SnO_2 to metallic Sn,[28] and the partial displacement or deterioration of the binder, which aligns with the contact angle observations. For example, TP-120 (10%) shows a conductivity of 10 ± 2 $mS \cdot cm^{-1}$ before the catalyst deposition, 0.02 ± 0.02 $\mu S \cdot cm^{-1}$ after the catalyst deposition and 3 ± 1 $mS \cdot cm^{-1}$ again after the electrochemical testing. The same observation is also made for the Freudenberg GDEs. FB-E20H shows a conductivity of 46 ± 5 $mS \cdot cm^{-1}$ before the catalyst deposition, 2 ± 0.6 $mS \cdot cm^{-1}$ after the catalyst deposition and 24 ± 3 $mS \cdot cm^{-1}$ after the electrochemical testing. Hence, the electrodes

undergo significant changes during the electrochemical experiments, meaning that their through-plane conductivity cannot be considered constant throughout the experiments.

Table 8: Results for the through-plane conductivity measurements of the pristine GDLs and the GDEs before and after the CO_2 electroreduction. (Scattering of measurement results represents the standard deviation for through-plane conductivity measurements). Reproduced from [3], enabled by the Creative Commons CC-BY license (https://creativecommons.org/licenses/by/4.0/).

Gas Diffusion Electrode [GDE]	Through-Plane Conductivity		
	GDL (pristine) [mS/cm]	GDE (before) [mS/cm]	GDE (after) [mS/cm]
TP-060 (10%)	6 ± 3	0.001 ± 0.3	0.5 ± 0.2
TP-120 (10%)	10 ± 2	0.02 ± 0.02	3 ± 1
TP-060 (30%)	5 ± 1	0.0006 ± 0.00002	5 ± 2
TP-120 (30%)	18 ± 13	0.04 ± 0.06	13 ± 0.9
TP-060 MPL (30%)	7 ± 0.6	0.06 ± 0.01	0.4 ± 0.2
TP-120 MPL (30%)	11 ± 1	0.2 ± 0.2	2 ± 0.4
FB-E20H	46 ± 5	2 ± 0.6	24 ± 3
FB-H23C3	20 ± 3	0.9 ±0.1	1.4 ± 0.7
FB-H23C2	41 ± 5	1.4 ± 0.2	0.7 ± 0.3
FB-H24C5	26 ± 2	0.7 ± 0.8	2 ± 1
FB-H23C6	32 ± 5	1 ± 0.3	0.8 ± 0.8

4.1.2 Electrochemical characterisation of the investigated carbon substrates

For electrochemical characterisation, the investigated GDEs underwent three consecutive runs at constant cathodic current densities (Run 1: −36, Run 2: −71, and Run 3: −107 mA cm^{-2}) in fresh 1 M $KHCO_3$ for 45 min each. During each run, formate accumulated in the static electrolyte of the cathodic chamber, causing negative feedback on CO_2 conversion efficiency to formate due to the pH sensitivity of the reaction.[162,163] This is why, for evaluating the obtained FEs for formate, a fixed time interval is used for each electrolysis experiment, 2–11 min after the electrolysis begins. This approach ensures comparable conditions across the investigated GDEs, enabling a quick assessment of how individual GDL properties influence GDE performance. Before and after each electrolysis run, PEIS and LSV scans were performed to assess the cathode-related part of the internal resistance of the cell setup and to monitor the evolution of the GDE performance in terms of cathodic current density. **Table 9** lists resistances derived from PEIS scans at OCV, which corresponds to the first intersection of the impedance spectrum with the x-axis of the individual Nyquist plots (**Figure 18 a**).

The area-specific resistance listed in **Table 9** decreases with repeated use of each GDE, starting from its highest resistance before Run 1 and ending with the individual's lowest resistance before Run 3. This change can be attributed to factors such as electrode conductivity[164] and/or electrode wetting[165] to the determined resistances, in addition to a constant iR-drop across the electrolyte. To elucidate additional contributions to the internal resistance, a reference experiment using a silver sheet as the working electrode was carried out. This experiment demonstrated a consistent and reproducible resistance of 0.7 **Ω** for 1 M $KHCO_3$ (**Figure 18 b**), aligning with the literature.[166] This confirms the assumption of additional contributions to internal resistance beyond the iR-drop. However, a clear attribution is not directly possible, as the hydrophobicity and electrical conductivity changed simultaneously for all GDEs in this study (see **Table 8**).

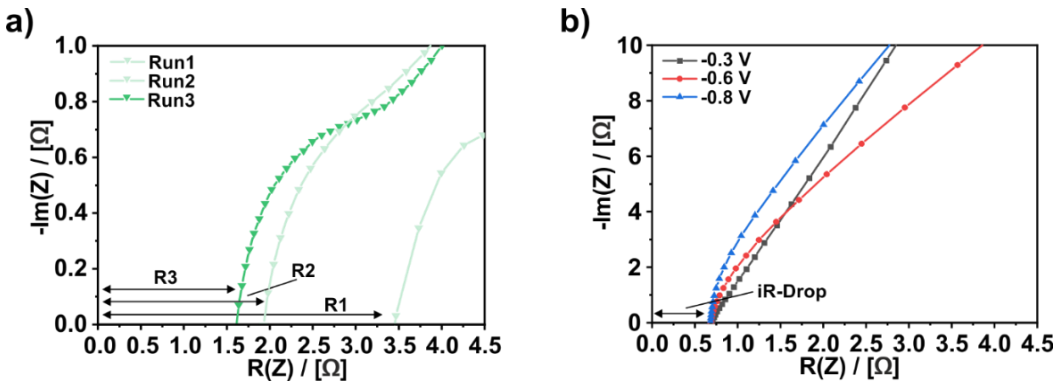


Figure 18. Exemplary Nyquist plots derived from PEIS measurements in the FlexCell. a) TP-120 (10%) prior to the CO_2 electroreduction. R1 – R3 denote the internal resistance of the whole setup as reported in **Table 9**, resulting from the conductivity of the electrolyte and the GDE-related contributions. b) Reference experiment on a silver plate at various electrode potentials. Reproduced from [3], enabled by the Creative Commons CC-BY license (https://creativecommons.org/licenses/by/4.0/).

Generally, an increased interface area and an improved electron transport in the electrode should lower the internal resistance for a non-ideal electrode. Looking into some results in detail, **Table 9** shows that the area-specific resistances for the GDEs based on TP-060 MPL and TP-120 MPL (30%) slightly decrease, from 0.51± 0.05 and 0.50± 0.05 Ω/cm^2 prior to Run 1 to 0.49± 0.05 and 0.49± 0.05 Ω/cm^2 prior to Run 3. The Freudenberg GDLs, however, yield different results from the Toray GDLs. The individual resistances are all in the same range, independent of the part of the conducted experiments. This becomes especially evident when comparing the area-specific resistance of the GDEs based on FB-E20H and FB-H24C5. They show area-specific resistances from 0.62 ± 0.05 Ω·cm^{-2} prior to Run 1 to 0.59 ± 0.05 Ω·cm^{-2} prior to Run 3 and 0.62 ± 0.05 Ω·cm^{-2} prior to Run 1 and 0.6 ± 0.05 Ω·cm^{-2} prior to Run 3, respectively. Based on this, it may be assumed that the electrical through-plane conductivity has a more significant effect on the determined resistances than the electrode wetting, as the resistances for the GDEs based on TP-060 MPL and TP-120 MPL (30%) reported in **Table 8** start on a low level, with the through-plane conductivities being relatively high. The other GDEs, on the other hand, show high resistances for relatively low through-plane conductivities, for otherwise drastically decreasing hydrophobicities for both types of GDEs. In

Table 9. Results of the internal resistance measurement by PEIS as conducted prior to every electrolysis run (Figure S4) in fresh 1 M $KHCO_3$ at room temperature. (Standard deviation based on estimates (± 10%)). Partly reproduced from [3], enabled by the Creative Commons CC-BY license (https://creativecommons.org/licenses/by/4.0/)

Gas Diffusion Electrode (GDE)	Area specific resistance R		
	Run 1	Run 2	Run 3
	[Ω/cm²]	[Ω/cm²]	[Ω/cm²]
Dioxide Materials	0.42 ± 0.04	0.38 ± 0.04	0.38 ± 0.04
TP-060 (10%)	1.37 ± 0.1	0.61 ± 0.06	0.52 ± 0.05
TP-120 (10%)	1.32 ± 0.1	0.70 ± 0.07	0.56 ± 0.06
TP-060 (30%)	0.89 ± 0.09	0.61 ± 0.06	0.60 ± 0.06
TP-120 (30%)	0.69 ± 0.07	0.60 ± 0.06	0.53 ± 0.05
TP-060 MPL (30%)	0.50 ± 0.05	0.49 ± 0.05	0.49 ± 0.05
TP-120 MPL (30%)	0.51 ± 0.05	0.50 ± 0.05	0.49 ± 0.05
FB- E20H	0.62 ±0.06	0.62 ± 0.06	0.74 ± 0.07
FB- H23C2	0.62 ±0.06	0.59± 0.06	0.59 ± 0.06
FB- H24C5	0.62 ±0.06	0.59± 0.06	0.6 ± 0.06
FB- H23C6	0.61 ±0.06	0.58 ± 0.06	0.58 ± 0.06
FB- H23C3	0.61 ±0.06	0.7 ± 0.07	0.68 ± 0.07

any case, the PEIS measurements confirm a significant change in the GDE properties, consistent with the results of the electrochemical experiments. This was already expected based on the results in **Table 9**.

Table 9 also lists internal resistances from a commercial SnO_2-GDE by Dioxide Materials for comparison. This GDE shows the lowest resistances with values ranging from 0.42 ± 0.04 Ω/cm^2 before Run 1 to 0.38 ± 0.04 Ω/cm^2 before Run 3, which may be due to an alternative GDE structure of the reference GDE. The catalyst was directly mixed with carbon to form a mixed carbon/catalyst layer.[143]

Figure 19 illustrates the change in cathodic current density at −1.15 V_{RHE} for the third of three LSV scans performed before each CO_2 electroreduction run (complete LSV data shown in **Figure A 1**). Similar to the resistances from PEIS scans, the cathodic current density decreases with repeated use across most investigated GDEs. For example, the TP-060 MPL (30%) GDE shows a cathodic current density of 212.9 ± 32 mA·cm^{-2} before Run 1, it decreases to 178.7 ± 27 mA·cm^{-2} before Run 2 and to 148.1 ± 22 mA·cm^{-2} before Run 3. Similarly, the Freudenberg GDLs also exhibit this trend; FB-E20H shows a cathodic current density of 164 ± 25 mA·cm^{-2} before Run 1 and 130.7 ± 20 mA·cm^{-2} before Run 2 and 132.9 ± 20 mA·cm^{-2} before Run 3. However, although GDE performance typically deteriorates over time due to gradual component degradation,[118] a decline in cathodic current density from electrochemical testing is not always observed for all GDEs. The reference GDE from Dioxide Materials remains the most stable, with a current density of 135.1 ± 20 mA·cm^{-2} before Run 1, 141.9 ± 21 mA·cm^{-2} before Run 2 and 119.7 ± 18 mA·cm^{-2} before Run 3. This stability aligns with the consistent cell voltage of a direct formic acid electrolyser at moderate current densities of 140 ± 21 mA·cm^{-2} reported by Dioxide Materials, over several hundred hours.[113]

Furthermore, the decrease in cathodic current density at −1.15 V_{RHE} for the custom-made GDEs mainly occurs between Run 1 and Run 2, with stable performance observed before Run 2 and Run 3 (**Figure 19**). For instance, the TP-120 MPL (30%) GDE shows a 31% decrease in cathodic current density from 203.2 ± 30 mA·cm^{-2} before Run 1 to 139.8 ± 21 mA·cm^{-2} before Run 2. However, for the comparison between Run 2 and Run 3, an identical performance was obtained (140 ± 21 mA·cm^{-2}, each). The same happens with Freudenberg GDLs. The cathodic current density of FB-H23C2 shows a 31% decrease in current density when comparing before Run 1 and Run 2, while before Run 2 and Run 3 present the same

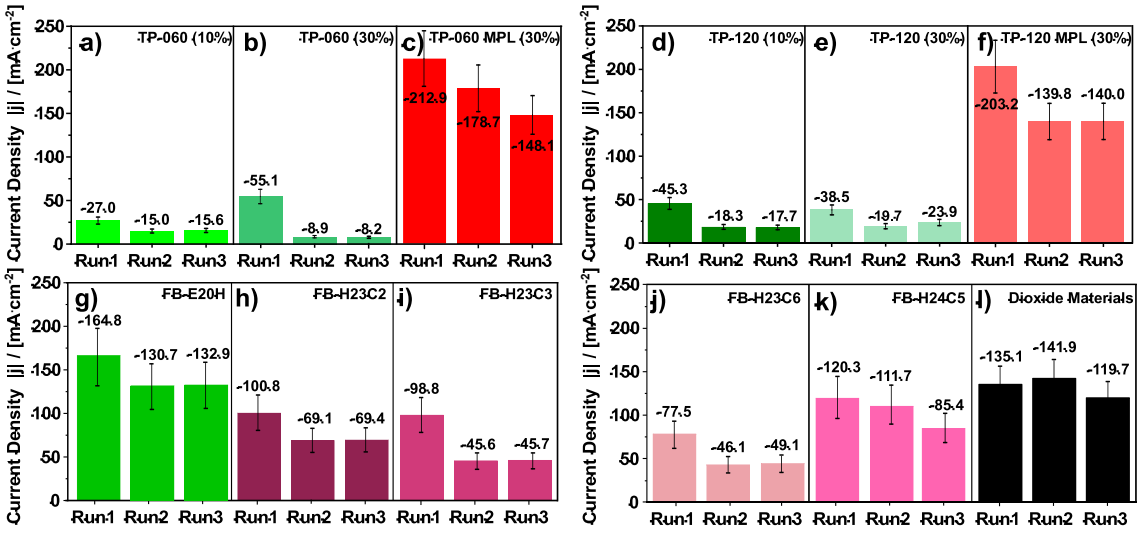


Figure 19. Evaluation of the current density at −1.15 V_{RHE} (iR-drop corrected) for the third of three LSV-scans prior to each electrolysis runs (Run 1-3). Results for the gas diffusion electrodes (GDEs) without microporous layer (MPL) are shown in green. Results for the GDEs with MPL are shown in red. The results for the reference electrode by Dioxide Materials is shown in black. (Additional details about the LSV-scans can be found in Figures S12. Error bars indicate the estimated standard deviation). Partially reproduced from [3], enabled by the Creative Commons CC-BY license (https://creativecommons.org/licenses/by/4.0/).

result. Hence, the decrease of the cathodic current densities is mostly an initial effect occurring between Run 1 and Run 2

When relating the results of the LSV scans to the PEIS measurements summarised in **Table 9**, it appears that a low initial internal resistance before Run 1 allows for a high cathodic current density in the following LSV scan. This is indicated by the results for the TP-060 and 120 MPL (30%) GDEs, which show low initial resistances of 0.50 ± 0.05 Ω·cm^{-2} and 0.51 ± 0.05 Ω·cm^{-2} as well as high cathodic current densities before Run 1. In contrast, the other four Toray Paper GDEs show higher resistances and, vice versa, lower cathodic current densities. The Freudenberg GDLs, on the other hand, exhibit different behaviour. The area-specific resistances of the investigated Freudenberg GDLs are all in the same range of about 0.6 ± 0.06 Ω·cm^{-2}, but the obtained cathodic current density before Run 1 still varies significantly. While the FB-E20H obtains a cathodic current density of 164.8 ± 25 mA·cm^{-2} before Run 1, the FB-H23C6 only obtains about half of it before Run 1. This might be related to the fact that FB-H23C6 and FB-H23C3 have an additional hydrophobic treatment at the carbon fibres, which impedes the electrical

conductivity of the otherwise very conductive carbon fibres. This effect is only minimised by the fact that FB-E20H has the highest through-plane conductivity of all investigated GDLs in this chapter. However, due to the simultaneous decrease in electrode resistance and cathodic current density for the Toray Paper GDLs, the proposed link between PEIS measurements and LSV results does not apply to Run 2 and Run 3. Otherwise, the cathodic current densities of the GDEs should even increase as resistance decreases, which is not observed. Therefore, the changes in resistance listed in **Table 9** cannot account for the loss of catalytic activity seen in the LSV scans. Regarding the Freudenberg GDLs, no correlation can be established between PEIS measurements and LSV results, nor with through-plane conductivity. This suggests the potential presence of additional opposing mechanisms that affect the GDE properties.

Concluding the present characterisation, **Figure 20** displays the results of individual electrolysis runs for the investigated GDEs (see **Figure A 2** for the individual potential vs. time curves). **Figure 20 a** shows the avr. electrode potential during 45 min of continuous CO_2 electroreduction at constant cathodic current densities from −36 $mA \cdot cm^{-2}$ to −107 $mA \cdot cm^{-2}$. Generally, the electrode potentials become more negative with increasing cathodic current density, reflecting higher electrode polarisation, but are also influenced by GDE deterioration observed in LSV measurements. For instance, the TP-060 (10%) GDE shows an avr. electrode potential of $-1.42 \pm 0.05\ V_{RHE}$ at $-36\ mA \cdot cm^2$ and $-1.59 \pm 0.05\ V_{RHE}$ at $-107\ mA \cdot cm^2$. Furthermore, the avr. electrode potential results can be divided into two groups at $-107\ mA \cdot cm^2$. Group 1 with avr. electrode potentials are always more negative than $-1.5 \pm 0.05\ V_{RHE}$, and group 2 with avr. electrode potentials are more positive than $-1.5 \pm 0.05\ V_{RHE}$. In group 1, neither major nor consistent differences became apparent. For example, the TP-120 (10%) GDE shows the most positive avr. electrode potential with $-1.31 \pm 0.05\ V_{RHE}$ and $-1.47 \pm 0.05\ V_{RHE}$ for −36 and −71 $mA \cdot cm^{-2}$, but at −107 $mA \cdot cm^{-2}$ it shows the most negative electrode potential with $-1.77 \pm 0.05\ V_{RHE}$. In group 2, the avr. electrode potentials at −36 $mA \cdot cm^{-2}$ are all in the same range, around $-0.85 \pm 0.05\ V_{RHE}$. However, at −71 $mA \cdot cm^{-2}$ and −107 $mA \cdot cm^{-2}$, a broad range of avr. electrode potentials of about $\pm 0.5\ V_{RHE}$ are

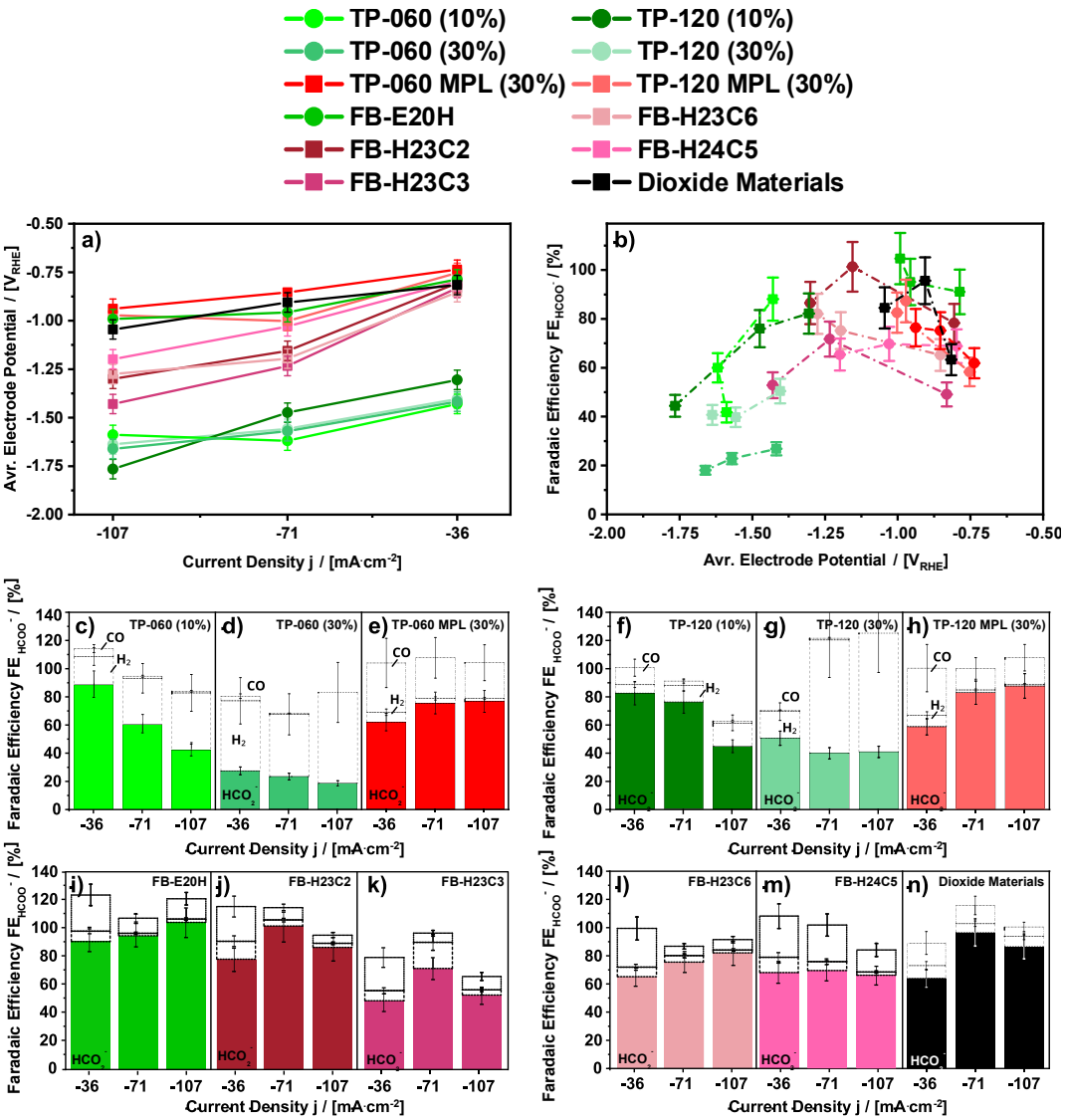


Figure 20. Evaluation of the avr. electrode potential and the resulting FE for CO_2 electroreduction to formate, H_2 and CO at different current densities ranging from –36 to –107 mA·cm^{-2}. Results for the gas diffusion electrodes (GDEs) without microporous layer (MPL) are shown in green. Results for the GDEs with MPL are shown in red. Results for the reference electrode by Dioxide Materials are shown in black. a) Avr. electrode potential during 45 min of continuous CO_2 electroreduction. b) Avr. electrode potentials vs. corresponding FE for formate (Interval: 2 – 11 min). c-i) Faradaic efficiencies for formate, H_2 and CO at different current densities ranging from –36 to –107 mA·cm^{-2} (Interval: 2 – 11 min). Error bars indicate the estimated standard deviation of a typical experiment. Partly reproduced from [3], enabled by the Creative Commons CC-BY license (https://creativecommons.org/licenses/by/4.0/).

apparent. This becomes especially evident when comparing the two GDLs with the most positive and most negative electrode potential, TP-060 (30%) MPL and FB-H23C3. They show an avr. electrode potential of –0.85 ±0.05 V_{RHE} and –1.23 ± 0.05 V_{RHE} at –71 $mA \cdot cm^{-2}$ and –0.9 ± 0.053 V_{RHE} and –1.42 ± 0.05 V_{RHE} at –107 $mA \cdot cm^{-2}$, respectively. The exceptional result here, however, is the obtained electrode potential of the FB-E20H. As a GDL without MPL, it would be assumed to obtain a similar avr. electrode potentials as the Toray Paper GDLs without MPL. However, due to the highest through-plane conductivity of all investigated GDLs, shown in **Table 7**, the avr. electrode potentials are below –1 V_{RHE} for all three applied current densities.

Figure 20 c-n illustrate the FEs corresponding to the data in **Figure 20 a**. In general, the FEs for formate are very diverse, ranging from 18 ± 1.8% to 100 ± 10%. The remaining charge is consumed by HER or CO_2 electroreduction to CO during the process. The FEs for formate results can be categorised into two groups, corresponding to the results in **Figure 20 a**. One where the FE for formate mainly decreases with increasing applied current density, and another where the FE for formate mainly increases. In group 1, the TP-060 (10%) GDE shows the highest FE for formate at −36 $mA \cdot cm^{-2}$, with 88 ± 8.8% decreased to 42 ± 4.2% at −107 $mA \cdot cm^{-2}$. In Group 2, overall, the FB-E20H GDE shows the highest FEs for formate, with 96 ± 9.6% at −71 $mA \cdot cm^{-2}$ and 100 ± 10% at −107 $mA \cdot cm^{-2}$. Combining the results from **Figure 20 a** and **Figure 20 c-i**, **Figure 20 b** provides a representation of the FEs for formate versus the avr. electrode potential during the electrolysis. Here, the investigated GDEs show the best CO_2 conversion at around −1.2 ± 0.2 V_{RHE}, with a tendency to increase FEs for formate from −0.8 to −1.2 V_{RHE} and decrease FEs for formate for electrode potentials more negative than −1.25 V_{RHE}. Accordingly, TP-060 and 120 (10%) show a decreasing FE, while TP-060 and TP-120 MPL (30 %), as well as FB-E20H and FB-H23C6, show an increasing FE for an increasing cathodic current density. The other investigated Freudenberg GDLs showed a mixed behaviour of the two investigated groups. First, an increase of FE is obtained until the optimal avr. electrode potential is reached, followed by a decrease in FE. Thus, the efficiency of CO_2 electroreduction to

formate for the investigated GDEs is highly electrode potential-dependent, whereby the electrode potential must neither be too positive nor too negative to allow efficient conversion. This observation corresponds well with previous reports, where medium electrode potentials of −1.2 V_{RHE},[167] −1.14 V_{RHE} [168] and −1.10 V_{RHE} [90] have been identified as the most efficient potentials for CO_2-to-formate on Sn-based catalysts.

4.1.3 Discussion

Effect of the GDL Thickness

The results presented in this chapter show no specific differences in GDE performance that would justify a preferred choice for one of the investigated GDL thicknesses (<300 µm and >400 µm), although thinner GDLs are expected to have lower electrical resistances. FE values in **Figure 20** show no pattern regarding the thickness of the GDEs. For example, the TP-060 (10%) GDE shows slightly higher FEs for formate than the TP-120 (10%) GDE at −36 $mA \cdot cm^{-2}$ with FEs for formate of 88 ± 8.8% and 82 ± 8.2%, respectively. In the case of the Toray Paper GDLs with the higher hydrophobic treatment, the TP-120 (30%) GDE outperforms the TP-060 (30%) GDE with FEs for formate 50 ± 5% vs 27 ± 2.7% at −36 $mA \cdot cm^{-2}$. Furthermore, the LSV results of the Toray Paper GDLs are largely identical regarding the observed cathodic current densities. For example, the TP-060 (10%) GDE shows current densities of 15.0 ± 2 and 15.8 ± 2 $mA \cdot cm^{-2}$ in Run 2 and Run 3, which are comparable to the TP-120 (10%) GDE with 18.3 ± 3 and 17.7 ± 3 $mA \cdot cm^{-2}$. The similarity of the GDE performance as a function of the GDL can be explained by the mostly identical GDE properties determined by microscopy images, contact angle, porosity, through-plane conductivity, and PEIS measurements. In fact, the imaging techniques showed no influence of the GDL thickness on the GDE surface morphology, which is expected since the bulk material is not involved in the GDE preparation. Similarly, the contact angle and the porosity measurements did not reveal any discernible difference due to the exclusive surface sensitivity of the contact

angle measurements and the homogeneity of the GDL fibre structure (see QR code in **Figure 17**).

Furthermore, the PEIS measurements did not display any advantage for thin over thick GDEs, either, although higher resistances for thicker GDEs are expected due to longer conductive pathways in thicker GDLs.[169,170] On the contrary, the TP-060 (30%) GDE shows an even higher resistance of 0.60 ± 0.06 $\Omega \cdot cm^{-2}$ before Run 3 than the TP-120 (30%) GDE with 0.53 ± 0.05 $\Omega \cdot cm^{-2}$ (**Table 9**). The latter is in accordance with the through-plane conductivity, which is higher for the TP-120 (30%) GDE than for the TP-060 (30%) GDE, 13 ± 0.9 $mS \cdot cm^{-2}$ vs. 5 ± 2 $mS \cdot cm^{-2}$. However, as is apparent for the other GDE couple without MPL, the through-plane conductivity cannot be treated as a single descriptor to predict the internal resistance as observed by PEIS. Although the TP-060 (10%) GD shows a lower through-plane conductivity than the TP-120 (10%) GDE, 0.5 ± 0.2 vs. 3 ± 1 $mS \cdot cm^{-2}$, the observed resistance in the PEIS-scan before Run 3 is lower too, 0.52 ±0.05 vs. 0.56 ± 0.06 $\Omega \cdot cm^{-2}$. Thus, a supporting effect of the Toray Paper thickness for the CO_2 electroreduction towards formate is not observed. Regarding the Freudenberg GDEs, a relationship between the thickness and the reported properties and parameters could not be established as well. The investigated GDLs are all in the same thickness range of 214 – 290 µm, directly in the middle of TP-060 (190 µm) and TP-120 (430 µm). The best result of all investigated GDLs, regarding obtained cathodic current densities prior to Run 1 to prior to Run 3, avr. electrode potentials and FE for formate is obtained with FB-E20H (214 µm), whose thickness is in the middle of all investigated GDLs. However, FB-E20H is the GDL with the highest through-plane conductivity, which could be the reason for the obtained results. Thus, no clear influence of thickness can be determined for the Freudenberg GDLs either. With this, the presented results are in very good agreement with a previous study on the effect of the GDL thickness on the electrode performance in a proton exchange membrane fuel cell (PEMFC), where no direct correlation was found between the thickness and the electrode performance.[171] Similarly, in a recent study for the electroreduction of CO_2 to CO, the GDL thickness did not affect the GDE performance during short-term measurements. Only during long-term

measurements (>100 h) did GDEs based on thicker GDLs have an advantage over thinner ones.[61] A possible reason for this was given in a study for the electroreduction of CO_2 to formate, where thicker GDLs, driven by custom-made MPLs with increasing thickness, showed better performance than thinner ones due to extended prevention of pore flooding.[172] On the contrary, a negative influence of the GDL thickness has also been reported due to decreased CO_2 transport rates.[173] However, the transport limit certainly requires a comparatively high current density to become effective, which is not the case for the present study.

Effect of the Hydrophobic Treatment

Unlike the GDL thickness, the presence and content of the substrate's hydrophobic treatment strongly influence the electrochemical performance, as the electrode wetting determines the extent of the CO_2 electroreduction at the GDE/electrolyte interface.[23] Comparing the results of the TP-060 and 120 (10%) GDEs and the TP-060 and 120 (30%) GDs, a lower hydrophobic treatment of the GDL appears to be beneficial for the obtained FEs for formate. For example, the TP-060 (10%) GDE shows FEs for formate from 88 ± 8.8% at −36 $mA \cdot cm^{-2}$ to 42 ± 4.2% at −107 $mA \cdot cm^{-2}$, while the TP-060 (30%) GDE obtains FEs for formate from 27 ± 2.7% at −36 $mA \cdot cm^{-2}$ to 18 ± 1.8% at −107 $mA \cdot cm^{-2}$ (**Figure 20**). Regarding the Freudenberg GDLs with an MPL, a hydrophobic treatment seems beneficial. For example, the FB-H23C6 GDE (with hydrophobic treatment) shows an increasing FE with increasing applied current densities from 65 ± 6.5% at −36 $mA \cdot cm^{-2}$ to 82 ± 8.2% at −107 $mA \cdot cm^{-2}$. While in the case of the FB-H24C5 GDE (without hydrophobic treatment), the FE for formate is in the same range for all three applied current densities, around 68 ± 6.8%. The current trend of improved GDE performance in terms of selectivity through lower hydrophobic treatment is not supported by the LSV scans in **Figure 19**. Concerning the Toray Paper GDEs, the LSV scans show similar results for all GDEs without MPL. Explaining the observed benefit of GDEs with the lower hydrophobic treatment (10% PTFE) for Toray Paper is challenging, as the contact angles, porosity, and electrical conductivity of the pristine GDEs without MPL were very similar, regardless of the

hydrophobic treatment (**Table 6** - **Table 8**). For instance, TP-060 (10%) GDE showed a contact angle of 140 ± 4° before and 41 ± 12° after the electrolysis, while TP-060 (30%) GDE showed 141 ± 11° before and 44 ± 14° after the electrolysis. This suggests a similar interface between the catalyst, the electrolyte and the gas phase for both hydrophobic treatments, mainly influenced by the catalyst layer composition. Additionally, the unexpectedly lower electrical through-plane conductivities of the Toray Paper (10% PTFE) GDEs after electrochemical testing [174] do not negatively affect electrode performance. The main difference related to the hydrophobic treatment was the initial internal resistance measured by PEIS. The internal resistance was significantly higher for GDEs with 10% PTFE (1.37 ± 0.1 and 1.32 ± 0.1 $\Omega \cdot cm^{-2}$, **Table 9**) compared to those with 30% PTFE (0.89 ± 0.09 and 0.69 ± 0.07 $\Omega \cdot cm^{-2}$). Moreover, the Toray Paper GDEs with lower hydrophobic treatment showed a more significant decrease in internal resistance during electrochemical characterisation, indicating that their properties, in combination with electrochemical testing, changed more substantially than those with the higher hydrophobic treatment.

In contrast to the results of the Toray Paper GDEs, for the Freudenberg GDEs, the LSV scans show that the GDEs without hydrophobic treatment obtain up to 3-fold higher cathodic current densities at −1.15 V_{RHE} than the GDEs with one. For example, the FB-H24C5, as GDE without hydrophobic treatment, shows cathodic current densities from 120.3 ± 18 $mA \cdot cm^{-2}$ before Run 1 to 85.4 ± 13 $mA \cdot cm^{-2}$ before Run 3. While the GDE with hydrophobic treatment, FB-H23C6, obtains cathodic current densities of 77.5 ± 12 $mA \cdot cm^{-2}$ before Run 1 to 49.1 ± 7 $mA \cdot cm^{-2}$ before Run 3. A possible explanation for the contradictory influence of the hydrophobic treatment regarding the obtained cathodic current densities and FEs for formate can be understood by looking at the results of the contact angle measurements and the through-plane conductivity (**Table 6**). The results obtained with the contact angle measurements are quite similar for the investigated Freudenberg GDLs with MPL and state a rather hydrophilic surface. On the other hand, the results obtained for the through-plane conductivity are quite interesting. While in the case of the Toray Paper GDLs, the through-plane conductivity increases again

after the electrochemical measurements, the Freudenberg GDLs with hydrophobic treatment show a further decrease in through-plane conductivity after the electrochemical measurements. This might indicate some deterioration of the catalyst layer, resulting in lower cathodic current densities in the LSV runs. Despite the increased through-plane conductivity after electrochemical measurements for the Freudenberg GDLs without hydrophobic treatment, the FEs for formate decrease with increasing current density, and this can be explained by exceeding the optimal avr. electrode potential (**Figure 20**) for high FEs for formate.

When comparing the present results with the literature, similarities and differences are evident. As an example of the agreeing part, a study on the impact of carbon fibre substrate on electrochemical reduction of CO_2 to CO found that low hydrophobic treatment with 10% PTFE provided the best performance in terms of partial current density.[67] In terms of disagreement, a study on the effects of hydrophobic treatment on electrode performance in a proton exchange membrane fuel cell (PEMFC) observed superior performance for GDEs based on GDLs with the highest PTFE content.[171] Additionally, a recent study on the electroreduction of CO_2 to CO reported no significant influence of GDL hydrophobic treatment on the selectivity of the electroreduction in the absence of a MPL.[61] The discrepancies of the presented studies from the literature and the study in this chapter may be explained by the different use cases. In PEMFCs, the cathode was operated within a membrane electrode assembly (MEA), where water, as a reaction product, had to be released with the outlet gas on the backside of the GDE, similar to the CO removal in the electroreduction of CO_2 to CO. However, in our setup, releasing formate towards the liquid electrolyte on the front side of the GDE is desired.

Effect of the Microporous Layer (MPL)

Based on the results in this chapter, incorporating a MPL significantly enhanced the GDE performance in Toray Paper GDEs. Especially for the cathodic current density, the presence of an MPL increased the GDE performance by up to 18 times compared to GDEs without MPL. For instance, the TP-060 MPL (30%) GDE

showed a cathodic current density of 148.1 ± 22 $mA \cdot cm^{-2}$ in Run 3, whereas the TP-060 (30%) GDE showed only −8.2 ± 1 $mA \cdot cm^{-2}$ at the same electrode potential (**Figure 19**). In turn, the higher cathodic current densities allow for higher product concentrations in the electrolyte (**Figure 21**) or, vice versa, lower electrode potentials for a certain current density (**Figure 20 a**). However, considering the FEs for formate with the Toray Paper GDEs, a GDE with MPL may not outperform a GDE without MPL at any rate. As shown by **Figure 20 b**, the FEs for the GDEs based on Toray Paper appear to show an optimum of around −1.2 ± 0.05 V_{RHE}, which is yet to be achieved by even higher cathodic current densities for GDEs with MPL. Despite the promising results obtained with the Toray Paper GDLs with MPL, the results obtained with GDEs based on Freudenberg GDLs come to a different conclusion. Here, the decisive factor for high FEs for formate is not the presence of a MPL. The FB-E20H obtains the highest FE for formate compared to all investigated GDLs, ranging from 91 ± 9.1% at −36 $mA \cdot cm^{-2}$ up to 100 ± 10% at −107 $mA \cdot cm^{-2}$. Meanwhile, the other Freudenberg GDLs with MPL obtain FEs for formate up to 78 ± 7.8% at −36 $mA \cdot cm^{-2}$ (FB-H23C2) and 82 ± 8.2% at −107 $mA \cdot cm^{-2}$ (FB-H23C6) and are therefore comparable to the results obtained with the Toray Paper GDEs, but much lower than those obtained with FB-E20H.

The significantly improved performance of GDEs with MPL compared to GDEs without MPL can be attributed to several factors. These include altered electrode wetting, improved electrical connectivity of the catalyst, and better CO_2 distribution within the GDE. In this chapter, the enhanced performance of GDEs with MPL is primarily due to the MPL acting as a physical barrier for the catalyst nanoparticles during deposition, as observed by XCT. This results in a focused catalyst layer on top of the GDE surface (**Figure 22 a**), ensuring good contact with the electrolyte (**Figure 22 b**). In contrast, GDEs without MPL have an open GDL structure that allows catalyst particles to penetrate deeply into the inner GDL volume (**Figure 22 c**), where they can be less accessible to the electrolyte (**Figure 22 d**). These findings align with previous research on the effects of MPL on electrolyte flooding and the selectivity of CO_2 electrolysis to CO.[61,70] In that study, Ag particles were focused on the GDE surface in the presence of an MPL, whereas without a MPL,

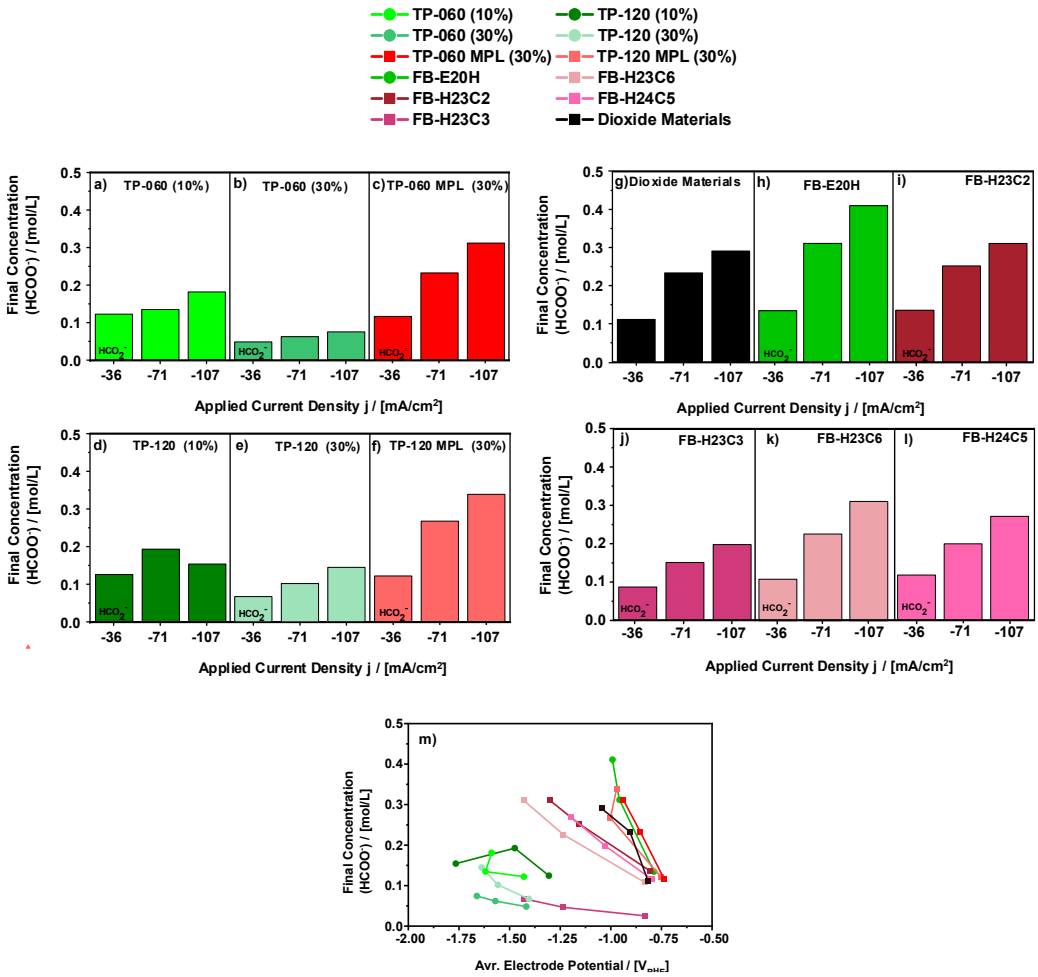


Figure 21. Effect of the gas diffusion layer (GDL) on the final concentration of format in the catholyte after 45 min of CO_2 electroreduction. a-g) Final concentration of formate at different current densities ranging from –36 to –107 mA·cm^{-2}. h) Evolution of the final concentration depending on the resulting electrode potential. Partly reproduced from [3], enabled by the Creative Commons CC-BY license (https://creativecommons.org/licenses/by/4.0/).

catalyst particles penetrated deeper into the carbon fibre support.[70] Additionally, a lower hydrophobicity, indicated by the contact angle measurements after electroreduction (**Table 6**), may also benefit GDE performance. Lower hydrophobicity facilitates complete wetting of the catalyst layer, which can enhance CO_2 electroreduction if the catalyst loading is optimised.[175] Nonetheless, maintaining higher initial hydrophobicity could potentially increase the GDE performance in terms of current density or FE for formate.

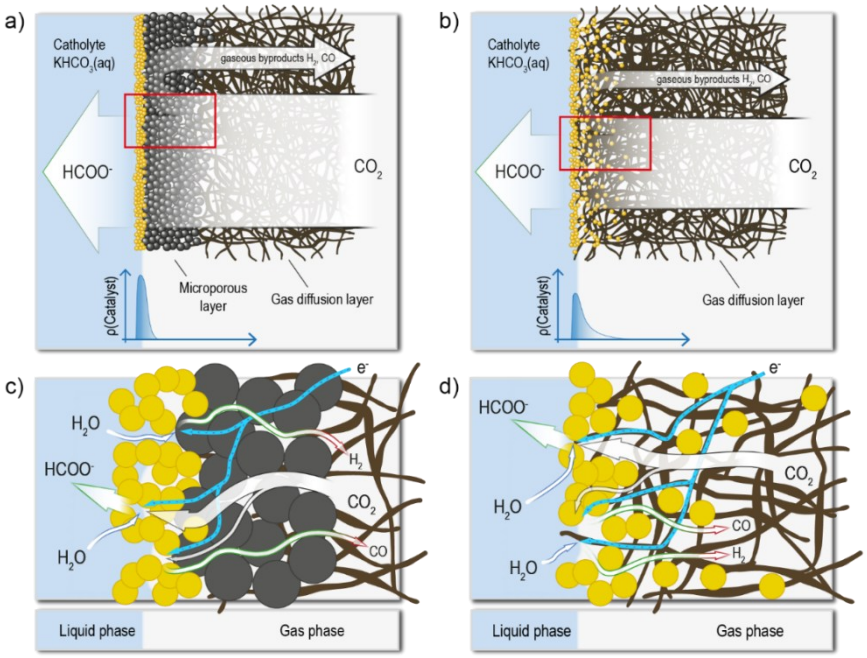


Figure 22. Schematic illustration of the reaction conditions on the investigated gas diffusion electrodes (GDEs) in this dissertation. a) GDE with a microporous layer (MPL) that leads to a focused catalyst layer on the GDE surface. b) GDE without MPL, thus, missing physical barrier for the catalyst nanoparticles (SnO_2, shown yellow) during the GDE manufacturing. c) Detailed schematic for the reaction interface of a GDE with MPL and a catholyte. (Most catalyst nanoparticles are in contact with the catholyte.) d) Detailed schematic for the reaction interface of a GDE without MPL and a catholyte. (In this case, some nanoparticles are lost for the reaction since they are not in contact with the catholyte.) Reproduced from [3], enabled by the Creative Commons CC-BY license (https://creativecommons.org/licenses/by/4.0/).

Furthermore, in **Table 8**, the electrical conductivity before electrochemical testing for Toray Carbon Paper GDEs with MPL is about one order of magnitude higher than the conductivity for the GDEs without MPL. The latter allows for lower electrode potentials at the same current density, aligning with previous research.[176] However, the Freudenberg GDEs show different results: the FB-E20H has the highest through-plane conductivity among all investigated GDLs, resulting in avr. electrode potentials similar to GDLs with MPL. For the Toray Paper GDLs, a significant difference in through-plane conductivity between GDEs with and without MPL is retrieved in the pristine state, which is then altered due to changes during the electrochemical reduction of CO_2. Meanwhile, the FB-E20H obtains the highest through-plane conductivity. The perceived benefit of the Toray Carbon Paper GDEs

with MPL regarding electrical connectivity between the catalyst and GDL appeared only in the PEIS measurements (**Table 9**). Here, TP-060 and 120 MPL (30%) GDEs start with relatively low internal resistances of 0.50 ± 0.05 and 0.51 ± 0.05 $\Omega \cdot cm^{-2}$, respectively, and decrease slightly to 0.49 ± 0.05 $\Omega \cdot cm^{-2}$ each.

Reviewing the present results, there is a strong agreement in the literature that GDEs with MPL perform significantly better than GDEs without MPL.[61,67,70] For instance, a study on the effects of MPL on electrolyte flooding and the selectivity of CO_2 electrolysis to CO showed that GDEs with MPL outperform GDEs without MPL. This difference was linked to flooding issues in GDEs without MPL.[70] Additionally, earlier research with different substrates showed limited conversion efficiency to CO and a limited partial current density towards CO without a MPL.[67] Therefore, the results in this chapter for the Toray Carbon Paper GDLs align with previous research and add new insights through focused investigations into CO_2 electroreduction to formate. The results indicate similar trends regarding optimal GDL choice, though the impact varies with the desired product.[177] Unlike previous studies,[172] even GDEs without MPL could be tested extensively without flooding under current experimental conditions. During these tests, GDEs still produced a reasonable amount of product, albeit at a higher electrode potential.

The remarkable results obtained with FB-E20H (a unique Freudenberg GDL without MPL) are due to its very high through-plane conductivity across all three investigated states (GDL, pristine GDE and after electrochemical measurements). This is likely the main reason it performs the best in this chapter. Additionally, this could explain why, for the Freudenberg GDLs, the extent of the MPL's impact on the electrode's performance is not given. Therefore, based on the results in this chapter and the potential for further improving the electrode's performance concerning avr. electrode potential and the obtained FEs for formate, FB-E20H is selected as GDL for the further measurements conducted in this thesis.

4.2 Early-Stage Performance Changes of Gas Diffusion Electrodes for Electroreduction to Formate

The results of this chapter, "Early-Stage Performance Change of Gas Diffusion Electrodes for Electroreduction to Formate", are published in Sustainable Energy & Fuels by the Royal Society of Chemistry (DOI: 10.1039/D3SE01347B).[2] This publication is published under a CC-BY 4.0 license. A. Kretzschmar conducted Vapor Sorption measurements, and S. Ziemer conducted the TGA measurements.

Although the GDE technology is quite advanced in other electrochemical processes, such as water electrolysis,[17,20–22] in the field of CO_2 electroreduction, it faces severe problems regarding long-term stability and electrode degradation.[52,121] This instability of GDEs for CO_2 electroreduction is mostly based on the unique requirements of this specific reaction, where products, different to water electrolysis, in two physical states (gaseous and liquid), are formed simultaneously.[20,23] Furthermore, the nature of evolving products, such as formic acid and ethanol, alters surface wetting, which may lead to electrode flooding due to the enrichment of these low-surface-tension liquid products.[24] In this chapter, therefore, a study on the early-stage performance change of GDEs, based on the influence of catalyst loading on the electroreduction of CO_2 to formate, is reported. To implement this study, custom-made GDEs with different catalyst loadings from 1.1 to 13 $mg \cdot cm^{-2}$ (see **Table 3**) are investigated.

4.2.1 Influence of the catalyst loading and repeated cycling on the electrode performance

To elucidate the influence of the catalyst loading on the electroreduction of CO_2 to formate, gas diffusion electrodes (GDEs) at six different catalyst loadings were prepared (from 1.1 to 13 mg·cm^{-2}, see **Table 3**) and tested with increasing cathodic current densities.

Concerning the influence of the catalyst loading on the avr. electrode potential, two regimes are discernible, which are depicted in **Figure 23**. In regime I, for catalyst loadings ≤ 2.3 mg·cm^{-2}, the avr. electrode potential upon the electroreduction of CO_2 becomes more positive with increasing catalyst loading. In regime II, concerning catalyst loadings > 2.3 mg·cm^{-2}, the avr. electrode potential stays almost constant in the same range. These two regimes are particularly observable at 36 mA·cm^{-2}; the lowest catalyst loading of 1.1 mg.cm^{-2} leads to the most negative avr. electrode potential of –0.99 ± 0.05 V_{RHE}, while 2.3 mg·cm^{-2} leads to a 200 mV more positive avr. electrode potential of –0.79 ± 0.05 V_{RHE}. On the other hand, the obtained avr. electrode potentials for the catalyst loadings of 4.2 and 13 mg·cm^{-2} are at –0.77 ± 0.05 V_{RHE} for both, respectively. Thus, the lowest catalyst loading leads to the most negative electrode potential.

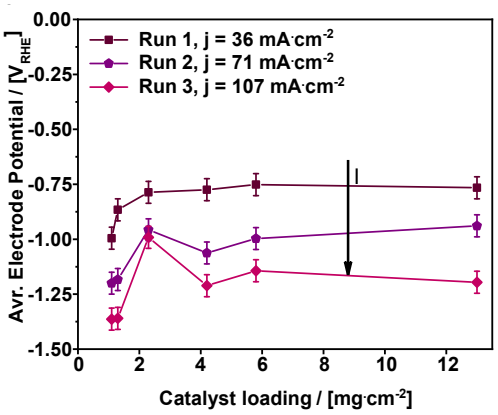


Figure 23. Influence of the catalyst loading on the avr. electrode potential for three different applied current densities (36, 71, and 107 mA·cm^{-2}. Measurement conditions: batch reactor, 12 ml electrolyte, 1 M $KHCO_3$, continuous CO_2 supply of 20 ml·min^{-1}, start at room temperature, electrolysis time: 45 min each). Reproduced from [2], enabled by the Creative Commons CC-BY license (https://creativecommons.org/licenses/by/4.0/).

In addition to the influence of catalyst loading, the effect of the different applied cathodic current densities was also given. With the increasing current densities (36, 71

and 107 $mA \cdot cm^{-2}$), the electrode potentials become more negative. This behaviour can be attributed to increased electrode polarisation due to higher currents.[178–180] An exception to this trend seems to be the GDE with a catalyst loading of 2.3 $mg \cdot cm^{-2}$. In this case, the obtained avr. electrode potential initially increases by 170 mV, from –0.79 ± 0.05 V_{RHE} to –0.96 ± 0.05 V_{RHE}, as the current density varies from 36 to 71 $mA \cdot cm^{-2}$. However, when the current density was further increased to 107 $mA \cdot cm^{-2}$, the potential remained constant at –0.97 ± 0.05 V_{RHE}. Consequently, the most positive avr. electrode potentials are obtained for catalyst loadings of ≥ 2.3 $mg \cdot cm^{-2}$. A comparison of the results presented in **Figure 23** with those from the literature reveals a comparable trend regarding the impact of catalyst loading on electrode performance.[64] In this context, the presence of a thicker catalyst layer has been observed to result in lower electrode potentials for a given current density. This effect can be attributed to an augmented active surface area.

In line with the results obtained in **Figure 23**, the FEs obtained for formate can also be divided into two regimes, shown in **Figure 24**. In Regime I, concerning catalyst loadings ≤ 2.3 $mg \cdot cm^{-2}$, the FE increases with increasing catalyst loading. For catalyst loadings > 2.3 $mg \cdot cm^{-2}$, representing Regime II, the FE decreases with further increasing catalyst loading. An exception to this trend is represented by the GDE with a catalyst loading of 13 $mg \cdot cm^{-2}$, showing a FE almost as high as the FE obtained with the 2.3 $mg \cdot cm^{-2}$ GDE. Thereby, the 13 $mg \cdot cm^{-2}$ GDE shows from Run 1 to Run 3 an increase from 50 ± 5.0% to 100 ± 10.0%, and the 2.3 $mg \cdot cm^{-2}$ GDE an increase from 91 ± 9.1% up to 100 ± 10.0%. Thus, these two catalyst loadings show the highest FE for formate and appear to be the most suitable catalyst loadings for the GDEs in the applied setup.

A possible explanation for the results obtained for GDE with a catalyst loading of 13 $mg \cdot cm^{-2}$ appears to be structural changes of the electrode as part of a run-in phase. The structural changes become evident when comparing FEs for the catalyst loadings 4.2 and 13 $mg \cdot cm^{-2}$ between Run 1 and

Run 3 in **Figure 24**. In Run 1, both catalyst loadings allow similar FE for formate of ca. 50%. In Run 3, the FE for 13 mg·cm^{-2} reaches up to 100 ± 10%, whereas for 4.2 mg·cm^{-2}, 76 ± 7.6% is observed. A detailed investigation of the structural changes will be addressed in the part on physical reasons for the run-in phase at the end of this chapter.

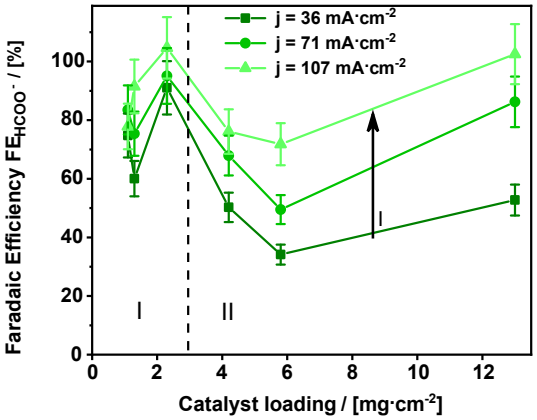


Figure 24. Influence of the catalyst loading on the FE for formate after a run time of 11 min each. (Measurement conditions: batch reactor, 12 ml electrolyte, 1 M $KHCO_3$, continuous CO_2 supply of 20 ml·min^{-1}, start at room temperature, electrolysis time: 45 min each). Reproduced from [2], enabled by the Creative Commons CC-BY license (https://creativecommons.org/licenses/by/4.0/).

Based on the observations above, a prior study found that changing the catalyst layer composition affects either CO_2 concentration gradient across the layer or the pH within it, depending on the distance from the GDL. Increasing catalyst loading extends the mean path for CO_2 and HCO_3^- transport through the thicker catalyst layer, creating zones of high alkalinity and CO_2 depletion. This, in turn, suppresses pH-sensitive products like $HCOO^-$, and leads to increased CO release. Additionally, variations in Nafion content produced similar effects; however, high Nafion loading seemed to act more as a barrier to CO_2 reaching the catalytic sites than simply increasing the transport path.[181] Such mass transport hindrance can be explained by slower through-plane transport of reactants (CO_2 and HCO_3^-), favouring HER. These phenomena were also evident in our experiments, as shown in **Figure 25**.

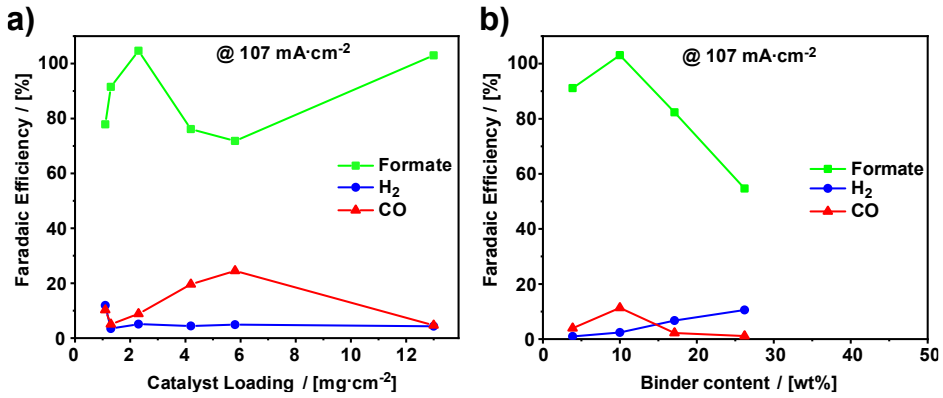


Figure 25. Influence of the catalyst loading (a) and the binder content (b) at the FE of the evolving products. (Catalyst loading: 2.3 mg·cm^{-2}, measurement conditions: batch reactor, 12 ml electrolyte, 1 M $KHCO_3$, continuous CO_2 supply of 20 ml·min^{-1}, start at room temperature, electrolysis time: 45 min each). Reproduced from [2], enabled by the Creative Commons CC-BY license (https://creativecommons.org/licenses/by/4.0/).

Regarding the influence of the applied cathodic current density on the obtained FEs for formate, a significant impact is especially discernible for the catalyst loadings > 2.3 mg·cm^{-2}. The highest FE is obtained at the highest cathodic current density; hence, 107 mA·cm^{-2} leads to the most favourable electrode potential investigated in this study. Similar effects have been observed in the literature, where at current densities up to 100 mA·cm^{-2}, an increase of FE was observed, followed by a decrease for higher current densities due to the favoured HER.[182]

Figure 26 depicts the presence of a preferential electrode potential range for formate production. If FEs > 70% are taken into account for this consideration, an electrode potential range between -1.10 ± 0.05 V_{RHE} and -1.40 ± 0.05 V_{RHE} appears to be most favourable for formate production. Starting from the 1.1 mg·cm^{-2} GDE with a maximum FE of 84 ± 8.4% at –1.20 ±

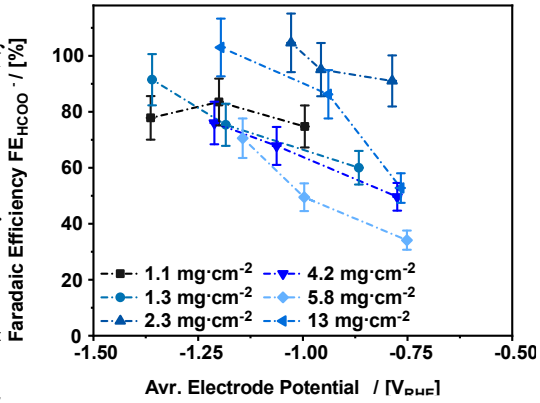


Figure 26. Graphical representation of the influence of the avr. electrode potential on the obtained FE for formate. Created from the data in Figures 20 and 21. Reproduced from [2], enabled by the Creative Commons CC-BY license (https://creativecommons.org/licenses/by/4.0/).

0.05 V_{RHE}, the other GDEs obtain max. FEs (70 ± 7.0% to 100 ± 10%) in a potential range from –1.10 ± 0.05 V_{RHE} to –1.40 ± 0.05 V_{RHE}. In a previous study on SnO_2 nanosheets as a catalyst for CO_2 electroreduction to formate, as well an optimum electrode potential between –1.0 and –1.2 V_{RHE} was observed.[183] Furthermore, in the electroreduction of CO_2 on Cu catalysts, the applied electrode potential determines which product range is obtained.[29]

Additionally, LSV scans were performed prior to each electrolysis run as a direct indicator of the GDE stability. **Figure 27 a** depicts the results of the third of three scans from OCV to −1.24 V_{RHE} for the 13 $mg \cdot cm^{-2}$ GDE. Furthermore, **Figure 27 b** demonstrates the impact of the catalyst loading on the cathodic current density at −1.15 V_{RHE} (blue line in **Figure 27 a**). Based on the course of the LSVs in **Figure 27 a**, the influence of repeated scanning can be described as shifting the CO_2RR onset to about –0.55 V_{RHE} more negative potentials and decreasing the cathodic current density.

Analysis of the cathodic current density at −1.15 V_{RHE} shows two distinct regimes (see **Figure 27 b)**. For catalyst loadings ≤ 2.3 $mg \cdot cm^{-2}$, cathodic current density increases, whereas for catalyst loadings > 2.3 $mg \cdot cm^{-2}$, it remains relatively constant. In the first run, the lowest cathodic current density, 55 ± 11 $mA \cdot cm^{-2}$, is obtained for the lowest catalyst loading, 1.1 $mg \cdot cm^{-2}$. At 2.3 $mg \cdot cm^{-2}$, the cathodic current density triples to 165 ± 33 $mA \cdot cm^{-2}$. For the catalyst loadings 4.2 and 13 $mg \cdot cm^{-2}$ the cathodic current density varies only about 10 $mA \cdot cm^{-2}$, from 137 ± 27 to 127 ± 25 $mA \cdot cm^{-2}$, respectively. This pattern persists in subsequent LSV scans. Consistent with **Figure 23** and previous literature, these results indicate that a high catalyst loading is not the key factor in reaching a high cathodic current density for the CO_2 electroreduction to formate.[73,182] Repeated use of GDEs reveals significant changes in the cathodic current density, suggesting a run-in phase of the catalyst during the electroreduction of CO_2. The exception is the GDE with the lowest catalyst loading (1.1 $mg \cdot cm^{-2}$), where the cathodic current density remains constant at around 60 ± 12 $mA \cdot cm^{-2}$. To better understand these effects, the two

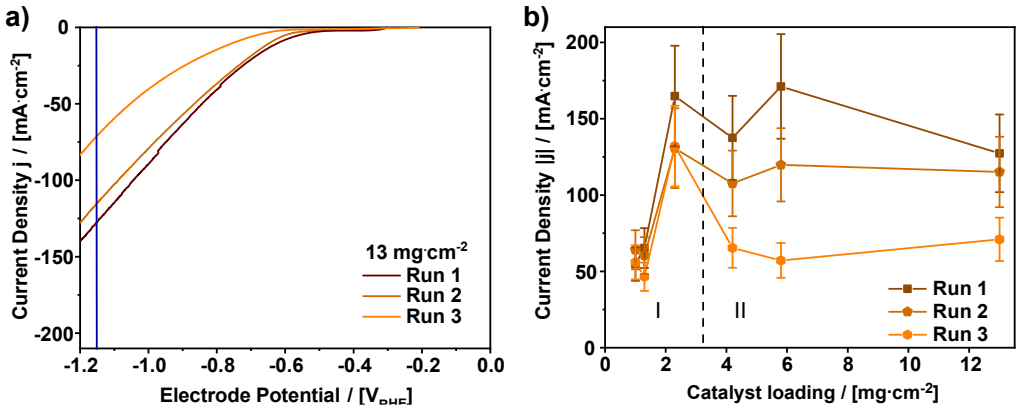


Figure 27. (a) Exemplary course of the linear sweep voltammograms (LSVs) for the GDE with a catalyst loading of 13 mg·cm^{-2}. (b) Evaluation of the cathodic current density at –1.15 V_{RHE} depending on the catalyst loading. (Measurement conditions: batch reactor, 12 ml electrolyte, 1 M $KHCO_3$, continuous CO_2 supply of 20 ml·min^{-1}, start at room temperature, electrolysis time: 45 min each). Reproduced from [2], enabled by the Creative Commons CC-BY license (https://creativecommons.org/licenses/by/4.0/).

best performing electrodes in terms of observed FE, 2.3 and 13 mg·cm^{-2}, were subjected to a second test cycle, using the same procedure as in **Figure 28.**

Comparing the results of the LSV scans between cycles 1 and 2 at –1.15 V_{RHE} reveals a drop in cathodic current density for both investigated catalyst loadings (see **Figure 28 a**). For the 2.3 mg·cm^{-2} GDE, the decrease of the cathodic current density is around 25%, from 170 ± 34 mA·cm^{-2} to 20 ± 24 mA·cm^{-2}. The 13 mg·cm^{-2} GDE demonstrates an even more pronounced decrease, with a drop of 52%, from 130 ± 26 mA·cm^{-2} to 70 ± 14 mA·cm^{-2}. However, in cycle 2, the obtained cathodic current densities remain constant at slightly lower values, i.e., 115 ± 23 mA·cm^{-2} for the 2.3 mg·cm^{-2} and 70 ± 14 mA·cm^{-2} for the 13 mg·cm^{-2} GDE. Therefore, the decrease in cathodic current density is not sustained and appears to be limited to the first cycle. This further supports the hypothesis of a run-in phase occurring.

Evaluating the GDEs further, **Figure 28 b** shows the influence of the GDE change on electrode performance upon repeated cycling. Comparing the

results for the GDE at 36 mA·cm^{-2} between cycles 1 and 2 for the catalyst loading 2.3 mg·cm$^{-2,}$ a drop in the electrode potential by 10% is shown. However, at 71 and 107 mA·cm^{-2}, the electrode potentials are constant around –0.95 ± 0.05 V_{RHE}. For the 13 mg·cm^{-2} GDE, however, a more severe drop in electrode potential is apparent between cycles 1 and 2. Here the avr. electrode potential in cycle 2 is up to 25% more negative than in cycle 1, and for example, at 36 mA·cm^{-2}, it drops from –0.77 ± 0.05 V_{RHE} in cycle 1 to–1.25 ± 0.05 V_{RHE} in cycle 2.

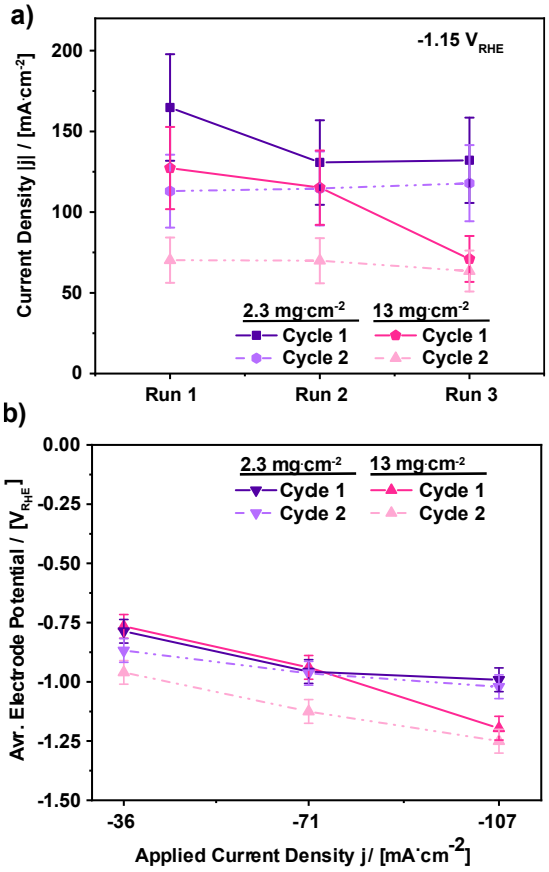


Figure 28. (a) Evaluation of the cathodic current density at –1.15 V_{RHE} to determine the influence of repeated cycling on the GDE stability for a GDE catalyst loading of 2.3 and 13 mg·cm^{-2}. (b) Comparison of the avr. electrode potential for three current densities (36, 71 and 107 mA·cm^{-2}). (Measurement conditions: batch reactor, 12 ml electrolyte, 1 M $KHCO_3$, continuous CO_2 supply of 20 ml·min^{-1}, start at room temperature, electrolysis time: 45 min each). Reproduced from [2], enabled by the Creative Commons CC-BY license (https://creativecommons.org/licenses/by/4.0/).

With regard to the FE towards formate, as illustrated in **Figure 29**, both GDEs demonstrate an increasing FE with increasing applied current density in the first cycle. However, in the second cycle, the changes are inconsistent. For the GDE with a catalyst loading of 2.3 mg·cm^{-2}, a decrease in FE of up to 15% occurs, from 91 ± 9.1% to 76 ± 7.6% at 36 mA·cm^{-2}, from 95 ± 9.5% to 90 ± 9.0% at 71 mA·cm^{-2} and from 104 ± 10.4% to 89 ± 8.9% at 107 mA·cm^{-2}. On the other hand, for the GDE with 13 mg·cm^{-2} catalyst loading, first an increase of 50% is observed at

36 mA·cm^{-2}, from 53 ± 5.3% to 99 ± 9.9%, followed by stagnation around 86 ± 8.6% at 71 mA·cm^{-2} and a decrease of –15% from 103 ± 10.3% to 91 ± 9.1% at 107 mA·cm^{-2}. In conjunction with **Figure 29**, it can therefore be concluded that the performance of the GDEs in terms of FE decreases between cycle 1 and cycle 2, but appears to remain constant within the second cycle, regardless of the current density. This leads to the conclusion that a run-in phase of the GDEs occurs during the first cycle.

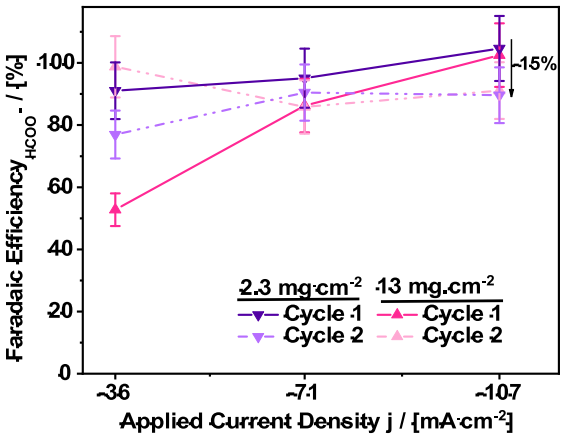


Figure 29. FE of formate after a run time of 11 min each obtained from the CO_2 electroreduction reaction shown in Figure 25. (Measurement conditions: batch reactor, 12 ml electrolyte, 1 M $KHCO_3$, continuous CO_2 supply of 20 ml·min^{-1}, start at room temperature, electrolysis time: 45 min each). Reproduced from [2], enabled by the Creative Commons CC-BY license (https://creativecommons.org/licenses/by/4.0/).

4.2.2 Physical reason for the run-in phase

Elucidating the physical reason for the run-in phase, further investigations of the GDEs were carried out, using scanning electron microscopy (SEM), Raman spectroscopy, contact angle (CA) measurements, vapor sorption measurements and thermogravimetric analysis (TGA). **Figure 30** shows the topography of the GDEs before the electrochemical measurements. Increasing the catalyst loading results in a continuous coverage of the GDL by the catalyst. At 2.3 mg·cm^{-2} (**Figure 30 d**), the original fibre structure of the GDL is still visible, showing how the catalyst layer follows the carbon fibre pattern. However, at 13 mg·cm^{-2} (**Figure 30 g**), the substrate is completely covered by a continuous layer. The increase in catalyst coverage can be described as continuous for catalyst loadings ≥ 4.2 mg·cm^{-2}, which is consistent with the

literature.[182] Furthermore, in addition to the increasing coverage with SnO_2, there are cracks in the catalyst layer at catalyst loadings ≥ 4.2 mg·cm^{-2}. These cracks are most probably a result of the drying process during the catalyst deposition.[184] Further analysis of the SEM images in **Figure 31 a) -f)** after cycle 1 reveals catalyst agglomeration. However, while at 2.3 mg·cm^{-2}, the agglomeration is limited to small agglomerates with diameters under 10 µm, larger agglomerates appear with increasing catalyst loading. The largest agglomerates, measuring around 50 µm, are found in the 13 mg·cm^{-2} GDE. Due to the agglomeration of the catalyst layer, holes and indentations are observed, especially along the course of the carbon fibres. Thus, the carbon fibres appear to act as initiators of changes in the catalyst layer, as the current passing through them provides the impetus for the change. Comparing this with the 1.1 mg·cm^{-2} GDE shows that agglomeration also occurs for the lowest catalyst loading, with the catalyst particles appearing to be centred in the

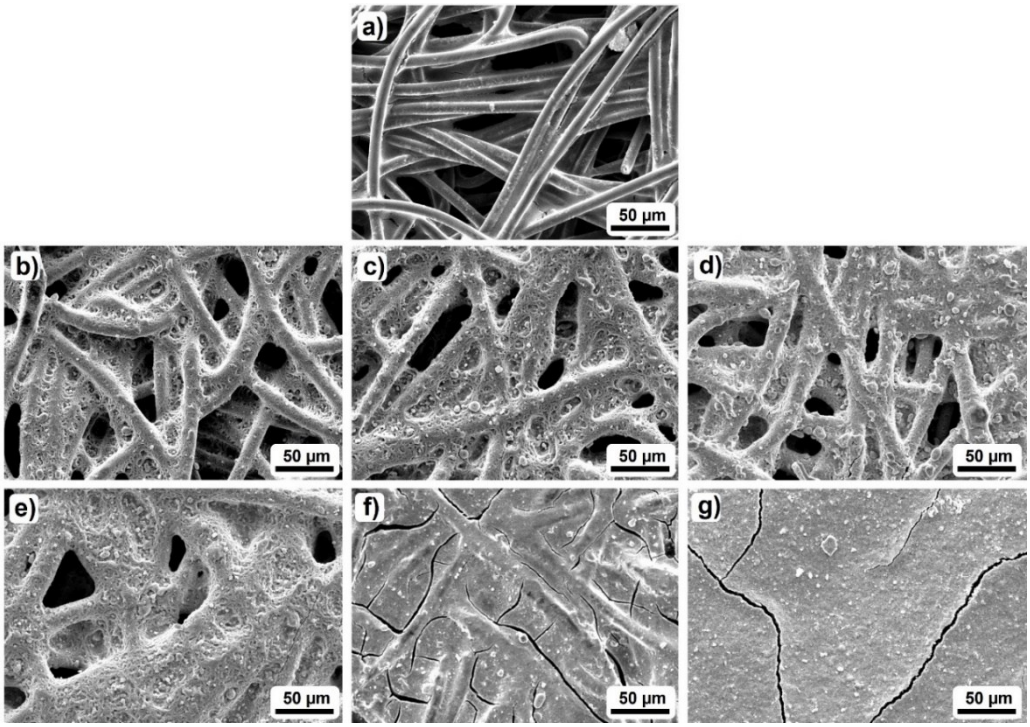


Figure 30. SEM images of the investigated GDEs concerning the influence of the catalyst loading before the electroreduction of CO_2 at 550x magnification, a) Freudenberg E20H GDL, b) 1.1 mg·cm^{-2}, c) 1.3 mg·cm^{-2}, d) 2.3 mg·cm^{-2}, e) 4.2 mg·cm^{-2}, f) 5.8 mg·cm^{-2}, g) 13 mg·cm^{-2}. Reproduced from [2], enabled by the Creative Commons CC-BY license (https://creativecommons.org/licenses/by/4.0/).

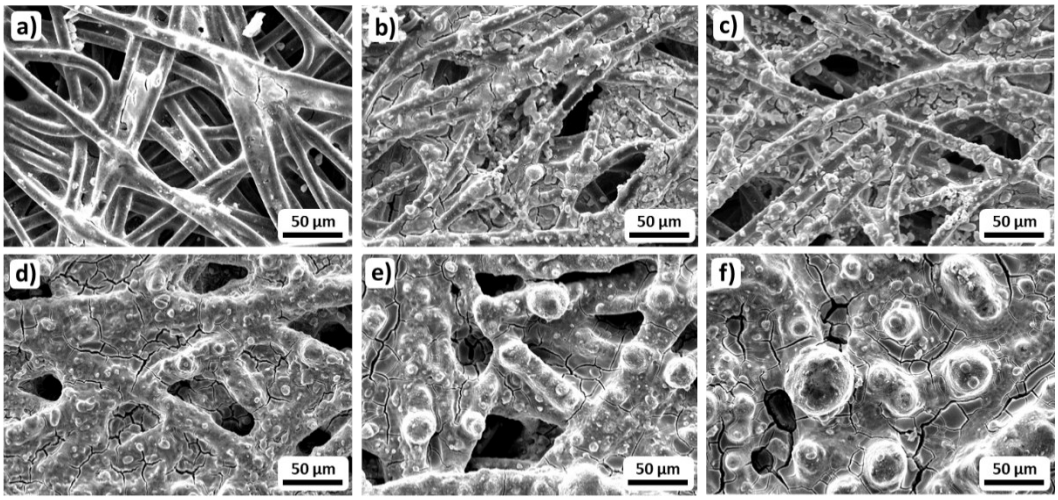


Figure 31. SEM images of the investigated GDEs concerning the influence of the catalyst loading after the first cycle electroreduction of CO_2 at 550x magnification, a) 1.1 mg·cm^{-2}, b) 1.3 mg·cm^{-2}, c) 2.3 mg·cm^{-2}, d) 4.2 mg·cm^{-2}, e) 5.8 mg·cm^{-2}, f) 13 mg·cm^{-2} . Reproduced from [2], enabled by the Creative Commons CC-BY license (https://creativecommons.org/licenses/by/4.0/).

interspace between the individual carbon fibres. Furthermore, considering the additional SEM cross-sections in **Figure 32**, it can be concluded that, in addition to the catalyst agglomeration, catalyst migration into deeper GDL layers also occurs for electrodes with a catalyst loading > 2.3 mg·cm^{-2}. This migration could lead to a loss of catalyst nanoparticles in contact with the electrolyte.[3] Therefore, the observed agglomeration and catalyst migration result in changes to the topography of the catalyst layer, which in turn affects the available active surface area of the catalyst. This is especially evident in **Figure 24**, which shows the effect of the catalyst loading on the FE. For catalyst loadings > 2.3 mg·cm^{-2}, a decrease in FE is observed, while the 13 mg·cm^{-2} GDE obtains similar results to 2.3 mg·cm^{-2} GDE. One possible explanation for this effect is that sufficient catalyst remains available in the first layer of the GDL. Due to agglomeration and catalyst migration, the amount of accessible active surface area decreases, which could explain the decrease in FE for catalyst loadings >2.3 mg·cm^{-2}. However, in the case of the 2.3 and 13 mg·cm^{-2} GDE, the amount of accessible active surface area appears to converge, resulting in similar FE obtained.

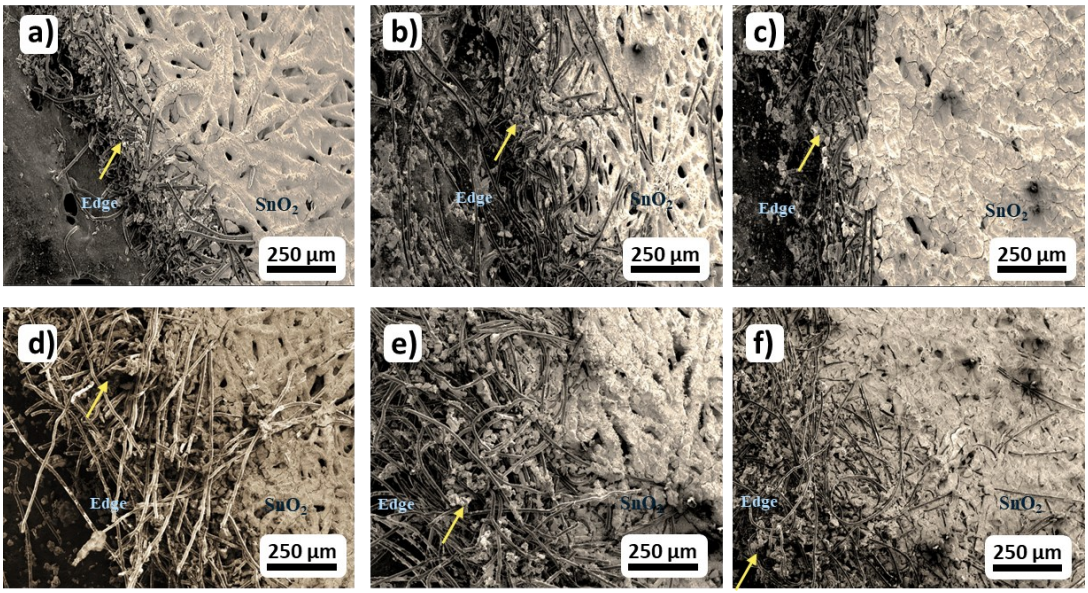


Figure 32. SEM cross sections of the investigated GDEs (catalyst loading > 2.3 mg·cm^{-2}) concerning the influence of the catalyst loading in the pristine state and after the first cycle electroreduction of CO_2 at 250x magnification, a),d) 4.2 mg·cm^{-2}, b), e) 5.6 mg·cm^{-2} and c), f) 13 mg·cm^{-2}. For a better visualisation, the fracture edges and the catalyst layer are labelled as edges and SnO_2, respectively, as well as arrows indicating the catalyst in the deeper layers. Reproduced from [2], enabled by the Creative Commons CC-BY license (https://creativecommons.org/licenses/by/4.0/).

Figure 33 shows the further changes of surface topography during cycle 2. In case of the catalyst loading 2.3 mg·cm^{-2}, a smoothing effect occurred, resulting in even more visible carbon fibres. This smoothing is accompanied by a noticeable decrease in the active catalyst surface area. However, at 13 mg·cm^{-2}, the opposite effect occurs, a much rougher surface is the result. This reorganisation of the catalyst layer topography could also explain the results in **Figure 28 b**: an increase in performance was observed for the 13 mg·cm^{-2} GDE, while a decreasing performance was observed for the 2.3 mg·cm^{-2} GDE.

Additionally, based on the reorganisation of the GDE topography, the carbon fibres appear to become increasingly exposed to the electrolyte. This increasing exposure could lead to increased HER and GDL dissolution upon continued use. Especially, GDL dissolution triggered by surface-oxide formation in the presence of a liquid electrolyte can lead to severe GDE alteration.[121] This could result in a reduction in the hydrophobicity of the GDL[64]

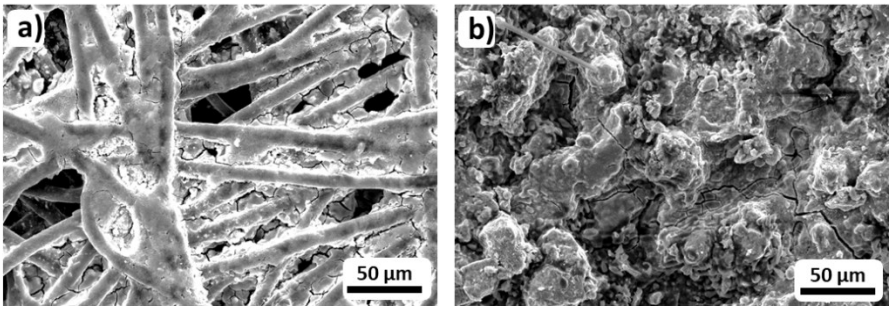


Figure 33. SEM images of the investigated GDEs after repeated cycling: (a) 2.3 mg·cm^{-2} and (b) 13 mg·cm^{-2}.Reproduced from [2], enabled by the Creative Commons CC-BY license (https://creativecommons.org/licenses/by/4.0/).

and a loss of carbon from the electrode due to the eventual conversion of the oxidised graphene particles into CO_2.[121] However, GDL dissolution is not apparent in the presented state of the GDEs.

Raman spectroscopy measurements of the GDEs were conducted after repeated cycling to determine if a change in the composition of the GDEs during CO_2 electroreduction occurs. This revealed distinct differences between the GDEs in the different states, i.e., pristine state and after cycle 2, see **Figure 34**. For the pristine GDEs, the Raman spectra are mainly governed by the response of the catalyst layer (i.e., the catalyst and the binder: SnO_2 and Nafion). The Raman spectrum of SnO_2 typically consists of three bands: at 470 cm^{-1} (E_g), 630 cm^{-1} (A_{1g}) and 770 cm^{-1} (B_{2g}), representing the classical modes of SnO_2.[185] Additionally also disordered activated surface modes can occur for SnO_2 as broad peaks in a region from 475 to 775 cm^{-1} (S1, S2 and S3). These defect modes depend on the nanoparticle size and can be seen in the pristine state for both GDEs at 570 cm^{-1} (S1).[186] The remaining Raman bands in **Figure 34** can be attributed to Nafion, which has four specific bands: at 292 cm^{-1} (A_1), 385 cm^{-1} (A_t), 731 cm^{-1} (A_1) and 971 cm^{-1}.[187]

Comparing the Raman spectra of the pristine GDEs to the GDEs after cycle 2, the SnO_2 bands at 570 cm^{-1} (S1) and 630 cm^{-1} (A_{1g}) change. This change is most probably attributable to the reduction of SnO_2 to metallic Sn^0 with a still prevalent $Sn^{IV}O_2$.[28] Additionally, the broad peak at 570 cm^{-1} can be ascribed to amorphous hydrous $Sn^{IV}O_2$, which further supports the morphological changes observed in the SEM images after cycle 2.[188]

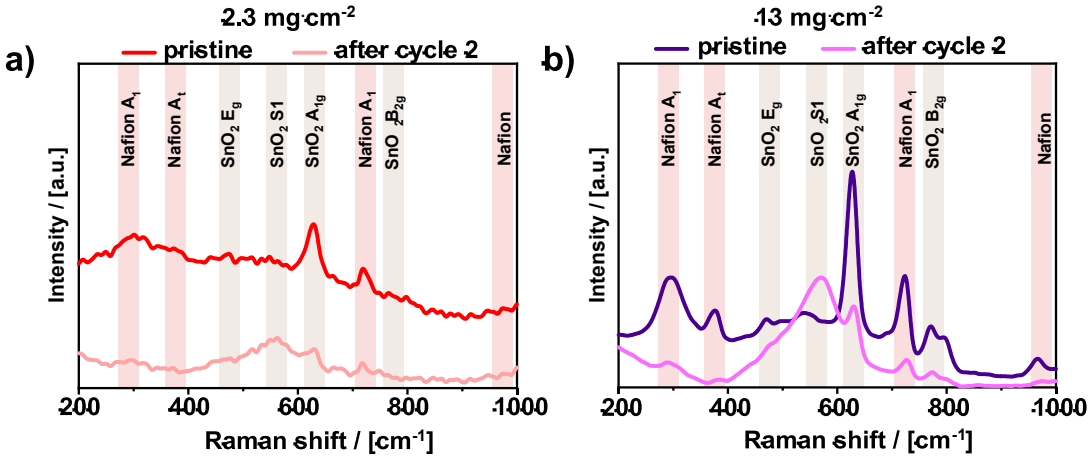


Figure 34. Raman spectra for the investigated GDEs before and after CO_2 electroreduction with a catalyst loading of (a) 2.3 mg·cm^{-2} and (b) 13 mg·cm^{-2}. (Incident wavelength: 532 nm, spectra normalised to the highest vibration). Reproduced from [2], enabled by the Creative Commons CC-BY license (https://creativecommons.org/licenses/by/4.0/).

Besides the change of the SnO_2 Raman bands, two more observations in **Figure 34** are present: the Raman bands for Nafion vanish, which could be a result of binder loss during the CO_2 electroreduction, and no carbon formation is detected, given the absence of the corresponding Raman peaks for the GDEs after the measurements.[118,120]

To further illustrate the property changes of the investigated GDEs, **Table 10** provides the contact angles of the pristine GDL, the GDL coated only with Nafion, and the GDEs with increasing catalyst loading before and after CO_2 electroreduction. The GDL itself (catalyst loading: 0 mg·cm^{-2}) has a hydrophobic surface with a contact angle of 137.9 ± 5.0°. However, following the catalyst deposition, the contact angle decreases up to 22°. Another significant impact on the hydrophobicity of the GDEs has the electrochemical experiments. Thereby, after cycle 1, the hydrophobicity decreases up to 40° as in case for the 1.3 and 2.3 mg·cm^{-2} GDEs or do not show hydrophobicity at all, with contact angles <90°C. After cycle 2 of electroreduction of CO_2 experiments, the decrease of hydrophobicity continues even further. For the 2.3 mg·cm^{-2} GDE, the contact angle decreases from 83.5 ± 9.7° to 41.9 ± 6.5°, and for the 13 mg·cm^{-2}, it was no longer possible to measure a contact angle as the applied droplet immediately absorbed into the GDL. The

results of the contact angle measurements thus support the observation of an altered GDE surface, which could involve either a loss or deterioration of Nafion.

Table 10. Comparison of the contact angles (1M $KHCO_3$) for pristine GDL and GDEs to the GDL with Nafion coating only and change of contact angle and of the investigated GDEs as a function of the catalyst loading before and after cycle 1 and cycle 2. (Scattering represents the standard deviation). Reproduced from [2], enabled by the Creative Commons CC-BY license (https://creativecommons.org/licenses/by/4.0/)

Catalyst loading / [mg·cm^{-2}]	GDE (before) [°]	GDE (Nafion coating) [°]	GDE (after cycle 1) [°]	GDE (after cycle 2) [°]
0	137.9 ± 5.0	134.3 ± 1.0	-	-
1.1	119.9 ± 9.8	-	110.9 ± 13.3	-
1.3	125.8 ± 4.5	-	82.1 ± 7.3	-
2.3	126.7 ± 2.7	-	83.5 ± 9.7	41.9 ± 6.5
4.2	126.4 ± 2.5	-	absorbed	-
5.8	115.9 ± 9.7	-	absorbed	-
13	123.2± 1.6	-	absorbed	absorbed

To obtain further information on how the decreased hydrophobicity of the GDE surface also influences the bulk hydrophobicity, vapor sorption measurements were conducted. The vapor adsorption isotherms were obtained at 25°C for the GDEs – pristine, after cycle 1, and after cycle 2, shown in **Figure 35**. The GDEs in the pristine state adsorb up to 0.73 wt% and show the least amount of water uptake. After the first cycle, the water uptake of the GDEs is up to twenty times higher than for the pristine samples. The highest water uptake is obtained with a catalyst loading of 5.8 mg·cm^{-2}, from 0.45 to 8.9 wt% at 80% humidity. With continuing electrochemical measurements, the increase in adsorbed water continues to increase further. After cycle 2, the 13 mg·cm^{-2} GDE shows a 10-fold increase in water adsorption at 80% humidity compared to the pristine state, from 0.74 to 8.2wt%. This observation confirms that the loss of hydrophobicity is not limited to the GDE surface but also extends to the bulk hydrophobicity properties of the GDE.

Furthermore, vapor sorption data can help establish a link between surface wettability, measured by contact angle, and the overall hydrophobicity of the

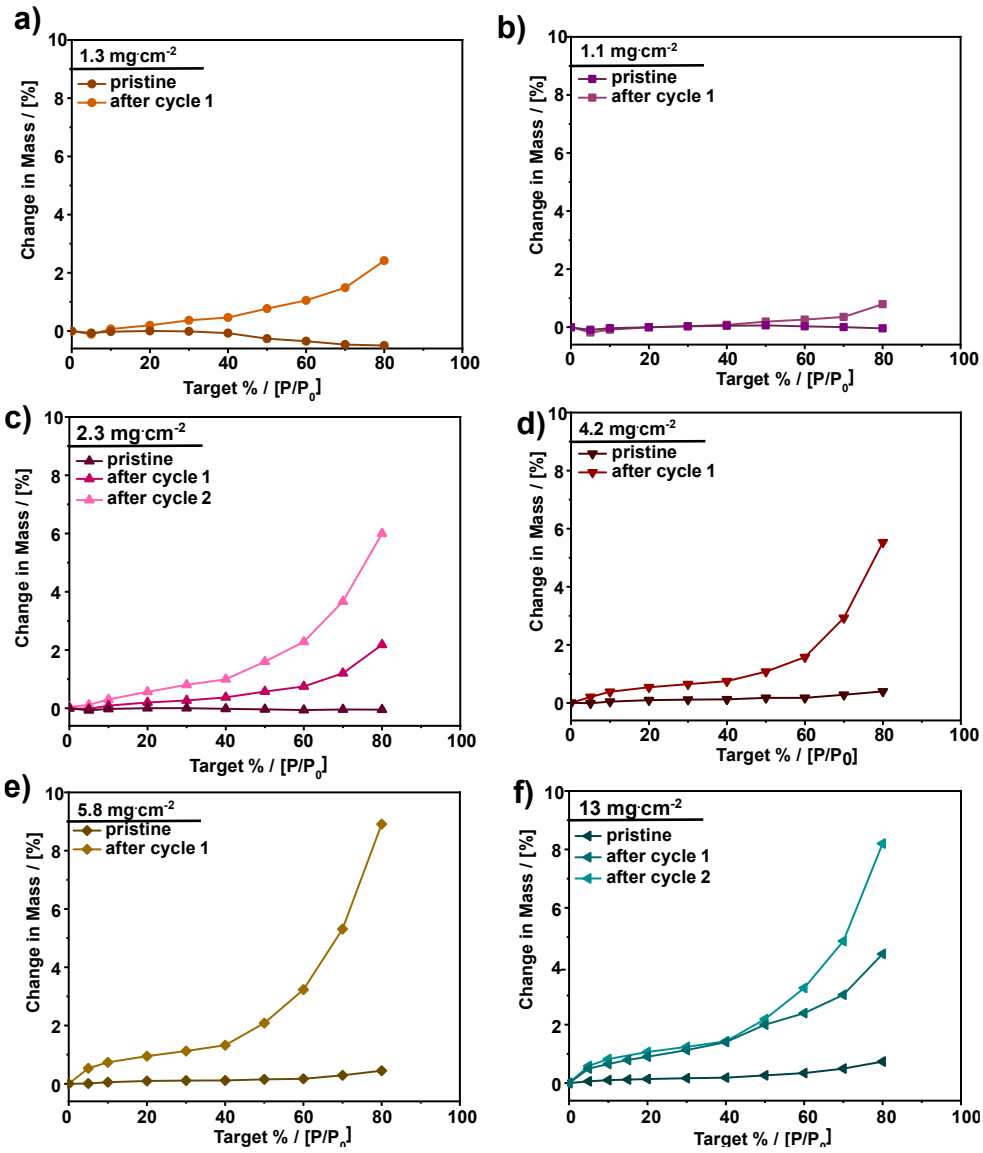


Figure 35. Vapor sorption measurements of GDEs with different catalyst loadings: a) 1.1 mg·cm^{-2} and b) 1.3 mg·cm^{-2}, c) 4.2 mg·cm^{-2} and d) 5.8 mg·cm^{-2}. Vapor adsorption isotherms of the investigated GDEs in different states – pristine and after cycle 1. Vapor sorption measurements were conducted at 25°C with a relative humidity from 0 to 80%, each humidity point was held for 60 min. Negative values are a result of the device uncertainty, common for a small amount of sample with limited adsorption. Reproduced from [2], enabled by the Creative Commons CC-BY license (https://creativecommons.org/licenses/by/4.0/).

GDE. After cycle 1, at low catalyst loadings (≤ 2.3 mg cm–2), both measurement methods reveal residual hydrophobicity, as indicated by an intermediate contact angle and relatively low water uptake (up to a 2% mass change). For higher catalyst loadings (>2.3 mg·cm^{-2}) this correlation also holds. The

contact angle results after cycle 1 suggest a very hydrophilic electrode surface, supported by mass change of up to 9% in vapor sorption measurements. The open structure of the GDL likely influences this relationship between surface wettability and internal hydrophobicity. SEM cross-section images (**Figure 32***)* reveal catalyst migration into deeper GDL layers. Along with possible Nafion loss or deterioration, these changes may alter the internal wettability.[57] Structural changes may also promote electrode flooding, as previously suggested.

TGA measurements were performed to determine the reason for the observations above and to establish whether catalyst material was also lost in conjunction with the GDE changes. In **Figure 36**, three decomposition steps can be identified for the pristine GDEs: at 400 °C, 500 °C, and 600 °C. The decomposition step at 400 °C can be allocated to the decomposition of Nafion (**Figure A 3**).[189] The further steps at 500°C and 600°C correspond to the decomposition of the GDL, starting with the decomposition of the hydrophobic treatment[190] and then the combustion of the carbon fibres. At the end, only the white SnO_2 remains, with which the determination of the total amount of catalyst on the GDE is possible. For the two catalyst loadings (2.3 $mg \cdot cm^{-2}$ & 13 $mg \cdot cm^{-2}$) 14.9 and 47.2 wt.% remain at the end, which correlates with the expected GDE composition (expected 15.7 and 50.1 wt% SnO_2, **Table 11**). In the comparison of the decomposition profiles of the GDEs in the pristine state and after cycle 2, three additional weight loss steps can be detected: at 150°C, 300°C, and 900°C. The two steps at 150°C and 900°C can be attributed to the decomposition of $KHCO_3$ and carbonate (K_2CO_3). The carbonate formation occurs due to the decomposition of $KHCO_3$.[191]

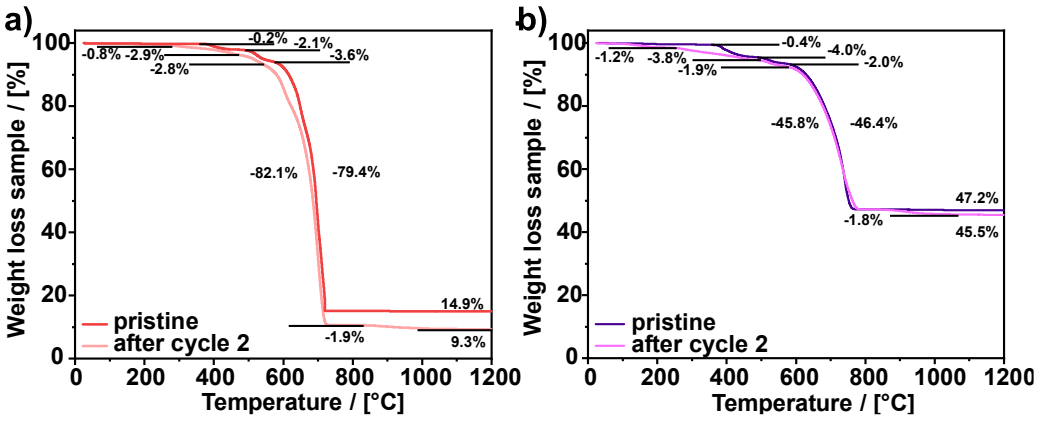


Figure 36. Thermogravimetric analysis (TGA) of the GDEs before and after electroreduction experiments at catalyst loadings of (c) 2.3 mg·cm^{-2} and (d) 13 mg·cm^{-2}. TGA was carried out from room temperature to 1200°C with a heating rate of 10 K·min^{-1} in oxygen environment. Reproduced from [2], enabled by the Creative Commons CC-BY license (https://creativecommons.org/licenses/by/4.0/).

Table 11. Result of the thermogravimetric analysis (TGA) for two gas diffusion electrodes (GDEs) with a catalyst loading of 2.3 and 13 mg·cm^{-2} before and after CO_2 electroreduction. Reproduced from [2], enabled by the Creative Commons CC-BY license (https://creativecommons.org/licenses/by/4.0/)

Relative weight	2.3 mg·cm^{-2}			13 mg·cm^{-2}		
	expected [%]	pristine [%]	used [%]	expected [%]	pristine [%]	used [%]
GDE	100	100	99.8	100	99.6	100
- Nafion	2.1	2.1	2.9	4.3	4.0	3.9
- GDL	82.2	83.0	87.3	45.6	48.4	49.2
= SnO_2	15.7	14.9	9.6	50.1	47.2	46.9

Additionally, **Figure 37** represents a magnification of **Figure 36** to allocate the decomposition steps from RT to 700°C more easily. The first prominent feature of the magnified plots is the change in weight loss steps between the pristine GDEs and after cycle 2 for the binder Nafion. While in the pristine state, the Nafion decomposition starts at 400°C, after cycle 2, there is an additional weight loss step at 300°C. This could be related to the desulfonation of sulfonic side chains of Nafion.[189] Hence, the changed weight loss step of

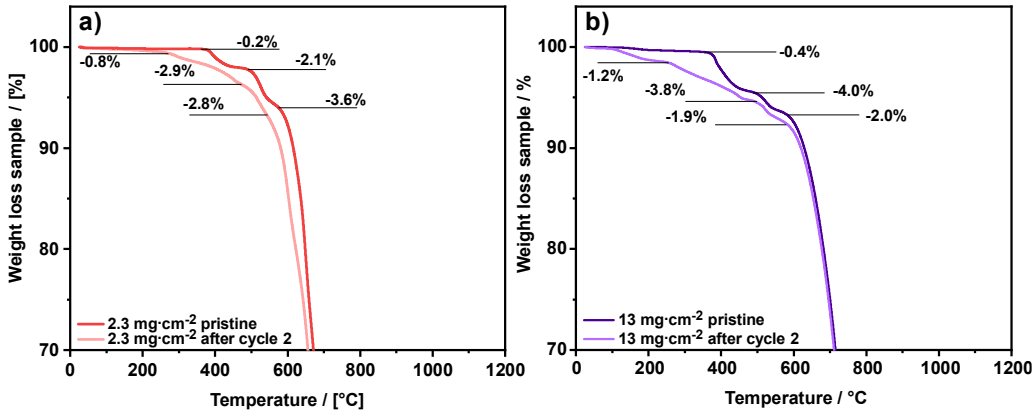


Figure 37. Thermogravimetric analysis (TGA) of the GDEs before and after electroreduction experiments at catalyst loadings of (a) 2.3 mg·cm^{-2} and (b) 13 mg·cm^{-2} in the cut out of 70 – 100wt%. TGA was carried out from room temperature to 1200°C with a heating rate of 10 K·min^{-1} in oxygen environment. Reproduced from [2], enabled by the Creative Commons CC-BY license (https://creativecommons.org/licenses/by/4.0/).

Nafion in combination with the decomposition step of the sulfonic side chains could be related to structural change within the Nafion during the electroreduction of CO_2.[121] The presented structural modifications of Nafion might be the reason for the hydrophobicity changes in the catalyst layer. For the GDL coated only with Nafion, the contact angle measurements already showed an alteration of the hydrophobicity (**Table 10**). Additionally, the vapor sorption measurements in combination with the contact angle measurements detected a loss of hydrophobicity for the GDEs after the electrochemical measurements. Moreover, the respective Raman peaks for Nafion vanished, and in addition to the less prominent decomposition step of the hydrophobic treatment of the carbon fibres, a deterioration of the GDE is suggested. This leads to the conclusion that the progressive loss of Nafion in combination with the deterioration of the hydrophobic treatment of the carbon fibres upon continued usage of the GDEs could result in GDE flooding as an electrode failure mechanism.

In addition to the discussion before, catalyst losses along with the deterioration of Nafion can be determined with the TGA results. Comparing the remaining catalyst at the end of the TGA measurements of the pristine GDE with the GDE after the electrochemical measurements, for the 2.3 mg·cm^{-2}

GDE a loss of about 30% was determined, 9.6% to 14.9%. For the 13 $mg \cdot cm^{-2}$ GDE, on the other hand, only minor or no loss of catalyst material at all was detected, with a difference of 47.2% to 46.9% between the pristine state and after the electrochemical measurements, even though the presence of catalyst agglomeration and the loss of Nafion was detected. Hence, the utilised binder in this chapter, Nafion, exhibited limited stability, which was at least partly responsible for the observed run-in effects of the investigated GDEs under the applied electrochemical conditions.

4.3 Impact of the Binder Matrix on Gas Diffusion Electrodes for CO_2 Electroreduction to Formate

A. Kretzschmar conducted the vapor sorption measurements.

The previous chapters 4.1 and 4.2 laid the groundwork for investigating a suitable GDE architecture. In particular, the study on early-stage performance changes revealed the unsuitability of Nafion as a binder. This underscores the importance of precise electrode design, as achieving optimal wettability and hydrophobicity is key to efficient and stable CO_2 electroreduction.[192] Generally, a binder in the catalyst layer and GDL serves multiple functions: it provides mechanical stability, maintains the GDE's hydrophobic nature to facilitate CO_2 mass transfer to the catalyst layer, and can prevent nanoparticle dissolution and morphological changes. Recent studies have shown that certain binders can stabilise the catalyst layer, enabling consistent electroreduction of CO_2 at relevant FEs.[193–195] This chapter highlights the influence of binder matrices in custom-made GDEs on CO_2 electroreduction to formate. Ion-conducting binders, which transport either cations (cation-conducting binders, CCB) or anions (anion-conducting binders, ACB), were selected. Specifically, Nafion and Aquivion were used as CCB, while Aemion, Sustainion, Fumion, Piperion, and Pention served as ACB. Additionally, a hybrid

binder of Aemion + Nafion was also investigated. **Table 4** and **Table 5** list the binders, their ion-conduction properties, and their structural formulas.

4.3.1 Influence of the binder on the electrode performance

Emphasising the importance of the binder choice in the electroreduction of CO_2 to formate, GDEs with eight different binders (**Table 4**) were prepared and tested upon repeated cycling at increasing cathodic current densities (36, 71 and 107 $mA \cdot cm^{-2}$). Additionally, to determine the stability of these GDEs throughout the continuous electroreduction of CO_2, LSV scans were performed prior to each electrolysis run (**Figure 38**).

Considering the influence of the binder on the obtained cathodic current density at −1.15 V_{RHE} (**Figure 38)**, the highest cathodic current densities are obtained with CCBs. This becomes especially evident in the first cycle at Run 1, where Aquivion obtains the highest cathodic current density, 243 ± 49 $mA \cdot cm^{-2}$. Sustainion as an ACB shows the lowest cathodic current density with 55 ± 11 $mA \cdot cm^{-2}$. Unfortunately, the binder Aquivion could only be tested for one cycle due to premature electrode flooding, which may be attributed to its structure itself. Aquivion has shorter PFSA chains than Nafion, resulting in a better drag of water to the catalyst layer, causing an even worse resistance against electrode flooding than Nafion.[196]

In a more detailed analysis of the cathodic current densities in cycle 1, two distinct groups can be identified. The first group is comparable to the course observed in the previous chapters. At cycle 1, Run 1, the highest cathodic current density is obtained, while at the subsequent Runs 2 and 3, the obtained cathodic current densities are in the same range but overall lower. For example, Nafion showed in cycle 1, Run 1, a cathodic current density of 165 ± 33 $mA \cdot cm^{-2}$, which decreased to 131 ± 26 $mA \cdot cm^{-2}$ for Runs 2 and 3. In the second group, the obtained cathodic current densities, however, are in the same range for all three Runs. Thereby, Aemion obtained cathodic current densities of around 128 ± 26 $mA \cdot cm^{-2}$ for all three Runs in cycle 1.

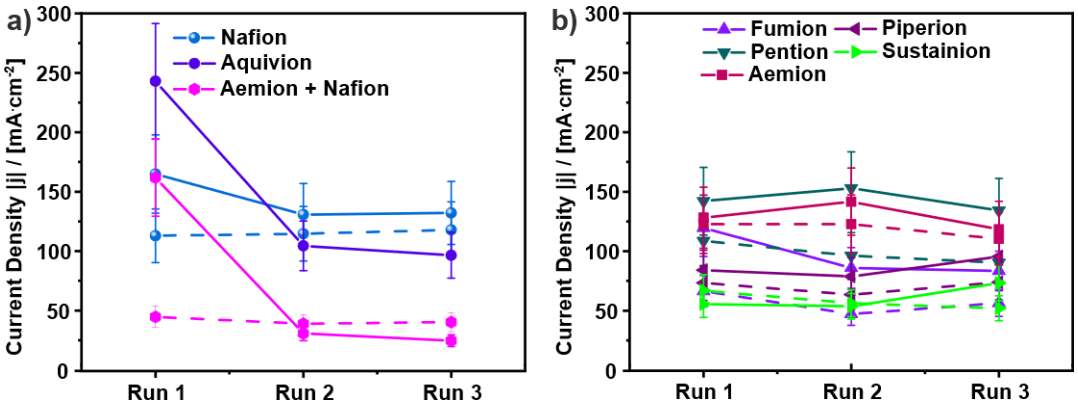


Figure 38. Evaluation of the cathodic current density at −1.15 V_{RHE} depending on the different binder types: a) cation conducting binder (CCB) and b) anion conducting binder (ACB). The bold lines represent Cycle 1, and the dashed lines Cycle 2. (Measurement conditions: batch reactor, 12 ml electrolyte, 1 M $KHCO_3$, continuous CO_2 supply of 20 ml·min^{-1}, start at room temperature, electrolysis time: 45 min each)

The division into two groups is also present for the second cycle of LSVs. In group one, a considerable decrease in current density is evident in the comparison between the first Runs of cycles 1 and 2, followed by a stable current density for the subsequent runs. Overall, a decrease in the obtained cathodic current densities of up to 80 mA·cm^{-2} is observed. For example, Piperion obtains a decrease in cathodic current density at the first runs of about 25% from 95 ± 19 mA·cm^{-2} to 73 ± 15 mA·cm^{-2}. For Runs 2 and 3, the obtained cathodic current densities are 63 ± 13 mA·cm^{-2} and 74 ± 14 mA·cm^{-2}, respectively. In the case of the second group, the obtained cathodic current densities are in the same range for both cycles. For example, Aemion obtains a cathodic current density of around 54 ± 11 mA.cm^{-2} at Run 2 for both cycles and Sustainion of around 128 ± 26 mA·cm^{-2} at Run 1 for both cycles, respectively. Thus, as the evaluation of the LSVs scans in **Figure 38** indicates, the GDE's stability and Sustainion and Aemion obtain similar current densities throughout the two cycles, and therefore they might be suitable binders for the investigated setup.

Regarding the influence of the binder on the avg. electrode potentials (**Figure 39**) upon repeated cycling at increasing cathodic current densities (36, 71, 107 $mA \cdot cm^{-2}$), again the obtained avr. electrode potentials increase with increasing applied current density. This effect is similarly observed in the previous chapters and can be explained by the increased electrode polarisation.[178–180] Overall, the obtained avr. electrode potentials range from –0.70 ± 0.06 V_{RHE} to –1.30 ± 0.06 V_{RHE}. The most positive avr. electrode potentials are obtained with Pention and Nafion in the first cycle, ranging from –0.72 ± 0.06 V_{RHE} to –0.96 ± 0.06 V_{RHE} and from –0.79 ± 0.06 V_{RHE} to –0.99 ± 0.06 V_{RHE}, respectively.

Considering the influence of repeated cycling on the avr. electrode potential, a drop of up to 30% is evident between cycle 1 and cycle 2. The highest drop occurs with the hybrid binder Aemion+Nafion at 36 $mA \cdot cm^{-2}$, from –0.79 ± 0.06 V_{RHE} to –1.11 ± 0.06 V_{RHE}, respectively. Regarding the other investigated binders, a maximum drop of about 15% V_{RHE} is observed between cycle 1 and cycle 2. For example, Aemion shows at 36 $mA \cdot cm^{-2}$ an avr. electrode potential of −0.74 ± 0.06 V_{RHE} and −0.8 ± 0.06 V_{RHE} for cycle 1 and cycle 2, respectively. Comparing the subsequently applied current densities (71 and 107 $mA \cdot cm^{-2}$), similar to the previous chapter, the obtained avr. electrode potentials remain within the same range. Aemion obtains an avr. electrode potentials for both cycles at 71 and 107 $mA \cdot cm^{-2}$

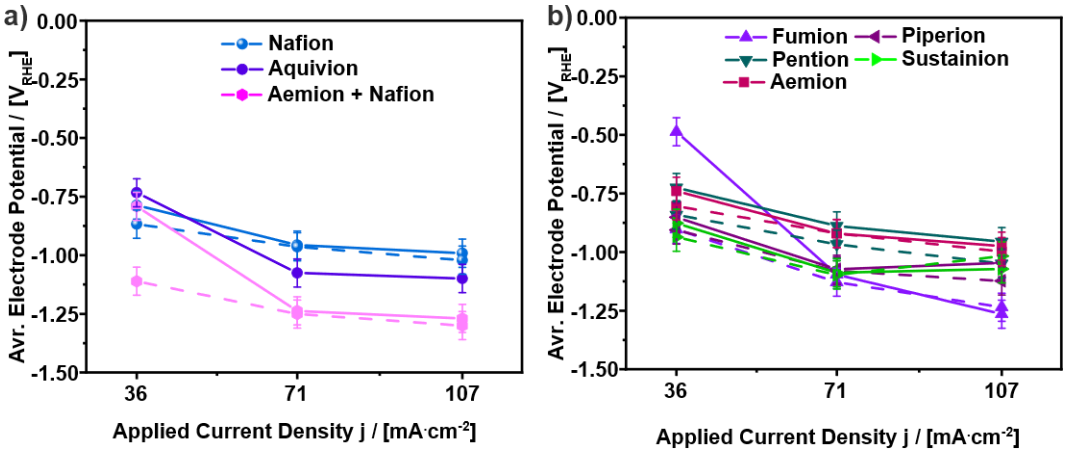


Figure 39. Evaluation of the avr. electrode potential depending on the different binder types: a) CCB and b) ACB for three current densities (36, 71 and 107 $mA \cdot cm^{-2}$). The bold lines represent Cycle 1, and the dashed lines represent Cycle 2. (Measurement conditions: batch reactor, 12 ml electrolyte, 1 M $KHCO_3$, continuous CO_2 supply of 20 $ml \cdot min^{-1}$, start at room temperature, electrolysis time: 45 min each).

of –0.92 ±0.06 V_{RHE} to –0.92 ±0.06 V_{RHE} and –0.97 ±0.06 V_{RHE} to –1.00 ± 0.06 V_{RHE}, respectively. Thus, even though the utilised binder type influenced the obtained LSV results, no clear trend is distinguishable for the avr. electrode potentials.

Figure 40 depicts the FE for formate obtained during the experiments shown in **Figure 39**. Similar to the previous chapters, the increasing applied current densities are accompanied by an increase in FE for formate due to the more favourable electrode potentials for formate evolution. Considering the influence of the binders' ionomeric character, the lowest FE for formate is generally obtained with ACBs. This effect is especially pronounced for the Aemion GDE, which obtains FEs up to 40% lower than Nafion. Aemion obtains FEs in the first cycle, from 54 ± 8% to 69 ± 10%, while Nafion obtains FEs for formate from 91 ± 9% to 104 ± 11%, respectively. A possible explanation for the low FEs obtained for formate with ACBs may be their intrinsic ion-conduction property. Anion-conducting binders effectively shuttle OH^- ions away from the catalyst surface, leaving a surplus of H^+ behind. The surplus of protons in the vicinity of the catalyst layer then most probably leads to a decreased local pH and a favoured HER, and thus a decreased FE for formate.[147] To emphasise this theory, **Figure 40** depicts the FEs for all evolved products during the CO_2 electroreduction reaction. Hereby, it is demonstrated that, for all investigated ACBs, the HER is increased compared to the results obtained with Nafion and Aquivion. Interestingly, this effect is not only present with SnO_2-based GDEs but also for Cu-based ones.[197]

Comparing the obtained FEs during the two cycles of CO_2 electroreduction, the results can be categorised into three groups. The first group exhibits an overall decline in FE between the two cycles, consistent with the findings presented in the previous chapter. This effect primarily manifests with the CCB Nafion and the hybrid Aemion + Nafion. For example, the hybrid binder Aemion+Nafion showed an increase in FE from 76 ± 11% to 89 ± 13 in the first cycle, followed by a decline of up to 40% in the second cycle. The most significant decrease in FE is

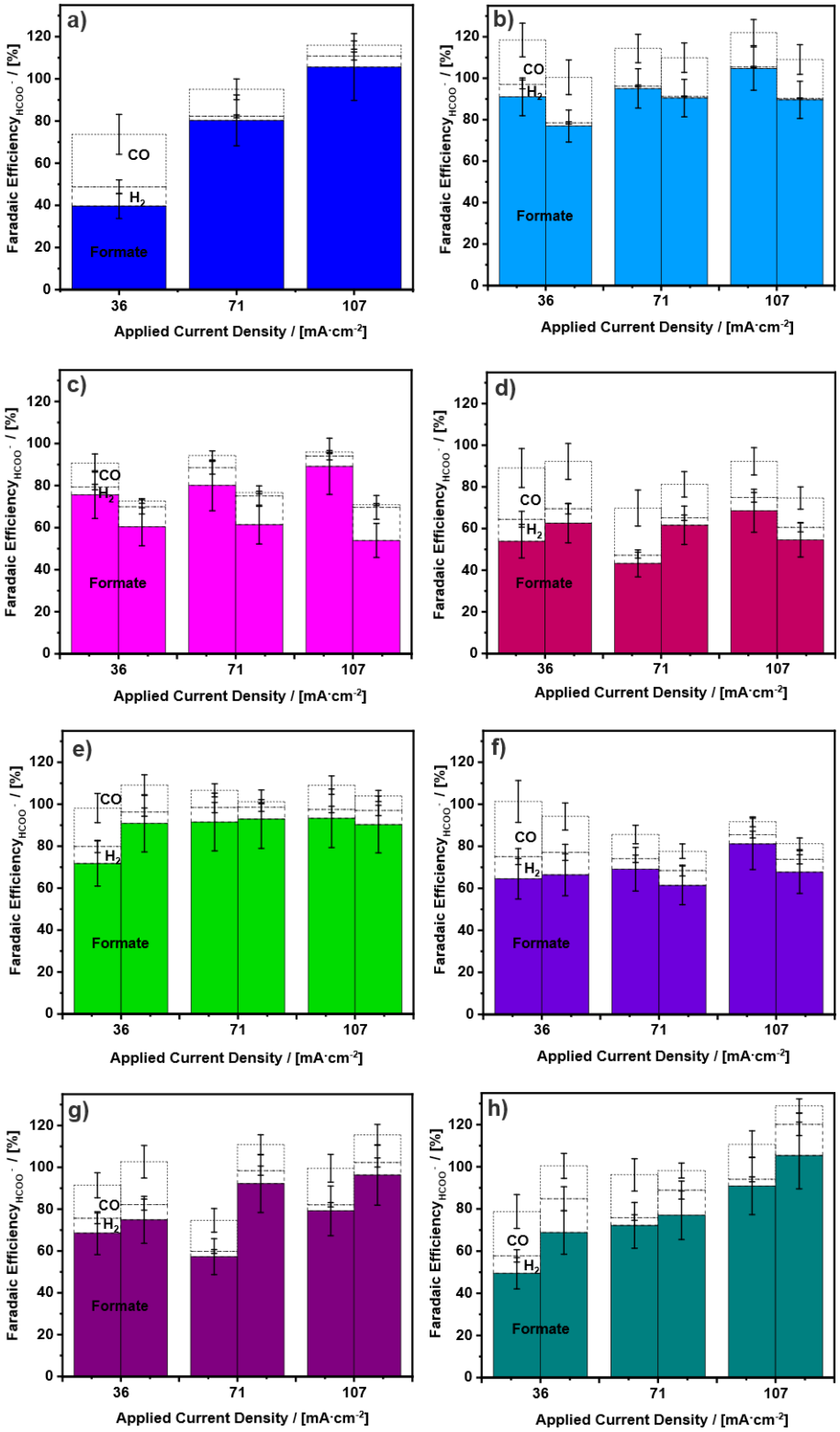


Figure 40. Faradaic efficiencies for formate, H_2 and CO at different current densities ranging from –36 to –107 mA·cm^{-2} repeated cycling. Error bars indicate the estimated standard deviation of a typical experiment. Catalyst loading: 2.3 mg·cm^{-2}, measurement conditions: batch reactor, 12 ml electrolyte, 1 M $KHCO_3$, continuous CO_2 supply of 20 ml·min^{-1}, start at room temperature, electrolysis time: 45 min each.

observed at 107 mA·cm², where FEs of 89 ± 13% and 54 ± 8% are obtained for cycles 1 and 2, respectively. However, the obtained FEs for formate in the second cycle match those obtained with Aemion as the binder.

Considering the second group, the FEs for formate show an increase with increasing electrode potential in both the first and second cycles of the electroreduction of CO_2 experiments. This is in contrast to group 1, where a decrease in FEs for formate was observed in the second cycle. The effect of the further increase in FE is mainly observed with the ACBs Piperion and Pention. For example, Piperion obtains FEs of 69 ± 10% up to 79 ± 11% in the first cycle. In the second cycle, a further increase in FE is obtained, 75 ± 11% up to 96 ± 15%. This could indicate that a running-in phase is also present, but it has not yet been fully completed.

Regarding the third group, the obtained FEs for formate are in the same range throughout both cycles. This effect is especially present with the ACBs Sustainion, Aemion and Fumion. Sustainion thereby obtains FEs above 90±14% in both cycles, while for Fumion and Aemion, the FEs for formate are around 60±10%. A possible explanation for the high FE with Sustainion as a binder may be the 20-fold higher CO_2 solubility in Sustainion compared to water, based on the CO_2 affinity of its imidazolium groups.[74,198] Thus, based on the results presented here, Sustainion appears to be a suitable exchange for Nafion as a binder. Especially, the high stability of electrode performance based on the similar obtained cathodic current densities at −1.15 V_{RHE} and the obtained FEs for formate >90% throughout both cycles indicated no decline in electrode performance in contrast to Nafion and states a particular suitability as binder. However, the post-GDE characterisation needs to be discussed first to determine if any changes in the catalyst layer occurred, which could decrease its suitability as a binder.

4.3.2 GDE Characterisation (pre- and post-test)

To elucidate the observed effects during the electrochemical measurements, the GDEs from **Figure 39** were subjected to further characterisation: scanning electron

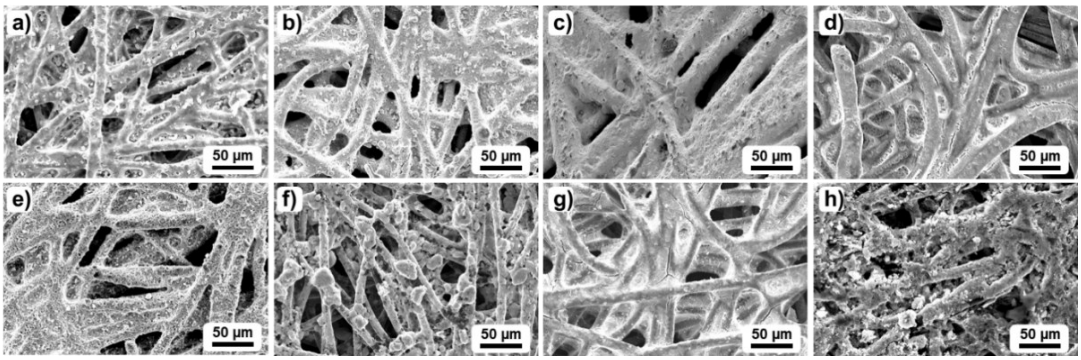


Figure 41. SEM images of the investigated GDEs in dependence of the binder in the pristine state: a) Aquivion, b) Nafion, c) Aemion+Nafion, d) Aemion, e) Sustainion, f) Fumion, g) Piperion, and h) Pention.

microscopy (SEM), Raman spectroscopy, contact angle (CA) measurements, and vapor sorption measurements. **Figure 41** shows the GDE topography of the investigated binders in the pristine state, and **Figure 42** shows the GDEs after cycle 2. Comparing the pristine GDE topographies in **Figure 41,** small agglomerates are apparent, with sizes ranging from 10 to 30 µm, due to the spray deposition process of the GDE. The small agglomerates can be seen regardless of the investigated ion-conducting ionomer.

Considering the differences between the pristine GDEs and those after the electroreduction experiments, as shown in **Figure 42**, three effects are apparent: catalyst agglomeration, smoothening of the catalyst layer, and no change in the catalyst layer. While the effect of catalyst agglomeration is only apparent with the binder Aquivion, the smoothening of the catalyst layer occurs for most of the other investigated binders. Catalyst agglomeration occurs only with binder Aquivion, as only one cycle of electrochemical measurements could be performed with this binder. As in the previous chapter, early-stage performance changes of GDEs, catalyst agglomeration, are only apparent after the first cycle of electrochemical measurements, followed by a smoothing effect of the catalyst layer after the second cycle. However, the smoothing effect of the catalyst layer only affects the binders Nafion, Aemion+Nafion, Fumion and Pention. The most significant change in the catalyst layer occurs with Fumion and Pention. In the case of Fumion, the catalyst layer changed from being covered by big agglomerates to a smooth version without agglomerates. Regarding Pention, the smoothening effect is especially

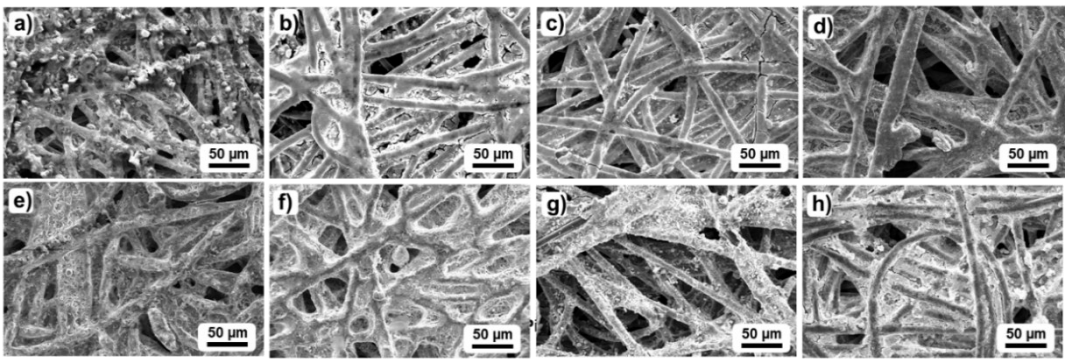


Figure 42. Exemplary SEM images of the investigated GDEs in dependence of the binder type after cycle 2. a) Aquivion (after cycle 1), b) Nafion, c) Aemion+Nafion, d) Aemion, e) Sustainion, f) Fumion, g) Piperion, and h) Pention.

accompanied by catalyst migration into the deeper layers of the carbon fibres, as shown in **Figure 32.** The catalyst migration here is so drastic that the carbon fibres become visible again, most likely explaining the increased amount of HER in cycle 2, compared to the other ACBs (**Figure 40**).

The third effect, in which no change of the catalyst layer topography is observed, is only apparent with Sustainion and Aemion as binders (**Figure 42 a** and **e**). The stable catalyst layer throughout the electrochemical measurements, as shown in the SEM images, most likely explains the stable cathodic current densities at −1.15 VRHE and the stable FEs for formate throughout both cycles.

Raman spectroscopy measurements were performed to analyse whether there was also a change in the composition of the GDEs due to CO_2 electroreduction. The corresponding results are depicted in **Figure 43** and show distinct differences between the pristine and the GDEs after CO_2 electroreduction, respectively. To obtain the Raman bands of the binder alone, either binder droplets were applied onto a glass substrate and dried, or the pure membrane was used. For the pristine GDEs, the Raman spectra are again, as in the previous chapter, governed by the response of the catalyst layer, i.e. the response of the catalyst and the binder, SnO_2 and the respective investigated binder.[2] Here, as a brief repetition, the classical Raman bands for SnO_2 are at 470 cm^{-1} (E_g), 630 cm^{-1} (A_{1g}) and 770 cm^{-1} (B_{2g}).[185] Additionally, disordered activated surface modes can also occur as broad peaks in the region from 475 to 775 cm^{-1} (S1, S2 and S3). The occurrence of these defect

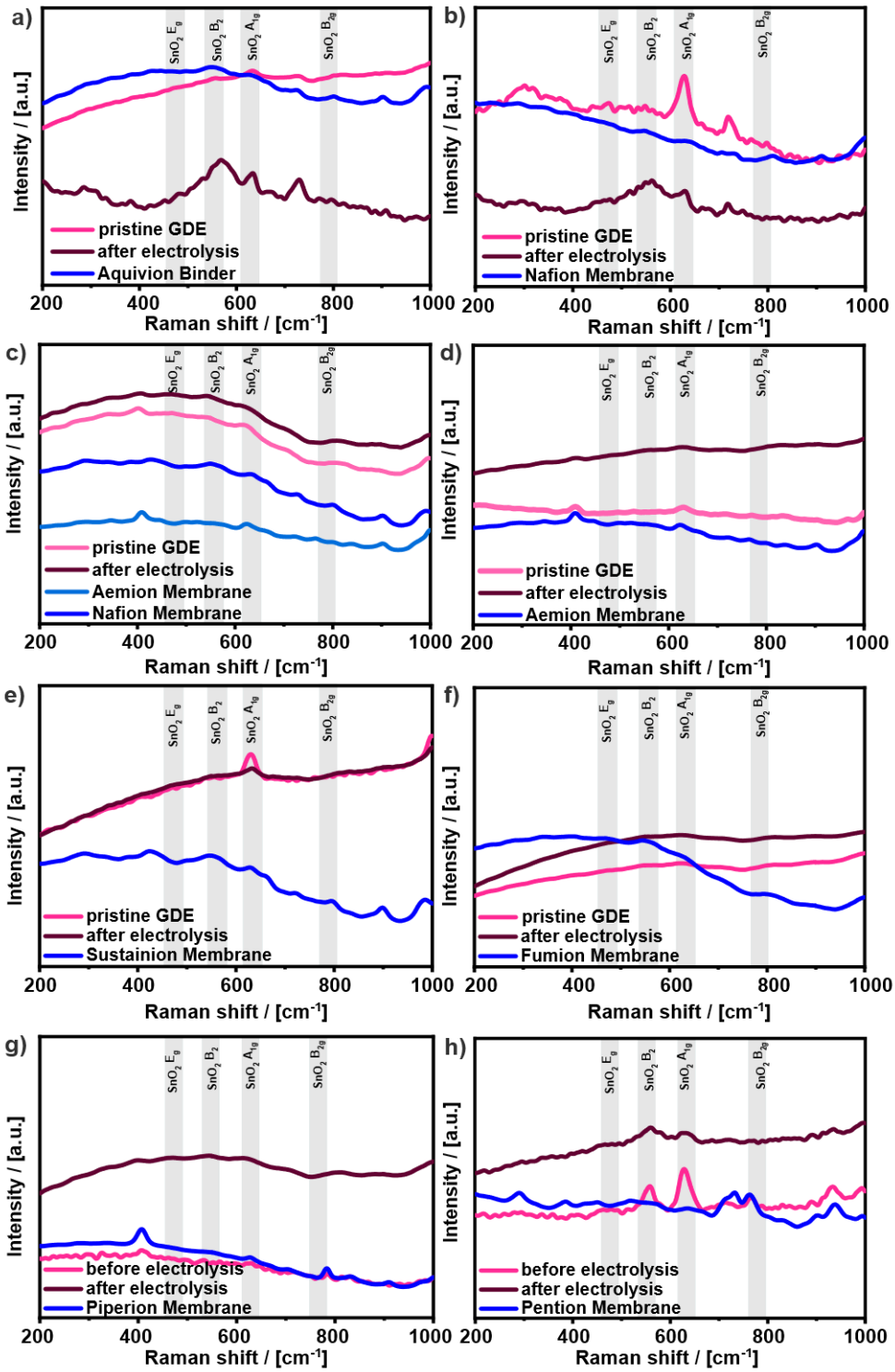


Figure 43. Raman spectra for the investigated GDEs before and after CO_2 electroreduction, as well as the respective binder used: a) Aquivion, b) Nafion, c) Aemion + Nafion, d) Aemion, e) Sustainion, f) Fumion, g) Piperion and h) Pention. (Incident wavelength: 532 nm, spectra normalised to the highest vibration).

modes depend on the nanoparticle size and can be detected at 570 cm^{-1} (S1) in the pristine state for all GDEs.[186] Besides this, the remaining bands in the Raman spectra can be attributed to the investigated binders. Nafion shows four bands at 292 cm^{-1} (A_1), 385 cm^{-1} (A_t), 731 cm^{-1} (A_1), and 971 cm^{-1}.[187] Aquivion displays the same Raman bands as Nafion, as its structure differs only in the length of the side chains. Characteristic bands of Aemion are at 406 cm^{-1}, 622 cm^{-1}, 997 cm^{-1}, and 1047 cm^{-1}.[199] For the hybrid binder Aemion+Nafion, the characteristic Raman bands are a combination of the respective used binders. Pention shows characteristic bands at 733 cm^{-1}, 764 cm^{-1}, 887 cm^{-1}, 931 cm^{-1}, 992 cm^{-1} and 1049 cm^{-1}. Piperion shows characteristic bands at 404 cm^{-1} and 833 $cm^{-1,}$ and Sustainion at 894 cm^{-1} and 983 cm^{-1}.

Comparing the Raman spectra of the pristine GDE and those after the electroreduction experiments, three notable effects are observed: the characteristic Raman bands of the binders become less pronounced, and the Raman bands for SnO_2 change or vanish almost completely. Regarding the Raman bands of the respective binders, a decrease is observable for all the GDEs after electroreduction, and no difference is apparent in terms of the ion-conducting ionomer type. However, the direct influence of the vanished Raman bands of the respective binders, especially the wettability of the GDE, contact angle measurements and vapour sorption measurements, needs to be discussed first.

The change of the SnO_2 bands, especially the Raman bands at 570 cm^{-1} and 630 cm^{-1}, is similar to the previous chapter and can most probably be ascribed to the reduction of SnO_2 to metallic Sn^0 but still prevalent $Sn^{IV}O_2$.[28] Furthermore, the broad peak arising at 570 cm^{-1} is probably a result of the formation of amorphous hydrous $Sn^{IV}O_2$ and is a further indicator for the observed morphological changes in the SEM images after cycle 2.[188] This effect can especially be seen at the GDEs coated with Aquivion, Nafion, Aemion+Nafion and Pention as binder. Furthermore, the vanishing of the characteristic SnO_2 Raman band at 630 cm^{-1} is most probably affected by a reduction from SnO_2 to Sn^0 during the electrochemical measurements.[28] In the case of the binders Sustainion and Aemion, this effect is the most pronounced, leading to an almost vanished Raman band; however, unlike the other

binders, no additional Raman band at 570 cm^{-1} evolved. The absence of the Raman band at 530 cm^{-1} would explain the topography of the catalyst layer for these two binders in **Figure 43**, as no formation of amorphous hydrous $Sn^{IV}O_2$ occurred, leading to a smooth catalyst layer. This may also explain the very stable results obtained during the electroreduction of CO_2, particularly regarding the cathodic current densities at −1.15 V vs. RHE. In addition, the decrease of FE at 107 $mA \cdot cm^{-2}$ in cycle 2 for both, Sustainion and Aemion, could be explained by the reduction of the SnO_2 peak, as the pure Sn metal is less active as a catalyst for the CO_2 electroreduction to formate than SnO_2.[28] However, it seems still sufficient active species is available for the electroreduction of CO_2 to formate as the FE for the CO_2 electroreduction products remains high (**Figure 40**).

Contact angle measurements and vapor sorption measurements were conducted to further elucidate the influence of the almost vanished Raman binder bands on the GDE's wettability. **Table 12** presents the contact angles of the investigated GDEs with different binders in their pristine state and after the electroreduction of CO_2. The pristine GDL (without a catalyst layer) shows a hydrophobic surface with a contact angle of 137.9 ± 5.0°. Comparing the pristine GDL to the pristine GDEs (with a catalyst layer), a decrease in contact angle of up to 64° is observable and can even result in a hydrophilic surface, depending on the applied binder. A hydrophilic catalyst layer at the pristine GDEs is already apparent when Fumion, Pention or Aemion are used as binders. However, with the other utilised binder types, a hydrophobic catalyst layer is present at the pristine GDE. A possible explanation for the already hydrophilic catalyst layer in the pristine state lies most probably in the higher water uptake percentages of the hydrocarbon-based ACBs compared to their fluoropolymer CCBs counterparts.[200] Additionally, similar contact angles are found in the literature for the binders Nafion, Sustainion, and Fumion, albeit with different catalyst materials. [118]

A further influencing factor on the catalyst layer's hydrophobicity is the electroreduction of CO_2 itself, which further decreases the contact angle. The highest decrease in contact angle is observed with the binders Aquivion, Aemion+Nafion and Aemion. Here, the applied droplet is immediately absorbed

and sinks into the deeper layers of the electrode. However, to draw a connection between the high wettability of the catalyst layer, i.e. absorbed droplet during the contact angle measurements, and the possibly intact bulk hydrophobicity required to sustain high electrode performance, the vapor sorption measurements need to be discussed as well.

Table 12. Investigation of the influence of the implemented binder on the contact angle of the respective GDEs before and after the electroreduction of CO_2 and GDLs coated only with the respective binders. (Scattering represents the standard deviation).

Binder	GDE (pristine) [°]	GDE (after) [°]	only Binder (w/o SnO2) [°]
0 (GDL)	137.9 ± 5.0	-	
Aquivion	137.3 ± 1.3	absorbed (after cycle 1)	132.3 ± 0.5
Nafion	126.7 ± 2.7	41.9 ± 6.5	134.3 ± 1.0
Aemion+Nafion	104.6 ± 8.9	absorbed	123.7 ± 2.7
Aemion	79.3 ± 5.8	absorbed	106 ± 10.2
Sustainion	135.8 ± 5.2	106.7 ± 1.9	134.3 ± 1.5
Fumion	90.3 ± 3.2	74.4 ± 7.7	128.3 ± 5.1
Piperion	103.2 ± 14.4	33.9 ± 5.6	113.2 ± 6.2
Pention	74.2 ± 6.2	47.5 ± 3.6	145.8 ± 2.6

Sustainion, on the other hand, opposing the contact angle results obtained for the other binders after CO_2 electroreduction, shows a sustained hydrophobicity of the catalyst layer. Sustainion shows a contact angle of 106.7 ± 1.9° and a still contact hydrophobic catalyst layer. The remaining hydrophobicity, in combination with the high CO_2 affinity of Sustainion's imidazolium groups,[198] might be the reason for the stable electrode performance in terms of the obtained stable FEs for formate >90% for both cycles. Thus, the disappearance of Raman bands in the investigated binders indicates a partial loss of hydrophobicity in the catalyst layer. However, no severe effects, such as electrode flooding, have been observed, except for Aquivion.

Vapor sorption measurements were also conducted to further discuss the GDE's bulk hydrophobicity and the influence of the vanishing Raman binder bands. **Figure 44** shows the vapour adsorption isotherms for the investigated binders at different states of the GDEs, pristine and after the electroreduction of CO_2. For all investigated samples, the pristine state of the GDE adsorbs the least amount of water, with an uptake of up to 1.5 wt%. The GDEs with the highest water uptake in the pristine state are Piperion, Fumion and Aemion, with uptakes of 1.25 wt%, 1.46 wt% and 1.36 wt% at 80% humidity, respectively. These binders are also the ones showing a hydrophilic catalyst layer at the pristine GDE contact angles. The higher water uptake for these binders may be attributed to the higher water affinity of hydrocarbon-based binders compared to their fluoropolymer counterparts.[200] Thus, based on the results of the vapor sorption measurements, a correlation can be established with the obtained contact angle results. Furthermore, the wettability of the catalyst layer, as determined by contact angle measurements, also provides a good initial indication of the overall GDE hydrophobicity.

Further elucidating the influence of the electroreduction of CO_2 on the GDE's bulk hydrophobicity, the water uptake is also determined after the electrochemical measurements. Hereby, a water uptake of up to ten times higher is observed compared to the pristine samples. The highest water uptake is exhibited with Piperion as the utilised binder, with an increase in absorbed vapour from 1.25 wt% to 12 wt% at 80% relative humidity. Aemion, as one of the binders where the applied droplet for the contact angle measurements was immediately absorbed, shows a seven times higher water uptake from 1.36 wt% to 9.85 wt%. On the other hand, the least amount of adsorbed water exhibits the GDE with Sustainion as binder, only four times higher, from 0.5 wt% to 2.3 wt% at 80% humidity. Thus, the vanished Raman binder peaks lead not only to an increased wettability of the catalyst

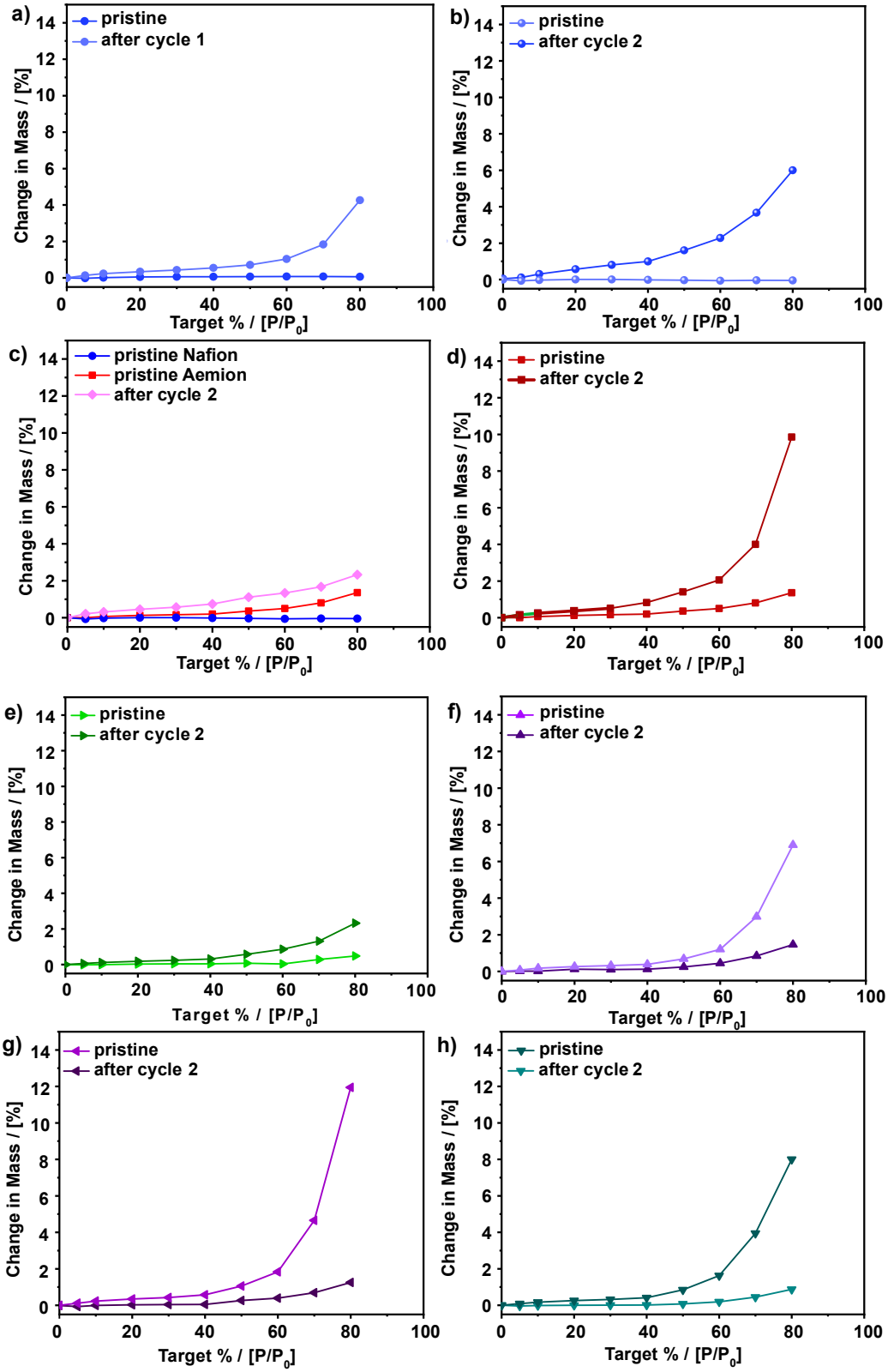


Figure 44. Vapor sorption measurements of GDEs with different binders: a) Aquivion, b) Nafion, c) Aemion+Nafion, d) Aemion, e) Sustainion, f) Fumion, g) Piperion and h) Pention. Vapor adsorption isotherms of the investigated GDEs in different states – pristine and after cycle 2.

layer but also to a decreased bulk hydrophobicity of the GDE. Even though the Raman binder peaks vanished for all investigated binders, it did not result in drastic effects, such as electrode flooding, as in the case of Aquivion. A positive effect of the higher wettability is shown in the case of the binders Piperion and Pention, where the electrolyte most probably reaches the migrated catalyst particles, resulting in the increased FE for formate in cycle 2. Based on the results presented in this chapter, it can be concluded that Sustainion is a suitable alternative to Nafion as a binder. Considering the electrode performance, which is based on stable avr. electrode potentials for both cycles, i.e. at 107 $mA \cdot cm^{-2}$ of around -1 ± 0.06 V_{RHE}, and the high FEs for formate of over 90% for both cycles of CO_2 electroreduction. Combined with the sustained hydrophobicity and the stable catalyst layer topography shown in the SEM images, Sustainion should be used for further measurements. Also, Aemion could be considered due to its stable catalyst layer, good electrode performance, with cathodic current densities of around 128 ± 26 $mA \cdot cm^{-2}$ at -1.15 V_{RHE}, and stable FEs for formate throughout both cycles. However, the overall low FE values do not reflect well on Aemion as a binder, and it needs to be enhanced before implementing it as a binder for the CO_2 electroreduction to formate.

4.4 Investigation of the influence of the cell setup: outlook for future experiments

Alongside experiments on electrode architecture and early-stage performance changes, additional experiments were conducted in a separate cell setup, the Gaskatel flow cell (ElyFlow). This change from a batch cell to a flow cell not only brought a different way of introducing the electrolyte to the system, a change from a static to a flowing electrolyte, but also increased the active electrode surface area (from 2.81 cm^2 to 10 cm^2). Furthermore, with the ElyFlow cell, the possibility of applying current densities >107 $mA \cdot cm^{-2}$ is enabled. In this chapter, the GDE architecture developed in the previous chapters (Freudenberg E20H as GDL,

2.3 mg·cm^{-2} catalyst loading, and 10 wt% of Sustainion binder) is transferred into a flow cell. The results presented in this study shall aim to encourage future research based on this thesis rather than serve as a comprehensive study.

The initial attempt to transfer the designed GDE architecture to the flow cell application was quite unsuccessful. The main issues included premature electrode flooding and FEs for Formate < 60% after the first cycle (see **Figure 45**). The premature electrode flooding was likely caused by the open GDL structure of FB-E20H, highlighting the importance of adding a MPL in the catalyst layer.[3,67,69,70] To resolve this, a 0.4 ± 0.03 mg·cm^{-2} MPL was chosen based on pre-tests in the batch cell, as higher MPL loadings either decreased FE for formate or caused catalyst layer detachment during CO_2 electroreduction (see **Figure 46**). Additionally, a simplified manufacturing process was developed based on the GDE used for benchmarking in Chapter 4.1.[3,113] HER as the main reaction at the end of cycle 1 was quite surprising, as Sustainion as a binder (see **Figure 45**) showed superior performance in the literature,[118,201] and the previous chapter (see Chapter 4.3). When exploring alternatives, previous findings on the binder matrix proved useful (see Section 4.3). Notably, Aemion, the only binder besides Sustainion, maintained an almost unchanged catalyst layer morphology, supporting mechanical stability.[62] However, the FEs for formate were significantly lower (~60%) compared to the FEs for formate achieved with Sustainion (>90%). To overcome this, a hybrid binder was developed that combines high mechanical stability with high FEs. Aemion, which offers high stability to the catalyst layer, and Nafion, yielding high FEs for formate. Initial tests

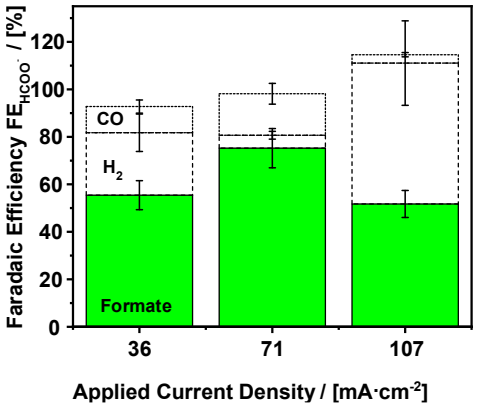


Figure 45. Flow cell measurements with Sustainion as binder: obtained FEs for Formate, H_2 and CO during the current density screening in ElyFlow setup (36 to 107 mA·cm^{-2}). Measurement conditions: GDE (2.3 mg·cm^{-2} catalyst loading, Sustainion as binder, FB-H23C3 GDL), electrolyte single-flow modus 10 ml·min^{-1}, 1 M $KHCO_3$, continuous CO_2 supply of 55 sccm (36 and 71 mA·cm^{-2}) and 85 sccm (107 mA·cm^{-2})., start at room temperature, electrolysis time: 30 min each.

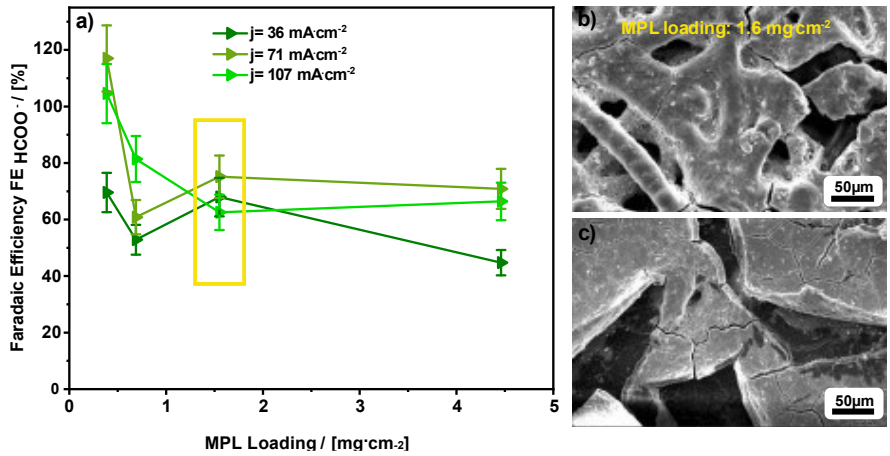


Figure 46. Influence of MPL loading on a) the obtained FE of formate. Respective SEM image of the MPL loading b) 1.6 mg.cm^{-2} before and c) after electroreduction of CO_2 showing a peeling of the catalyst layer due to too high MPL loading. Measurement conditions: batch reactor, 12 ml electrolyte, 1 M $KHCO_3$, continuous CO_2 supply of 20 ml·min^{-1}, start at room temperature, electrolysis time: 45 min each.

of this mixture in the batch cell showed FEs for formate >70% in cycle 1, proving that it is worth testing in the flow cell.

The second attempt to transfer the GDE architecture from the FlexCell to the ElyFlow, using the updated GDE design (Freudenberg E20H as GDL, 2.3 mg·cm^{-2} catalyst loading, 0.4 ± 0.03 mg·cm^{-2} MPL loading and Aemion+Nafion as the hybrid binder) was successful, as shown in **Figure 47**. To compare the results across the two setups used in this thesis, the same electrode architecture was also tested in the FlexCell (labelled as Batch Cell in **Figure 47**). For testing in both setups, the same electrochemical measurement procedure was followed (as described in section 3.3), with the CO_2 electroreduction duration shortened from 45 min to 30 min. For clarity, only the results from the CO_2 electroreduction experiments are presented in this chapter.

Initially, both cell configurations obtain similar results, as illustrated in **Figure 47 a**. The electrode potential becomes more negative with increasing current density, due to increased electrode polarisation at higher currents.[178–180] In cycle 1, the avr. electrode potentials for both cell configurations range from –0.7 ± 0.07 V_{RHE} at 36 mA·cm^{-2} to –1.18 ± 0.06 V_{RHE} at 107 mA·cm^{-2}. In cycle 2, differences appear between the two types of cells: the batch cell obtained avr. electrode

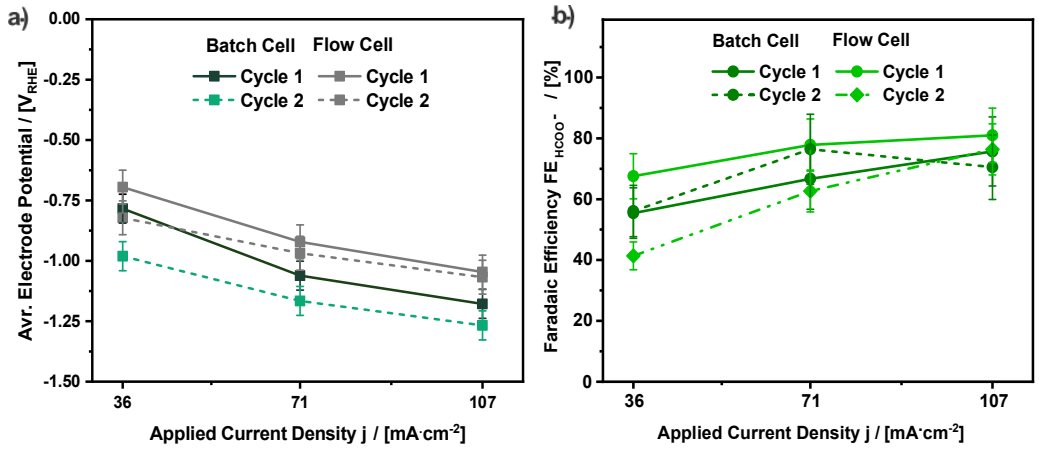


Figure 47. Influence of the repeated cycling in two different cell setups: a) Comparison of the avr. electrode potential for three different current densities (36, 71, and 107 mA·cm^{-2}) and b) FE of formate obtained after a run time of 11 min each. (Measurement conditions: batch reactor, 12 ml electrolyte, 1 M $KHCO_3$, continuous CO_2 supply of 20 ml·min^{-1}, start at room temperature, electrolysis time: 45 min each, flow cell: electrolyte in single flow modus 10 ml·min^{-1}, 1 M $KHCO_3$, continuous CO_2 supply of 300 ml·min^{-1}, start at room temperature, electrolysis time 35 min each).

potentials range from –0.98 ± 0.06 V_{RHE} to –1.27 ± 0.06 V_{RHE}, while for the flow cell, they range from –0.82 ± 0.07 V_{RHE} to –1.07 ± 0.07 V_{RHE}. Therefore, using the same GDE design and testing procedure, similar electrode potentials can be obtained regardless of the cell type.

In accordance with the obtained avr. electrode potentials, the FEs for formate shown in **Figure 47 b** are also comparable between the two cell setups. As the applied current density increases in cycle 1 (from 36 to 107 mA·cm^{-2}), the FEs for formate increase as well, from 55% ± 8.3% to 81% ± 8.9%. Overall, the obtained FEs for formate in the flow cell are higher but still within measurement variability. In cycle 2, a more noticeable difference appears between the FlexCell and ElyFlow. For the batch cell, similar FEs for formate are obtained as in cycle 1, but the flow cell shows a decrease in FE. For example, in the ElyFlow at 36 mA·cm^{-2}, the FE for formate decreases from 68 ± 7% to 41 ± 5% and at 71 mA·cm^{-2}, from 78 ± 9% to 63 ± 7%. However, at 107mA·cm^{-2}, the FE for formate is again comparable to cycle 1. Finally, employing the same electrode architecture in two distinct cell configurations with the same electrochemical measurement sequence yielded similar

results, successfully demonstrating the comparability of results in two different cell concepts using the same GDE architecture.

Further assessment of the engineered GDE architecture, whether also near-industrial relevant current densities (CD > 107 mA·cm^{-2})[107] are feasible with this GDE architecture, involved increasing the current density up to 240 mA·cm^{-2}, as shown in **Figure 48**. This resulted, as expected, in more negative avr. electrode potentials. Additionally, the FE for formate increased further up to a current density of 160 mA·cm^{-2}, illustrated in **Figure 48 b**. Therefore, the engineered GDE architecture can also be utilised for higher applied current densities.

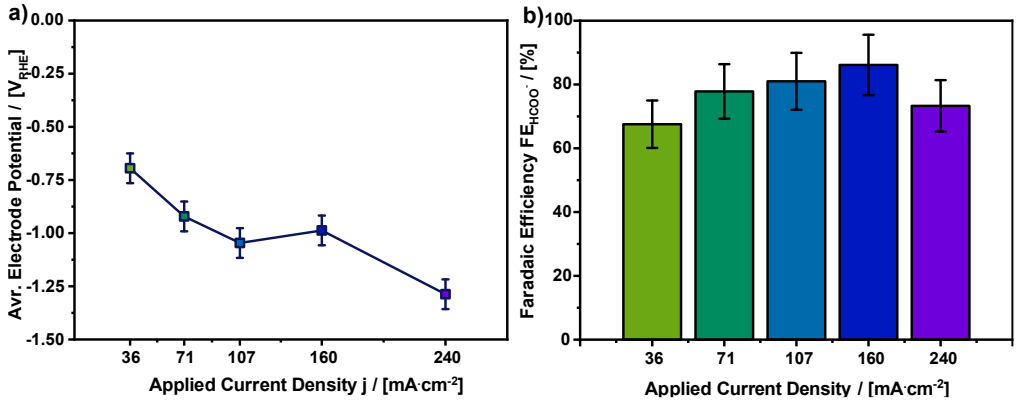


Figure 48. Current Density Screening in ElyFlow setup from 36 to 360 mA·cm^{-2}, a) avr. electrode potential and b) resulting FE.

The ultimate test for the GDE architecture's stability involved a 6-hour CO_2 electroreduction at 160 mA·cm^{-2}, as depicted in **Figure 49**. Throughout this period, the electrode potential remained stable around –1.04 ± 0.06 V_{RHE}. The slight fluctuations in electrode potential are likely due to accumulated gas bubbles on the electrode surface, which mask the active area and decrease the effective surface area between the electrolyte and electrode. This masking effect also causes an overvoltage, leading to more negative electrode potentials.[202,203] In the first 2 hours, the obtained FE for formate is approximately 75 ± 8%. Between hours 2 and 5, the electrolyte supply was briefly interrupted, preventing evaluation of the FE for formate during this period. Nevertheless, the obtained FEs for the gas products, especially H_2, remained consistent before and after the interruption, as shown in **Figure 49 b**, indicating adequate wetting of the GDE pores for CO_2 electroreduction without noticeable degradation.

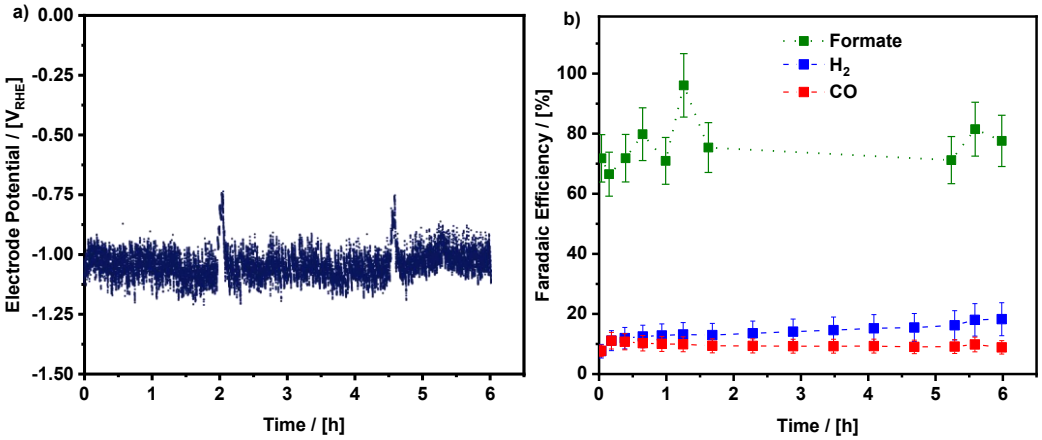


Figure 49. 6-hour electrolysis at 160 mA·cm^{-2}: a) obtained electrode potential and b) obtained FEs of formate, H_2 and CO. (Measurement conditions: flow cell: electrolyte flow 20 ml·min^{-1}, 1 M $KHCO_3$, continuous CO_2 supply of 300 ml·min^{-1}, start at room temperature, electrolysis time 6 hours).

Electrolyte samples collected for determining the FEs for formate were also used for ICP-MS measurements to evaluate the catalyst layer's mechanical stability during flow cell experiments. **Table 13** presents the results of electrolyte samples taken after 2, 16, 45, 140, and 360 min during CO_2 electroreduction. The highest catalyst loss occurs within the first few minutes, reaching a concentration of 10 µmol/L. Nonetheless, the calculated SnO_2 loss relative to the catalyst layer is ≤ 0.002%. These findings indicate a well-anchored catalyst layer with only minor losses at the beginning of electrochemical testing, thereby proving the suitability of the hybrid binder.

Table 13. Results of the ICP-MS measurements determining the amount of catalyst lost during the electroreduction of CO_2.

Time	Concentration of Sn		Amount of catalyst lost
[min]	[µmol/L]	[µg]	[%]
2	10.09	1.20	0.002
16	0.19	0.02	0.0003
45	0.08	0.01	<0.0003
140	<0.07	<0.008	<0.0003
360	<0.07	<0.008	<0.0003

To detect morphological changes of the catalyst layer depending on the cell setup and the 6-hour electrolysis, SEM images were taken, shown in **Figure 50.** Regarding the GDEs before electrochemical measurements, the topography is similar to that of the GDEs discussed in previous chapters, despite additional carbon nanoparticles being incorporated into the catalyst layer. The structure of the carbon fibres remains visible, and the spray-deposited catalyst layer fully encases the carbon fibres, forming regions with a continuous layer. Concerning the impact of the utilised cell setup, catalyst agglomerates up to 20 µm are observed for both cell types after the electrochemical testing, and the catalyst layer appears to be smoothed, as noted in earlier chapters. Additionally, a still intact catalyst layer is present, with no bare carbon fibres after repeated cycling, nor evidence of abrasion from the flowing electrolyte, consistent with the results of ICP-MS. The GDE topography after 6 hours of electrolysis showed an increase in catalyst agglomerates up to 40 µm. Furthermore, a roughening effect appears to have occurred, with small cracks forming as a result of the movement of catalyst particles. Therefore, combining Aemion and Nafion as a hybrid binder provides sufficient stability to the catalyst layer for its application in a GDE within a flow cell.

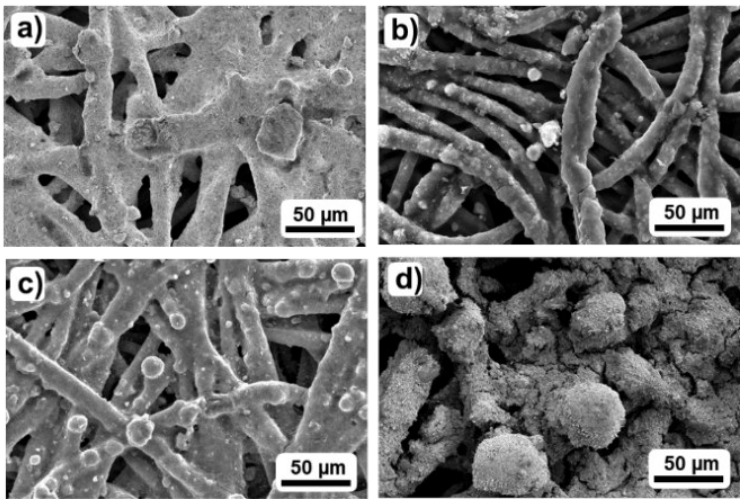


Figure 50. SEM images of the investigated GDEs: (a) pristine GDE, after repeated cycling in (b) the batch cell and (c) the flow cell, as well as d) after 6 hours of CO_2 electroreduction.

The measurements above demonstrate that transferring a GDE architecture designed in a batch cell to a flow cell can yield consistent FEs for formate and electrode potentials. Although no electrode flooding has been observed with the current GDE architecture, it still could occur during longer tests and/or at higher current densities. A potential countermeasure is switching to a GDL with a higher hydrophobic treatment, suitable for long-term measurements. Overall, these results highlight the importance of investigating the GDE interface between the catalyst, electrolyte and CO_2 to advance the electroreduction of CO_2 to formate. Especially regarding the lifetime and stability of GDEs, more research is required. Future studies should investigate GDE stability over long durations (>5000 h) at current densities > 200 $mA \cdot cm^{-2}$ in flow cell reactors. Since time and resources (CO_2, electrolyte, electricity) are limited for such long experiments, accelerated ageing techniques like accelerated stress tests and accelerated durability testing (AST/ADT), already used in the fields of fuel cells and water electrolysers, could simulate months of continuous electrolysis in less time.[204] Once the GDEs reach a certain stability, scaling up (e.g. active electrode areas of >10 cm^2) and stacking GDEs in flow electrolysers warrant further investigation.

Chapter 5
Conclusion

To conclude, the results of this dissertation can be divided into two main sections. The first section involves the influence of the GDE composition, exploring the impact of the components of a gas diffusion layer (GDL), including catalyst loading and binder type. It also considers the influence of early-stage performance changes, such as the loss of hydrophobicity and catalyst agglomeration. Finally, an outlook on the potential industrial applications of the evolved GDE architecture is provided.

Starting with the influence of the Gas Diffusion Layers (GDL) on CO_2 electroreduction, **Chapter 4.1** presented a study based on commercial GDLs that differ in the presence of MPL, GDL thickness, and the extent of hydrophobic treatment. The investigation was conducted in a gas-fed electrolysis setup with a static electrolyte specifically designed to investigate GDEs. Since the GDLs were obtained from two different manufacturers (Toray Industries, Japan, and Freudenberg GmbH, Germany), the results display different patterns. For the Toray Paper GDEs, the presence of an MPL significantly improved the cathodic current density and the Faradaic Efficiency (FE) for formate. The FE for formate was found to increase for an increasing cathodic current density of at least up to 107 $mA \cdot cm^{-2}$ and was as high as 87 ± 8.7% when using SnO_2 nanoparticles as a catalyst. Conversely, for GDEs based on Freudenberg GDLs, high through-plane conductivity outperformed the improved surface of GDLs with an MPL. Experiments with FB-E20H, a GDL without MPL, achieved high performance at low electrode potentials (below –1 ± 0.05 V_{RHE}) and reached FEs for formate of up to 100 ± 10%. Regarding the influence of hydrophobic treatment on Toray Carbon Paper GDLs, the extent of the hydrophobic treatment proved important in the absence of an MPL. The 10% PTFE treatment resulted in better GDE performance than the 30% PTFE treatment. The presence of hydrophobic treatment in Freudenberg GDEs particularly influenced FE for formate, leading to the suggestion that hydrophobic treatment could enhance

the lifetime of GDLs and delay GDE deterioration, as indicated by a decrease in FE for formate. GDL thickness, on the other hand, did not appear to be influential in the applied setup. Thus, on the one hand, if Toray Paper GDLs are used, the presence of an MPL is advantageous for maximising formate production and improving performance, such as reaching higher cathodic current densities, even beyond state-of-the-art electrodes. However, if GDLs with higher through-plane conductivity, as those for FB-E20H, are available, the performance of GDEs with an MPL can be surpassed. The superior performance of GDEs with an MPL stems from an optimal combination of a focused catalyst layer—verified by high-resolution X-ray computed tomography—as well as wetting and electrical conductivity. Furthermore, it was observed that all GDEs undergo significant changes in wetting and conductivity during initial electrochemical tests. However, these changes did not immediately reflect in the surface topography of the catalyst layer, suggesting electrochemical conversion of the catalyst and/or the (partial) displacement or deterioration of the binder. To conclude, a GDL with MPL can achieve superior performance, but GDLs with higher through-plane conductivities will always perform better. Therefore, FB-E20H was used in subsequent chapters as the GDL.

The importance of the hydrophobic treatment was particularly evident in **Chapter 4.2**, where early-stage performance changes based on the influence of the catalyst loading of the custom-made GDEs were investigated. During repeated cycling, the electrode performance, in terms of electrode potential and FEs for formate, was affected, especially by catalyst agglomeration and a decline in hydrophobicity. The most detrimental effect was the loss of hydrophobicity, which led to a decrease of FE for formate (−15%) and the disappearance of the electrode's hydrophobicity. The loss of hydrophobicity could most likely contribute to premature electrode flooding, hence affecting the lifetime of the GDE. The most plausible explanation for this observation were structural changes of the side chains and/or sulfonic groups, which states the unsuitability of Nafion as a binder in the investigated setup. However, the structural changes occurring at the GDE, the catalyst agglomeration and the binder deterioration have not yet led to a significant loss of catalyst. Moreover, the catalyst loading appeared to have a significant

influence on the GDE performance. While the increase of catalyst loading only improved the electrode performance up to a certain point, it was quite surprising that the highest catalyst loading showed a good performance in terms of FE for formate again, due to changes in the accessible active surface area. Nevertheless, the best performance was observed for a medium catalyst loading of 2.3 $mg \cdot cm^{-2}$.

Further discussing the integrity of the catalyst layer and the importance of a suitable binder, **Chapter 4.3** showed a systematic investigation of the binder matrix. The most intriguing finding here was the influence of the ionic exchange character (cationic vs. anionic) on the electrode performance regarding electrode potential and FE for formate. The cation exchange ionomers, especially, had a favourable effect on the FE for formate, with an obtained FE for formate of ≥90%. A possible explanation for the detrimental effect of the anion exchange binders in the FEs for formate could be their intrinsic anion-conducting property to anions such as OH^- and carbonate, leaving behind a surplus of H^+. The surplus of protons near the catalyst layer most probably led to a decreased local pH and a favoured HER and, thus, a decreased FE for formate. The exception from this was Sustainion. Based on the CO_2 affinity to imidazolium, FEs for formate ≥90% were obtained. In addition to the very stable catalyst layer and the least amount of water uptake in the vapor sorption measurements, Sustainion was selected as a suitable replacement for Nafion as a binder for the investigated setup. The least suitable binder, however, was Aquivion; the shorter PFSA chains, in contrast to Nafion, improved water drag to the catalyst layer, resulting in increased wettability but also premature electrode flooding. Regarding the first measurements in the flow cell, the suitability of Sustainion as a binder was inadequate. After a short time of electrolysis, HER was the favoured occurring reaction. Therefore, the hybrid binder Aemion+Nafion was ultimately selected as a replacement for Nafion.

The results presented in this dissertation demonstrate the importance of investigating GDEs to achieve technical maturity for the electroreduction of CO_2 to formate. Especially regarding the lifetime and stability of GDEs for the electroreduction of CO_2, further investigation in this direction is needed. Therefore, future

research on GDEs should focus on the stability of the GDEs in long-term measurements (>5000 h) at current densities above 200 $mA \cdot cm^{-2}$ in flow cell reactors.

Declaration of generative AI and AI-assisted technologies in the writing process

While preparing this dissertation, the author used Grammarly and DeepL to edit and enhance the readability. After using these tools, the author reviewed and edited the content as needed and takes full responsibility for the content of this dissertation.

Chapter 6 Bibliography

1. Theußl, V. *et al.* Technological Advances in the Electroreduction of CO2 to HCOOH: The Impact of Catalyst, Gas Diffusion Electrode, and Cell Design. *Electrochem. Sci. Adv.* (2024).
2. Theußl, V., Weinrich, H., Lisi, F., Tempel, H. & Eichel, R.-A. Early-Stage Performance Change of Gas Diffusion Electrodes for CO2 Electroreduction to Formate. *Sustain. Energy Fuels* (2024) doi:10.1039/d3se01347b.
3. Theußl, V. *et al.* Impact of the Carbon Substrate for Gas Diffusion Electrodes on the Electroreduction of CO2 to Formate. *ChemElectroChem* **10**, (2023).
4. Nguyen, T. T. *et al.* Security risks from climate change and environmental degradation : implications for sustainable land use transformation in the Global South. *Curr. Opin. Environ. Sustain.* **63**, 101322 (2023).
5. Glanemann, N., Willner, S. N. & Levermann, A. Paris Climate Agreement passes the cost-benefit test. *Nat. Commun.* **11**, 1–11 (2020).
6. Yoro, K. O. & Daramola, M. O. CO2 emission sources, greenhouse gases, and the global warming effect. in *Advances in Carbon Capture: Methods, Technologies and Applications* 3–28 (Elsevier Inc., 2020). doi:10.1016/B978-0-12-819657-1.00001-3.
7. Szulczewski, M. L., MacMinn, C. W., Herzog, H. J. & Juanes, R. Lifetime of carbon capture and storage as a climate-change mitigation technology. *Proc. Natl. Acad. Sci. U. S. A.* **109**, 5185–5189 (2012).
8. Ghommem, M., Hajj, M. R. & Puri, I. K. Influence of natural and anthropogenic carbon dioxide sequestration on global warming. *Ecol. Modell.* **235**–**236**, 1–7 (2012).
9. Olah, G. A., Prakash, G. K. S. & Goeppert, A. Anthropogenic chemical carbon cycle for a sustainable future. *J. Am. Chem. Soc.* **133**, 12881–12898 (2011).
10. Mertens, J. *et al.* Carbon capture and utilization: More than hiding CO2 for some time. *Joule* **7**, 442–449 (2023).
11. Zhang, J., Sewell, C. D., Huang, H. & Lin, Z. Closing the Anthropogenic Chemical Carbon Cycle toward a Sustainable Future via CO2 Valorization. *Adv. Energy Mater.* **11**, 1–38 (2021).
12. Vetter, K. M. *et al.* Stability evaluation of earth-abundant metal-based polyoxometalate electrocatalysts for oxygen evolution reaction towards industrial PEM electrolysis at high current densities. *Electrochem. Sci. Adv.* **2**, (2022).
13. Kondratenko, E. V., Mul, G., Baltrusaitis, J., Larrazábal, G. O. & Pérez-Ramírez, J. Status and perspectives of CO2 conversion into fuels and chemicals by catalytic, photocatalytic and electrocatalytic processes. *Energy Environ. Sci.* **6**, 3112–3135 (2013).
14. Hernandez-Aldave, S. & Andreoli, E. Oxygen depolarised cathode as a learning platform for CO2 gas diffusion electrodes. *Catal. Sci. Technol.* **12**, 3412–3420 (2022).
15. Kuwertz, R., Aoun, N., Turek, T. & Kunz, U. Influence of PTFE Content in Gas Diffusion Layers Used for Gas-Phase Hydrogen Chloride Electrolysis with Oxygen Depolarized Cathode. *J. Electrochem. Soc.* **163**, F988–F997 (2016).
16. Kuwertz, R. *et al.* Energy-efficient chlorine production by gas-phase HCl electrolysis with oxygen depolarized cathode. *Electrochem. commun.* **34**, 320–322 (2013).
17. Suermann, M., Bensmann, B. & Hanke-Rauschenbach, R. Degradation of Proton Exchange Membrane (PEM) Water Electrolysis Cells: Looking Beyond the Cell Voltage Increase. *J. Electrochem. Soc.* **166**, F645–F652 (2019).
18. Park, S., Lee, J. W. & Popov, B. N. A review of gas diffusion layer in PEM fuel cells: Materials and designs. *Int. J. Hydrogen Energy* **37**, 5850–5865 (2012).
19. Lapicque, F., Belhadj, M., Bonnet, C., Pauchet, J. & Thomas, Y. A critical review on gas diffusion micro and macroporous layers degradations for improved membrane fuel cell durability. *J. Power Sources* **336**, 40–53 (2016).

20. Etzold, B. J. M. *et al.* Understanding the activity transport nexus in water and CO2 electrolysis: State of the art, challenges and perspectives. *Chem. Eng. J.* **424**, 130501 (2021).
21. Hegge, F. *et al.* Three-dimensional microstructure analysis of a polymer electrolyte membrane water electrolyzer anode. *J. Power Sources* **393**, 62–66 (2018).
22. Martin, A., Trinke, P., Bensmann, B. & Hanke-Rauschenbach, R. Hydrogen Crossover in PEM Water Electrolysis at Current Densities up to 10 A cm −2 . *J. Electrochem. Soc.* **169**, 094507 (2022).
23. Nesbitt, N. T. *et al.* Liquid–Solid Boundaries Dominate Activity of CO 2 Reduction on Gas-Diffusion Electrodes. *ACS Catal.* **10**, 14093–14106 (2020).
24. Leonard, M. E. *et al.* Flooded by Success: On the role of electrode wettability in CO2 electrolyzers that generate liquid products. *Journal of The Electrochemical Society* at https://doi.org/10.26434/chemrxiv.11987541.v3 (2020).
25. Ampelli, C. *et al.* Electrode and cell design for CO2 reduction: A viewpoint. *Catal. Today* **421**, 114217 (2023).
26. Jouny, M., Luc, W. & Jiao, F. General Techno-Economic Analysis of CO2 Electrolysis Systems. *Ind. Eng. Chem. Res.* **57**, 2165–2177 (2018).
27. Royer, M. E. Réduction de l'acide carbonique en acide formique. *Compt. rend* **1870**, 731–732 (1870).
28. Dutta, A., Kuzume, A., Rahaman, M., Vesztergom, S. & Broekmann, P. Monitoring the Chemical State of Catalysts for CO2 Electroreduction: An In Operando Study. *ACS Catal.* **5**, 7498–7502 (2015).
29. Hori, Y. Electrochemical CO2 Reduction on Metal Electrodes. in *Modern Aspects of Electrochemistry vol. 42* (eds. Vayenas, C. G., White, R. E. & Gamboa-Aldeco, M. E.) 89–189 (Springer, New York, NY, 2008). doi:10.1007/978-0-387-49489-0.
30. Bagger, A., Ju, W., Varela, A. S., Strasser, P. & Rossmeisl, J. Electrochemical CO2 Reduction: A Classification Problem. *ChemPhysChem* **18**, 3266–3273 (2017).
31. Al-Tamreh, S. A. *et al.* Electroreduction of Carbon Dioxide into Formate: A Comprehensive Review. *ChemElectroChem* **8**, 3207–3220 (2021).
32. Leonzio, G., Hankin, A. & Shah, N. CO2 electrochemical reduction: A state-of-the-art review with economic and environmental analyses. *Chem. Eng. Res. Des.* **208**, 934–955 (2024).
33. Verma, S., Nwabara, U. O. & Kenis, P. J. A. Carbon-Based Electrodes and Catalysts for the Electroreduction of Carbon Dioxide (CO2) to Value-Added Chemicals. in *Nanocarbons for Energy Conversion: Supramolecular Approaches* 219–251 (2019). doi:https://doi.org/10.1007/978-3-319-92917-0_10.
34. Hietala, J. *et al.* Formic acid. in *Ullmann's Encyclopedia of Industrial Chemistry* 1–12 (2016).
35. Chen, Y. *et al.* The effect of catholyte and catalyst layer binders on CO2 electroreduction selectivity. *Chem Catal.* **2**, 400–421 (2022).
36. Thijs, B., Rongé, J. & Martens, J. A. Matching emerging formic acid synthesis processes with application requirements†. *Green Chem.* **24**, 2287–2295 (2022).
37. Pérez-Fortes, M., Schöneberger, J. C., Boulamanti, A., Harrison, G. & Tzimas, E. Formic acid synthesis using CO2 as raw material: Techno-economic and environmental evaluation and market potential. *Int. J. Hydrogen Energy* **41**, 16444–16462 (2016).
38. Rumayor, M., Dominguez-Ramos, A., Perez, P. & Irabien, A. A techno-economic evaluation approach to the electrochemical reduction of CO2 for formic acid manufacture. *J. CO2 Util.* **34**, 490–499 (2019).
39. Formic Acid Global Production. https://www.chemanalyst.com/industry-report/formic-acid-market-688.
40. Spurgeon, J. M. & Kumar, B. A comparative technoeconomic analysis of pathways for commercial electrochemical CO2 reduction to liquid products. *Energy Environ. Sci.* **11**,

1536–1551 (2018).
41. Eppinger, J. & Huang, K. W. Formic Acid as a Hydrogen Energy Carrier. *ACS Energy Lett.* **2**, 188–195 (2017).
42. Oh, W., Rhee, C. K., Han, J. W. & Shong, B. Atomic and Molecular Adsorption on the Bi(111) Surface: Insights into Catalytic CO2 Reduction. *J. Phys. Chem. C* **122**, 23084–23090 (2018).
43. Pander, J. E., Baruch, M. F. & Bocarsly, A. B. Probing the Mechanism of Aqueous CO2 Reduction on Post-Transition-Metal Electrodes using ATR-IR Spectroelectrochemistry. *ACS Catal.* **6**, 7824–7833 (2016).
44. Koh, J. H. *et al.* Facile CO2 Electro-Reduction to Formate via Oxygen Bidentate Intermediate Stabilized by High-Index Planes of Bi Dendrite Catalyst. *ACS Catal.* **7**, 5071–5077 (2017).
45. Zhang, Y., Guo, S. X., Zhang, X., Bond, A. M. & Zhang, J. Mechanistic understanding of the electrocatalytic CO2 reduction reaction – New developments based on advanced instrumental techniques. *Nano Today* **31**, 100835 (2020).
46. Baruch, M. F., Pander, J. E., White, J. L. & Bocarsly, A. B. Mechanistic Insights into the Reduction of CO2 on Tin Electrodes using in Situ ATR-IR Spectroscopy. *ACS Catal.* **5**, 3148–3156 (2015).
47. Zhang, X., Guo, S. X., Gandionco, K. A., Bond, A. M. & Zhang, J. Electrocatalytic carbon dioxide reduction: from fundamental principles to catalyst design. *Mater. Today Adv.* **7**, 100074 (2020).
48. Zhang, Q., Xu, W., Xu, J., Liu, Y. & Zhang, J. High performing and cost-effective metal/metal oxide/metal alloy catalysts/electrodes for low temperature CO2 electroreduction. *Catal. Today* **318**, 15–22 (2018).
49. Li, F., MacFarlane, D. R. & Zhang, J. Recent advances in the nanoengineering of electrocatalysts for CO2 reduction. *Nanoscale* **10**, 6235–6260 (2018).
50. Gao, D., Cai, F., Wang, G. & Bao, X. Nanostructured heterogeneous catalysts for electrochemical reduction of CO2. *Curr. Opin. Green Sustain. Chem.* **3**, 39–44 (2017).
51. Bi, W., Wu, C. & Xie, Y. Atomically Thin Two-Dimensional Solids: An Emerging Platform for CO2 Electroreduction. *ACS Energy Lett.* **3**, 624–633 (2018).
52. Van Daele, K. *et al.* Sn-Based Electrocatalyst Stability: A Crucial Piece to the Puzzle for the Electrochemical CO2Reduction toward Formic Acid. *ACS Energy Lett.* **6**, 4317–4327 (2021).
53. Yu, F. *et al.* Electrochemical CO2 reduction: From catalysts to reactive thermodynamics and kinetics. *Carbon Capture Sci. Technol.* **6**, (2023).
54. An, X. *et al.* Common strategies for improving the performances of tin and bismuth-based catalysts in the electrocatalytic reduction of CO2 to formic acid/formate. *Renew. Sustain. Energy Rev.* **143**, 110952 (2021).
55. Liang, X. Du, Tian, N., Hu, S. N., Zhou, Z. Y. & Sun, S. G. Recent advances of bismuth-based electrocatalysts for CO2 reduction: Strategies, mechanism and applications. *Mater. Reports Energy* **3**, 100191 (2023).
56. Manolova, M. *et al.* Comparison of Electrochemically Deposited Bi and Sn Catalysts onto Gas Diffusion Electrodes for the Electrochemical CO2 Reduction Reaction to Formate. *Appl. Sci.* **13**, (2023).
57. Díaz-Sainz, G., Alvarez-Guerra, M. & Irabien, A. Continuous electrochemical reduction of CO2to formate: Comparative study of the influence of the electrode configuration with sn and bi-based electrocatalysts. *Molecules* **25**, (2020).
58. Weiss, R. F. Carbon Dioxide in Water and Seawater: The solubility of a non-ideal gas. *Mar. Chem.* **2**, 203–215 (1974).
59. Burdyny, T. & Smith, W. A. CO2 reduction on gas-diffusion electrodes and why catalytic performance must be assessed at commercially-relevant conditions. *Energy Environ. Sci.* **12**, 1442–1453 (2019).

60. Yang, K., Kas, R., Smith, W. A. & Burdyny, T. Role of the Carbon-Based Gas Diffusion Layer on Flooding in a Gas Diffusion Electrode Cell for Electrochemical CO2Reduction. *ACS Energy Lett.* **6**, 33–40 (2021).
61. Samu, A. A., Szenti, I., Kukovecz, Á., Endrődi, B. & Janáky, C. Systematic screening of gas diffusion layers for high performance CO2 electrolysis. *Commun. Chem.* **6**, 1–9 (2023).
62. Martens, C., Schmid, B., Tempel, H. & Eichel, R. A. CO2 flow electrolysis - limiting impact of heat and gas evolution in the electrolyte gap on current density. *Green Chem.* **25**, 7794–7806 (2023).
63. Hussain, N., Van Steen, E., Tanaka, S. & Levecque, P. Metal based gas diffusion layers for enhanced fuel cell performance at high current densities. *J. Power Sources* **337**, 18–24 (2017).
64. Dinh, C. T. *et al.* CO2 electroreduction to ethylene via hydroxide-mediated copper catalysis at an abrupt interface. *Science (80-.).* **360**, 783–787 (2018).
65. Rutjens, B. *et al.* Impact of the PiperION Anion Exchange Membrane Thickness on the Performance of a CO2-to-HCOOH Three-Compartment Electrolyzer. (2024) doi:10.1021/acs.iecr.3c04459.
66. Philips, M. F., Gruter, G.-J. M., Koper, M. T. M. & Schouten, K. J. P. Optimizing the Electrochemical Reduction of CO 2 to Formate: A State-of-the-Art Analysis. *ACS Sustain. Chem. Eng.* **8**, 15430–15444 (2020).
67. Kim, B., Hillman, F., Ariyoshi, M., Fujikawa, S. & Kenis, P. J. A. Effects of composition of the micro porous layer and the substrate on performance in the electrochemical reduction of CO2 to CO. *J. Power Sources* **312**, 192–198 (2016).
68. Park, G. G. *et al.* Effect of PTFE contents in the gas diffusion media on the performance of PEMFC. *J. Power Sources* **131**, 182–187 (2004).
69. Weber, A. Z. & Newman, J. Effects of Microporous Layers in Polymer Electrolyte Fuel Cells. *J. Electrochem. Soc.* **152**, A677 (2005).
70. Wu, Y. *et al.* Effects of microporous layer on electrolyte flooding in gas diffusion electrodes and selectivity of CO2 electrolysis to CO. *J. Power Sources* **522**, 230998 (2022).
71. Wu, Y. *et al.* Mitigating Electrolyte Flooding for Electrochemical CO2 Reduction via Infiltration of Hydrophobic Particles in a Gas Diffusion Layer. *ACS Energy Lett.* **7**, 2884–2892 (2022).
72. Weng, L. C., Bell, A. T. & Weber, A. Z. Modeling gas-diffusion electrodes for CO2 reduction. *Phys. Chem. Chem. Phys.* **20**, 16973–16984 (2018).
73. Löwe, A. *et al.* Optimizing Reaction Conditions and Gas Diffusion Electrodes Applied in the CO2Reduction Reaction to Formate to Reach Current Densities up to 1.8 A cm-2. *ACS Sustain. Chem. Eng.* **9**, 4213–4223 (2021).
74. Bui, J. C. *et al.* Engineering Catalyst-Electrolyte Microenvironments to Optimize the Activity and Selectivity for the Electrochemical Reduction of CO2on Cu and Ag. *Acc. Chem. Res.* **55**, 484–494 (2022).
75. Lee, J. H. *et al.* Understanding the Role of Functional Groups in Polymeric Binder for Electrochemical Carbon Dioxide Reduction on Gold Nanoparticles. *Adv. Funct. Mater.* **28**, 1–6 (2018).
76. Ozden, A. *et al.* High-rate and efficient ethylene electrosynthesis using a catalyst/promoter/transport layer. *ACS Energy Lett.* **5**, 2811–2818 (2020).
77. Salvatore, D. A. *et al.* Designing anion exchange membranes for CO2 electrolysers. *Nature Energy* vol. 6 339–348 at https://doi.org/10.1038/s41560-020-00761-x (2021).
78. Ueki, T. & Watanabe, M. Macromolecules in ionic liquids: Progress, challenges, and opportunities. *Macromolecules* vol. 41 3739–3749 at https://doi.org/10.1021/ma800171k (2008).
79. Ogawa, T., Kamiguchi, K., Tamaki, T., Imai, H. & Yamaguchi, T. Differentiating Grotthuss proton conduction mechanisms by nuclear magnetic resonance spectroscopic analysis of frozen samples. *Anal. Chem.* **86**, 9362–9366 (2014).

80. Pyoungho Choi, Nikhil H. Jalani, Tony M. Thampan, R. D. Consideration of thermodynamic, transport, and mechanical properties in the design of polymer electrolyte membranes for higher temperature fuel cell operation. 2183–2200 (2006) doi:10.1002/polb.20858.
81. Jhong, H. R. Q., Brushett, F. R. & Kenis, P. J. A. The effects of catalyst layer deposition methodology on electrode performance. *Adv. Energy Mater.* **3**, 589–599 (2013).
82. Rabiee, H. *et al.* Gas diffusion electrodes (GDEs) for electrochemical reduction of carbon dioxide, carbon monoxide, and dinitrogen to value-added products: A review. *Energy Environ. Sci.* **14**, 1959–2008 (2021).
83. Koraishy, B. M., Meyers, J. P. & Wood, K. L. Manufacturing of Direct Methanol Fuel Cell Electrodes by Spraying. *J. Electrochem. Soc.* **158**, B1459 (2011).
84. Bezerra, C. A. G., Deiner, L. J. & Tremiliosi-Filho, G. Inkjet Printed Double-Layered Cathodes for PEM Fuel Cells. *J. Electrochem. Soc.* **167**, 124503 (2020).
85. Wang, W., Chen, S., Li, J. & Wang, W. Fabrication of catalyst coated membrane with screen printing method in a proton exchange membrane fuel cell. *Int. J. Hydrogen Energy* **40**, 4649–4658 (2015).
86. Flegler, A., Hartmann, S., Settelein, J., Mandel, K. & Sextl, G. Screen printed bifunctional gas diffusion electrodes for aqueous metal-air batteries: Combining the best of the catalyst and binder world. *Electrochim. Acta* **258**, 495–503 (2017).
87. Liu, P., Yang, D., Li, B., Zhang, C. & Ming, P. Recent progress of catalyst ink for roll-to-roll manufacturing paired with slot die coating for proton exchange membrane fuel cells. *Int. J. Hydrogen Energy* **48**, 19666–19685 (2023).
88. Bevers, D., Wagner, N. & Von Bradke, M. Innovative production procedure for low cost PEFC electrodes and electrode/membrane structures. *Int. J. Hydrogen Energy* **23**, 57–63 (1998).
89. MacHunda, R. L., Lee, J. & Lee, J. Microstructural surface changes of electrodeposited Pb on gas diffusion electrode during electroreduction of gas-phase CO2. *Surf. Interface Anal.* **42**, 564–567 (2010).
90. Irtem, E. *et al.* Low-energy formate production from CO2 electroreduction using electrodeposited tin on GDE. *J. Mater. Chem. A* **4**, 13582–13588 (2016).
91. Bohlen, B., Wastl, D., Radomski, J., Sieber, V. & Vieira, L. Electrochemical CO2 reduction to formate on indium catalysts prepared by electrodeposition in deep eutectic solvents. *Electrochem. commun.* **110**, 106597 (2020).
92. Lenef, J. D. *et al.* Atomic Layer Deposition of Cu Electrocatalysts on Gas Diffusion Electrodes for CO2 Reduction. *Nano Lett.* **23**, 10779–10787 (2023).
93. Hrbek, T. *et al.* Sputter-etching treatment of proton-exchange membranes: Completely dry thin-film approach to low-loading catalyst-coated membranes for water electrolysis. *Int. J. Hydrogen Energy* **45**, 20776–20786 (2020).
94. Huq, F. *et al.* Influence of the PTFE Membrane Thickness on the CO2 Electroreduction Performance of Sputtered Cu-PTFE Gas Diffusion Electrodes. *ChemElectroChem* **9**, 1–9 (2022).
95. Bienen, F. *et al.* Degradation study on tin- and bismuth-based gas-diffusion electrodes during electrochemical CO2 reduction in highly alkaline media. *J. Energy Chem.* **62**, 367–376 (2021).
96. Kopljar, D., Inan, A., Vindayer, P., Wagner, N. & Klemm, E. Electrochemical reduction of CO2 to formate at high current density using gas diffusion electrodes. *J. Appl. Electrochem.* **44**, 1107–1116 (2014).
97. Junge Puring, K. *et al.* Electrochemical CO2 Reduction: Tailoring Catalyst Layers in Gas Diffusion Electrodes. *Adv. Sustain. Syst.* **5**, 1–13 (2021).
98. Sievers, G. W., Jensen, A. W., Brüser, V., Arenz, M. & Escudero-Escribano, M. Sputtered Platinum Thin-films for Oxygen Reduction in Gas Diffusion Electrodes: A Model System for Studies under Realistic Reaction Conditions. *Surfaces* **2**, 336–348 (2019).

99. Roschger, M. *et al.* Influence of the Electrode Deposition Method of Graphene-Based Catalyst Inks for ADEFC on Performance. *ACS Appl. Mater. Interfaces* **15**, 40687–40699 (2023).
100. Zheng, T. *et al.* Large-Scale and Highly Selective CO 2 Electrocatalytic Reduction on Nickel Single-Atom Catalyst. *Joule* **3**, 265–278 (2019).
101. Ahadi, M., Tam, M., Stumper, J. & Bahrami, M. Electronic conductivity of catalyst layers of polymer electrolyte membrane fuel cells: Through-plane vs. in-plane. *Int. J. Hydrogen Energy* **44**, 3603–3614 (2019).
102. Zhao, J., Li, X. & Liu, Z. sheng. The effect of ink dilution and evaporation on the microstructures of catalyst layers in polymer electrolyte membrane fuel cells. *Int. J. Energy Res.* **43**, 6799–6811 (2019).
103. Alcaide, F. *et al.* Effect of the solvent in the catalyst ink preparation on the properties and performance of unsupported PtRu catalyst layers in direct methanol fuel cells. *Electrochim. Acta* **231**, 529–538 (2017).
104. Bonifácio, R. N., Paschoal, J. O. A., Linardi, M. & Cuenca, R. Catalyst layer optimization by surface tension control during ink formulation of membrane electrode assemblies in proton exchange membrane fuel cell. *J. Power Sources* **196**, 4680–4685 (2011).
105. Li, M. *et al.* The role of electrode wettability in electrochemical reduction of carbon dioxide. *J. Mater. Chem. A* 1–41 (2021) doi:10.1007/978-3-319-19375-5_2.
106. Hansen, K. U. & Jiao, F. Hydrophobicity of CO2 gas diffusion electrodes. *Joule* **5**, 754–757 (2021).
107. Hernandez-Aldave, S. & Andreoli, E. Fundamentals of Gas Diffusion Electrodes and Electrolysers for Carbon Dioxide Utilisation: Challenges and Opportunities. *Catalysts* **10**, 713 (2020).
108. Dinh, C. T., García De Arquer, F. P., Sinton, D. & Sargent, E. H. High rate, selective, and stable electroreduction of co2 to co in basic and neutral media. *ACS Energy Lett.* **3**, 2835–2840 (2018).
109. Senocrate, A. *et al.* Importance of Substrate Pore Size and Wetting Behavior in Gas Diffusion Electrodes for CO2Reduction. *ACS Appl. Energy Mater.* **5**, 14504–14512 (2022).
110. Jännsch, Y., Hämmerle, M., Simon, E., Fleischer, M. & Moos, R. Contributions of Pulsed Operation Along with Proper Choice of the Substrate for Stabilizing the Catalyst Performance in Electrochemical Reduction of CO2 Toward Ethylene in Gas Diffusion Electrode Based Flow Cell Reactors. *Energy Technol.* **10**, (2022).
111. Kutz, R. B. *et al.* Sustainion Imidazolium-Functionalized Polymers for Carbon Dioxide Electrolysis. *Energy Technol.* **5**, 929–936 (2017).
112. Haas, T., Krause, R., Weber, R., Demler, M. & Schmid, G. Technical photosynthesis involving CO2 electrolysis and fermentation. *Nat. Catal.* **1**, 32–39 (2018).
113. Yang, H., Kaczur, J. J., Sajjad, S. D. & Masel, R. I. Electrochemical conversion of CO2 to formic acid utilizing Sustainion™ membranes. *J. CO2 Util.* **20**, 208–217 (2017).
114. Ma, S. *et al.* One-step electrosynthesis of ethylene and ethanol from CO2 in an alkaline electrolyzer. *J. Power Sources* **301**, 219–228 (2016).
115. Kong, Y. *et al.* Cracks as Efficient Tools to Mitigate Flooding in Gas Diffusion Electrodes Used for the Electrochemical Reduction of Carbon Dioxide. *Small Methods* **6**, (2022).
116. Kalde, A. M. *et al.* Micromodel of a Gas Diffusion Electrode Tracks In-Operando Pore-Scale Wetting Phenomena. *Small* **18**, 2204012 (2022).
117. Brosch, S., Wiesner, F., Decker, A., Linkhorst, J. & Wessling, M. Spatio-Temporal Electrowetting and Reaction Monitoring in Microfluidic Gas Diffusion Electrode Elucidates Mass Transport Limitations. *Small* (2024) doi:10.1002/smll.202310427.
118. Nwabara, U. O. *et al.* Binder-Focused Approaches to Improve the Stability of Cathodes for CO2Electroreduction. *ACS Appl. Energy Mater.* **4**, 5175–5186 (2021).
119. Moss, A. B. *et al.* In operando investigations of oscillatory water and carbonate effects in MEA-based CO2 electrolysis devices. *Joule* **7**, 350–365 (2023).

120. Cofell, E. R., Nwabara, U. O., Bhargava, S. S., Henckel, D. E. & Kenis, P. J. A. Investigation of Electrolyte-Dependent Carbonate Formation on Gas Diffusion Electrodes for CO2Electrolysis. *ACS Appl. Mater. Interfaces* **13**, 15132–15142 (2021).
121. Nwabara, U. O., Cofell, E. R., Verma, S., Negro, E. & Kenis, P. J. A. Durable Cathodes and Electrolyzers for the Efficient Aqueous Electrochemical Reduction of CO2. *ChemSusChem* **13**, 855–875 (2020).
122. Mom, R. V. *et al.* Assessment of the Degradation Mechanisms of Cu Electrodes during the CO2 Reduction Reaction. *ACS Appl. Mater. Interfaces* **15**, 30052–30059 (2023).
123. Franzen, D. *et al.* Influence of binder content in silver-based gas diffusion electrodes on pore system and electrochemical performance. *J. Appl. Electrochem.* **49**, 705–713 (2019).
124. Liu, M. *et al.* The role of ionomers in the electrolyte management of zero-gap MEA-based CO2 electrolysers: A Fumion vs. Nafion comparison. *Appl. Catal. B Environ.* **335**, (2023).
125. Leonard, M. E., Clarke, L. E., Forner-Cuenca, A., Brown, S. M. & Brushett, F. R. Investigating Electrode Flooding in a Flowing Electrolyte, Gas-Fed Carbon Dioxide Electrolyzer. *ChemSusChem* **13**, 400–411 (2020).
126. Van Daele, S. *et al.* How flue gas impurities affect the electrochemical reduction of CO2 to CO and formate. *Appl. Catal. B Environ.* **341**, 123345 (2024).
127. Cui, Z., Marx, M. A., Tegomoh, M. N. & Co, A. C. A Guide to Evaluate Electrolyte Purity for CO2 Reduction Studies. *ACS Energy Lett.* **8**, 5201–5205 (2023).
128. Pimlott, D. J. D., Jewlal, A., Mowbray, B. A. W. & Berlinguette, C. P. Impurity-Resistant CO2 Reduction Using Reactive Carbon Solutions. *ACS Energy Lett.* **8**, 1779–1784 (2023).
129. Harmon, N. J. & Wang, H. Electrochemical CO 2 Reduction in the Presence of Impurities: Influences and Mitigation Strategies . *Angew. Chemie* **134**, (2022).
130. Ikemiya, N., Natsui, K., Nakata, K. & Einaga, Y. Long-Term Continuous Conversion of CO2 to Formic Acid Using Boron-Doped Diamond Electrodes. *ACS Sustain. Chem. Eng.* **6**, 8108–8112 (2018).
131. Zhou, F., Li, H., Fournier, M. & MacFarlane, D. R. Electrocatalytic CO2 Reduction to Formate at Low Overpotentials on Electrodeposited Pd Films: Stabilized Performance by Suppression of CO Formation. *ChemSusChem* **10**, 1509–1516 (2017).
132. Popović, S. *et al.* Stability and Degradation Mechanisms of Copper-Based Catalysts for Electrochemical CO2 Reduction. *Angew. Chemie - Int. Ed.* **59**, 14736–14746 (2020).
133. Galeano, C. *et al.* Toward highly stable electrocatalysts via nanoparticle pore confinement. *J. Am. Chem. Soc.* **134**, 20457–20465 (2012).
134. Li, Y. *et al.* Structure-Sensitive CO2 Electroreduction to Hydrocarbons on Ultrathin 5-fold Twinned Copper Nanowires. *Nano Lett.* **17**, 1312–1317 (2017).
135. Chen, Q. *et al.* Elucidating key mechanistic processes during acidic CO2 electroreduction on gas diffusion electrodes towards stable production of formic acid. *Chem. Eng. J.* **476**, (2023).
136. Garg, S. *et al.* Advances and challenges in electrochemical CO2 reduction processes: An engineering and design perspective looking beyond new catalyst materials. *J. Mater. Chem. A* **8**, 1511–1544 (2020).
137. Ewis, D. *et al.* Electrochemical reduction of CO2 into formate/formic acid: A review of cell design and operation. *Sep. Purif. Technol.* **316**, 123811 (2023).
138. Gaskatel GmbH. *Test Cell FlexCell Manual*. https://gaskatel.de/shop/elektrochemische-messzelle-betriebsbereit-flexcell-ptfe/ (2023).
139. Bienen, F. *et al.* Importance of Time-Dependent Wetting Behavior of Gas-Diffusion Electrodes for Reactivity Determination. *Chemie-Ingenieur-Technik* **93**, 1015–1019 (2021).
140. Wijaya, G. H. A., Im, K. S. & Nam, S. Y. Advancements in Commercial Anion Exchange Membranes: A Review of Membrane Properties in Water Electrolysis Applications. *Desalin. Water Treat.* **320**, 100605 (2024).
141. Kuhnert, E., Hacker, V. & Bodner, M. A Review of Accelerated Stress Tests for Enhancing MEA Durability in PEM Water Electrolysis Cells. *Int. J. Energy Res.* **2023**, (2023).

142. Mo, S. *et al. Recent Advances on PEM Fuel Cells: From Key Materials to Membrane Electrode Assembly*. *Electrochemical Energy Reviews* vol. 6 (Springer Nature Singapore, 2023).
143. Yang, H., Kaczur, J. J., Sajjad, S. D. & Masel, R. I. Performance and long-term stability of CO2conversion to formic acid using a three-compartment electrolyzer design. *J. CO2 Util.* **42**, 101349 (2020).
144. O'Brien, C. P. *et al.* CO2 Electrolyzers. *Chem. Rev.* **124**, 3648–3693 (2024).
145. Nankya, R., Elgazzar, A., Zhu, P., Chen, F. Y. & Wang, H. Catalyst design and reactor engineering for electrochemical CO2 reduction to formate and formic acid. *Mater. Today* **76**, 94–109 (2024).
146. Sajna, M. S. *et al.* Electrochemical system design for CO2 conversion: A comprehensive review. *J. Environ. Chem. Eng.* **11**, 110467 (2023).
147. Chae, Y., Kim, H., Lee, D. K., Lee, U. & Won, D. H. Exploring the critical role of binders in electrochemical CO2 reduction reactions. *Nano Energy* **130**, 110134 (2024).
148. Gaskatel GmbH. *Test Cell ElyFlow Manual*. https://gaskatel.de/shop/elektrochemische-messzelle-elyflow-betriebsbereit-ptfe/ (2024).
149. Schatz, M., Jovanovic, S., Eichel, R. A. & Granwehr, J. Quantifying local pH changes in carbonate electrolyte during copper-catalysed CO 2 electroreduction using in operando 13C NMR. *Sci. Rep.* **12**, 1–9 (2022).
150. Higgins, D., Hahn, C., Xiang, C., Jaramillo, T. F. & Weber, A. Z. Gas-Diffusion Electrodes for Carbon Dioxide Reduction: A New Paradigm. *ACS Energy Lett.* **4**, 317–324 (2019).
151. Liu, K., Smith, W. A. & Burdyny, T. Introductory Guide to Assembling and Operating Gas Diffusion Electrodes for Electrochemical CO 2 Reduction. *ACS Energy Lett.* **4**, 639–643 (2019).
152. Lees, E. W., Mowbray, B. A. W., Parlane, F. G. L. & Berlinguette, C. P. Gas diffusion electrodes and membranes for CO2 reduction electrolysers. *Nat. Rev. Mater.* **7**, 55–64 (2022).
153. Díaz-Sainz, G. *et al.* CO2 electroreduction to formate: Continuous single-pass operation in a filter-press reactor at high current densities using Bi gas diffusion electrodes. *J. CO2 Util.* **34**, 12–19 (2019).
154. Kopljar, D., Wagner, N. & Klemm, E. Transferring Electrochemical CO2 Reduction from Semi-Batch into Continuous Operation Mode Using Gas Diffusion Electrodes. *Chem. Eng. Technol.* **39**, 2042–2050 (2016).
155. Del Castillo, A. *et al.* Sn nanoparticles on gas diffusion electrodes: Synthesis, characterization and use for continuous CO2 electroreduction to formate. *J. CO2 Util.* **18**, 222–228 (2017).
156. De Mot, B., Hereijgers, J., Duarte, M. & Breugelmans, T. Influence of flow and pressure distribution inside a gas diffusion electrode on the performance of a flow-by CO2 electrolyzer. *Chem. Eng. J.* **378**, 1–8 (2019).
157. Sen, S., Brown, S. M., Leonard, M. L. & Brushett, F. R. Electroreduction of carbon dioxide to formate at high current densities using tin and tin oxide gas diffusion electrodes. *J. Appl. Electrochem.* **49**, 917–928 (2019).
158. Baumgartner, L. M., Koopman, C. I., Forner-Cuenca, A. & Vermaas, D. A. Narrow Pressure Stability Window of Gas Diffusion Electrodes Limits the Scale-Up of CO 2 Electrolyzers . *ACS Sustain. Chem. Eng.* **10**, 4683–4693 (2022).
159. Martínez-Rodriguez, M. J., Tong, C., Shimpalee, S. & Van Zee, J. W. Characterization of Microporous Layer in Carbon Paper GDL for PEM Fuel Cell. *ECS Meet. Abstr.* **MA2010-02**, 927–927 (2010).
160. Young, A. P., Stumper, J., Knights, S. & Gyenge, E. Ionomer Degradation in Polymer Electrolyte Membrane Fuel Cells. *J. Electrochem. Soc.* **157**, B425 (2010).
161. Pan, Y., Wang, H. & Brandon, N. P. Gas diffusion layer degradation in proton exchange membrane fuel cells: Mechanisms, characterization techniques and modelling

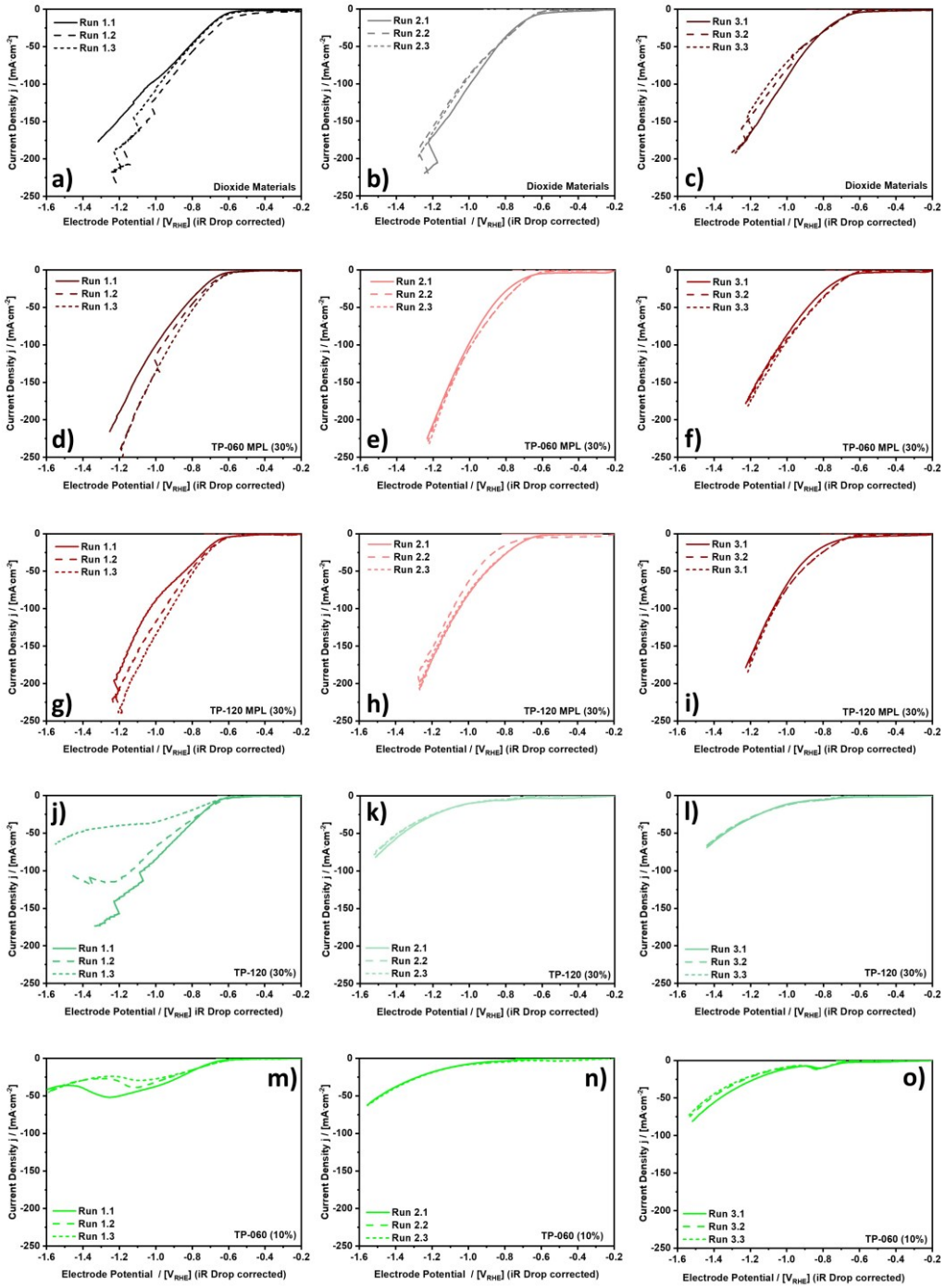
approaches. *J. Power Sources* **513**, 1–77 (2021).
162. König, M., Vaes, J., Klemm, E. & Pant, D. Solvents and Supporting Electrolytes in the Electrocatalytic Reduction of CO2. *iScience* **19**, 135–160 (2019).
163. Bumroongsakulsawat, P. & Kelsall, G. H. Effect of solution pH on CO: Formate formation rates during electrochemical reduction of aqueous CO2 at Sn cathodes. *Electrochim. Acta* **141**, 216–225 (2014).
164. Easton, E. B. & Pickup, P. G. An electrochemical impedance spectroscopy study of fuel cell electrodes. *Electrochim. Acta* **50**, 2469–2474 (2005).
165. Zhang, D. & Nagayama, G. Effective Wetting Area Based on Electrochemical Impedance Analysis: Hydrophilic Structured Surface. *Langmuir* **35**, 16508–16513 (2019).
166. Schmitt, N., Schmidt, M., Hübner, G. & Etzold, B. J. M. Oxygen reduction reaction measurements on platinum electrocatalysts in gas diffusion electrode half-cells: Influence of electrode preparation, measurement protocols and common pitfalls. *J. Power Sources* **539**, 231530 (2022).
167. Wang, Q. *et al.* Sn nanoparticles deposited onto a gas diffusion layer via impregnation-electroreduction for enhanced CO2 electroreduction to formate. *Electrochim. Acta* **369**, 137662 (2021).
168. Wen, G. *et al.* Orbital Interactions in Bi-Sn Bimetallic Electrocatalysts for Highly Selective Electrochemical CO2 Reduction toward Formate Production. *Adv. Energy Mater.* **8**, (2018).
169. Omrani, R. Gas diffusion layer for proton exchange membrane fuel cells. in *PEM Fuel Cells* (ed. Kaur, G.) 91–122 (Elsevier, Amsterdam, 2022). doi:10.1016/B978-0-12-823708-3.00017-1.
170. El-Kharouf, A., Mason, T. J., Brett, D. J. L. & Pollet, B. G. . Ex-situ characterisation of gas diffusion layers for proton exchange membrane fuel cells. *J. Power Sources* **218**, 393–404 (2012).
171. Lin, G. & Nguyen, T. Van. Effect of Thickness and Hydrophobic Polymer Content of the Gas Diffusion Layer on Electrode Flooding Level in a PEMFC. *J. Electrochem. Soc.* **152**, A1942 (2005).
172. Abarca, J. A. *et al.* Optimized manufacturing of gas diffusion electrodes for CO2 electroreduction with automatic spray pyrolysis. *J. Environ. Chem. Eng.* **11**, 109724 (2023).
173. Baumgartner, L. M., Koopman, C. I., Forner-Cuenca, A. & Vermaas, D. A. When Flooding Is Not Catastrophic–Woven Gas Diffusion Electrodes Enable Stable CO2Electrolysis. *ACS Appl. Energy Mater.* **5**, 15125–15135 (2022).
174. Sadeghifar, H. In-plane and through-plane electrical conductivities and contact resistances of a Mercedes-Benz catalyst-coated membrane, gas diffusion and micro-porous layers and a Ballard graphite bipolar plate: Impact of humidity, compressive load and polytetrafluoroe. *Energy Convers. Manag.* **154**, 191–202 (2017).
175. Castillo, A. Del *et al.* Electrocatalytic reduction of CO 2 to formate using particulate Sn electrodes : Effect of metal loading and particle size • Electrochemical characterizaϴon to find opϴmal load and size of Sn parϴcles • Filter-press cell parϴculate electrode tests • High c. *Appl. Energy* **157**, 165–173 (2015).
176. Merino-Garcia, I., Albo, J. & Irabien, A. Tailoring gas-phase CO 2 electroreduction selectivity to hydrocarbons at Cu nanoparticles. *Nanotechnology* **29**, 014001 (2018).
177. Leonard, M. E. *et al.* Editors' Choice—Flooded by Success: On the Role of Electrode Wettability in CO 2 Electrolyzers that Generate Liquid Products . *J. Electrochem. Soc.* **167**, 124521 (2020).
178. Li, F., Chen, L., Knowles, G. P., MacFarlane, D. R. & Zhang, J. Hierarchical Mesoporous SnO2Nanosheets on Carbon Cloth: A Robust and Flexible Electrocatalyst for CO2Reduction with High Efficiency and Selectivity. *Angew. Chemie - Int. Ed.* **56**, 505–509 (2017).

179. Wei, Y., Liu, J., Cheng, F. & Chen, J. Mn-doped atomic SnO2 layers for highly efficient CO2 electrochemical reduction. *J. Mater. Chem. A* **7**, 19651–19656 (2019).
180. Xiang, H. *et al.* Production of formate by CO2 electrochemical reduction and its application in energy storage. *Sustain. Energy Fuels* **4**, 277–284 (2019).
181. Möller, T. *et al.* The product selectivity zones in gas diffusion electrodes during the electrocatalytic reduction of CO2. *Energy Environ. Sci.* **14**, 5995–6006 (2021).
182. Del Castillo, A. *et al.* Electrocatalytic reduction of CO2 to formate using particulate Sn electrodes: Effect of metal loading and particle size. *Appl. Energy* **157**, 165–173 (2015).
183. Li, J. *et al.* Two-Dimensional SnO 2 Nanosheets for Efficient Carbon Dioxide Electroreduction to Formate . *ACS Sustain. Chem. Eng.* **8**, 4975–4982 (2020).
184. Hwang, D. S., Park, C. H., Yi, S. C. & Lee, Y. M. Optimal catalyst layer structure of polymer electrolyte membrane fuel cell. *Int. J. Hydrogen Energy* **36**, 9876–9885 (2011).
185. Diéguez, A., Romano-Rodríguez, A., Vilà, A. & Morante, J. R. The complete Raman spectrum of nanometric SnO2 particles. *J. Appl. Phys.* **90**, 1550–1557 (2001).
186. Weinrich, H. *et al.* CO2 Electroreduction to Formate—Comparative Study Regarding the Electrocatalytic Performance of SnO2 Nanoparticles. *Catalysts* **13**, 17 (2023).
187. Bribes, J. -L, El Boukari, M. & Maillols, J. Application of Raman spectroscopy to industrial membranes. Part 2–Perfluorosulphonic membrane. *J. Raman Spectrosc.* **22**, 275–279 (1991).
188. Ristić, M., Ivanda, M., Popović, S. & Musić, S. Dependence of nanocrystalline SnO2 particle size on synthesis route. *J. Non. Cryst. Solids* **303**, 270–280 (2002).
189. De Almeida, S. H. & Kawano, Y. Thermal behavior of Nafion membranes. *J. Therm. Anal. Calorim.* **58**, 569–577 (1999).
190. Henri, V., Dantras, E., Lacabanne, C., Dieudonne, A. & Koliatene, F. Thermal ageing of PTFE in the melted state: Influence of interdiffusion on the physicochemical structure. *Polym. Degrad. Stab.* **171**, 109053 (2020).
191. Hartman, M., Svoboda, K., Čech, B., Pohořelý, M. & Šyc, M. Decomposition of Potassium Hydrogen Carbonate: Thermochemistry, Kinetics, and Textural Changes in Solids. *Ind. Eng. Chem. Res.* **58**, 2868–2881 (2019).
192. Kim, Y. E. *et al.* Role of Binder in Cu2O Gas Diffusion Electrodes for CO2 Reduction to C2+ Products. *ACS Sustain. Chem. Eng.* **10**, 11710–11718 (2022).
193. Zhang, L. *et al.* A Polymer Solution To Prevent Nanoclustering and Improve the Selectivity of Metal Nanoparticles for Electrocatalytic CO2 Reduction. *Angew. Chemie - Int. Ed.* **58**, 15834–15840 (2019).
194. An, P. *et al.* Enhancing CO2reduction by suppressing hydrogen evolution with polytetrafluoroethylene protected copper nanoneedles. *J. Mater. Chem. A* **8**, 15936–15941 (2020).
195. Sharma, S. K., Johannessen, B., Golovko, V. B. & Marshall, A. T. Electrochemical CO 2 Reduction on Au Cluster-based Electrodes: Investigating the Role of Nafion Ionomer . *J. Electrochem. Soc.* **170**, 076509 (2023).
196. Kim, B. & Park, J. Effect of Blended Perfluorinated Sulfonic Acid Ionomer Binder on the Performance of Catalyst Layers in Polymer Electrolyte Membrane Fuel Cells. (2023).
197. Shao, T. *et al.* Tackling the proton limit under industrial electrochemical CO2 reduction by a local proton shuttle. *Carbon Energy* **6**, 1–11 (2023).
198. Sadeghpour, M., Yusoff, R. & Aroua, M. K. Polymeric ionic liquids (PILs) for CO2 capture. *Rev. Chem. Eng.* **33**, 183–200 (2017).
199. Shanahan, B., Britton, B., Belletti, A., Vierrath, S. & Breitwieser, M. Performance and stability comparison of Aemion^{TM} and Aemion+^{TM} membranes for vanadium redox flow batteries. *RSC Adv.* **11**, 13077–13084 (2021).
200. Zheng, Y. *et al.* Water Uptake Study of Anion Exchange Membranes. *Macromolecules* **51**, 3264–3278 (2018).
201. Díaz-Sainz, G. *et al.* Coupling continuous CO2electroreduction to formate with efficient

Ni-based anodes. *J. Environ. Chem. Eng.* **11**, (2023).
202. Krause, K. *et al.* Electrolyte layer gas triggers cathode potential instability in CO2 electrolyzers. *J. Power Sources* **520**, 230879 (2022).
203. Ryu, J. & Lee, D. W. Tailoring hydrophilic and hydrophobic microenvironments for gas-liquid-solid triphase electrochemical reactions. *J. Mater. Chem. A* **12**, 10012–10043 (2024).
204. Nwabara, U. O. *et al.* Towards accelerated durability testing protocols for CO2electrolysis. *J. Mater. Chem. A* **8**, 22557–22571 (2020).

This page is intentionally left blank.

Appendix



Continued

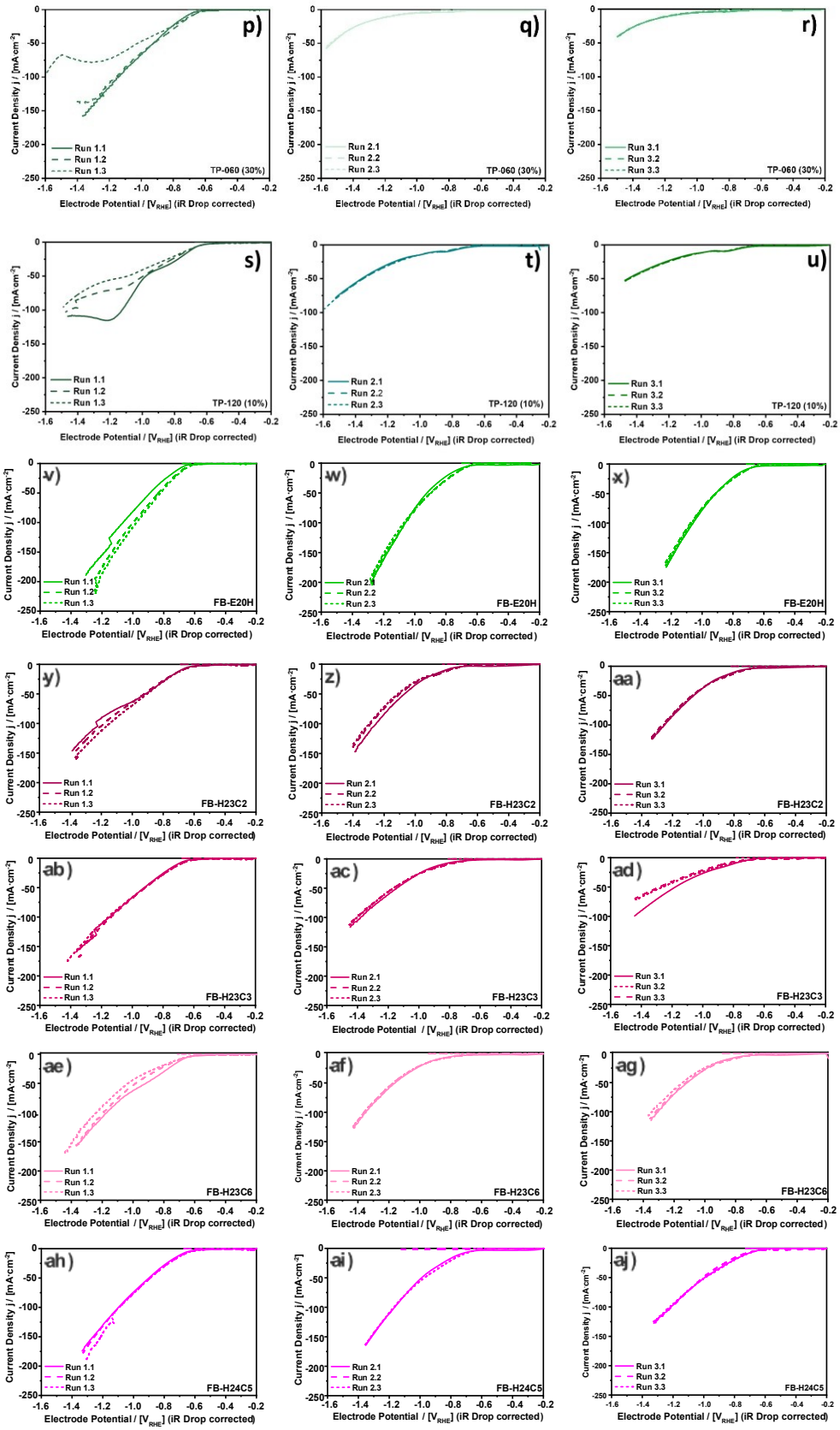


Figure A 1: All LSV-scans for the investigated GDEs. Partly reproduced from [3], enabled by the Creative Commons CC-BY license (https://creativecommons.org/licenses/by/4.0/).

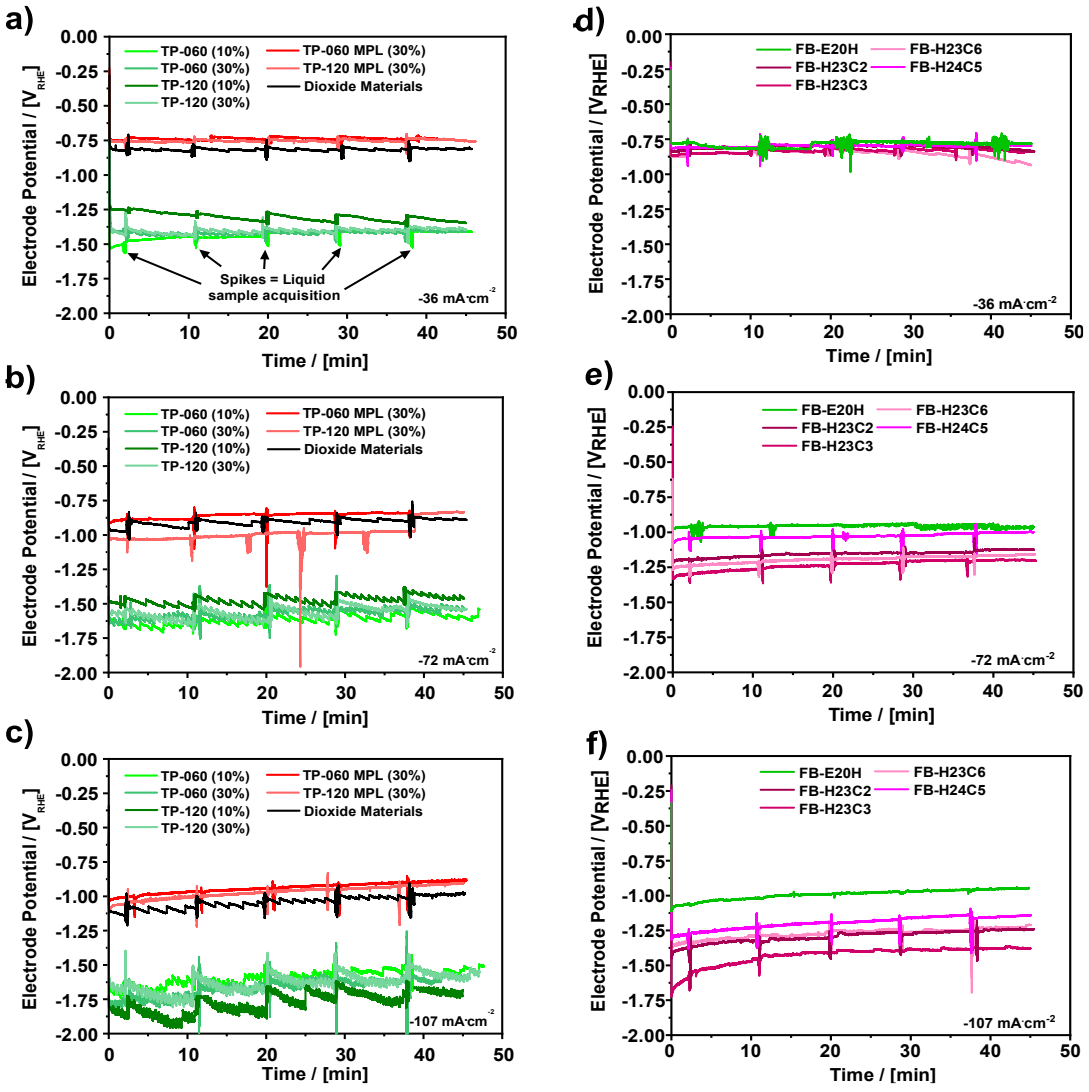


Figure A 2. Potential vs. Time curves during each 45 min CO_2-electrolysis run at current densities ranging from –36 to –107 mA·cm^{-2}, a)-c) Toray Carbon Paper GDLs and d)-f) Freudenberg GDLs. Partly reproduced from [3], enabled by the Creative Commons CC-BY license (https://creativecommons.org/licenses/by/4.0/).

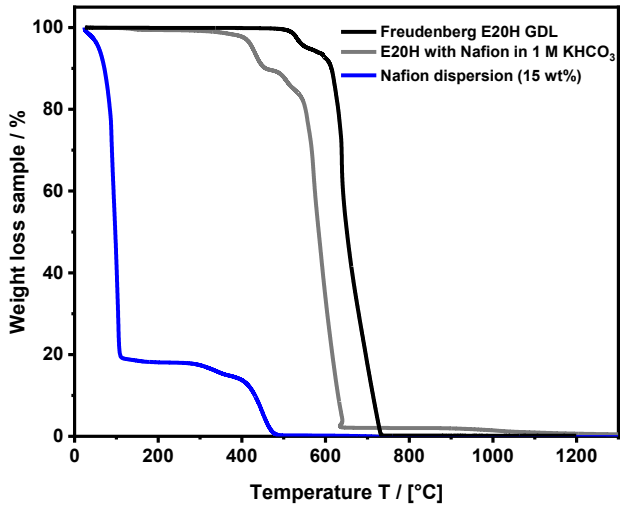


Figure A 3. Thermogravimetric analysis of pure Nafion polymer dispersion (15 wt%), the Freudenberg E20H GDL and the Freudenberg E20H GDL coated with Nafion and immersed in $KHCO_3$ for 7 days. TGA was carried out from room temperature to 1200°C with a heating rate of 10 $K \cdot min^{-1}$, in oxygen environment. Reproduced from [2], enabled by the Creative Commons CC-BY license (https://creativecommons.org/licenses/by/4.0/).

Copyrights of Figures and Tables

Table S 1. Figures and tables used in this thesis and the respective copyright requirement. In cases where copyright needs to be clarified, clearance has been granted via the Copyright Clearance Centre and the licence ID is provided. The full licence agreement can be provided on request. All other images are personally created and have been published, are to be published or are original images for this work.

Figure	Copyright clearance (Order licence ID)	From own publications ([1–3])	Original for this work
1	5785270535498	-	-
2	CCBY license-open access	-	-
3	5791821389244	-	-
4	CCBY license-open access	[3]	-
5	CCBY license-open access	[1]	-
6	5870670930573	-	-
7	CCBY license-open access	[1]	-
8 a	1563369-1.	-	-
8 b-d	CCBY license-open access	[1]	-
9	with permission from the manufacturer	-	-
10	CCBY license-open access	[3]	-
11	CCBY license-open access	[3]	-
12	with permission from the manufacturer	-	-
13	CCBY license-open access	[2]	-
14	CCBY license-open access	[3]	-
15	CCBY license-open access	-	※
16	CCBY license-open access	[3]	-
17	CCBY license-open access	[3]	-
18	CCBY license-open access	[3]	-
19	CCBY license-open access	[3]	-
20	CCBY license-open access	[3]	-

21	CCBY license-open access	[3]	-
22	CCBY license-open access	[3]	-
23	CCBY license-open access	[3]	-
24	CCBY license-open access	[2]	-
25	CCBY license-open access	[2]	-
26	CCBY license-open access	[2]	-
27	CCBY license-open access	[2]	-
28	CCBY license-open access	[2]	-
29	CCBY license-open access	[2]	-
30	CCBY license-open access-	[2]	-
31	CCBY license-open access	[2]	-
32	CCBY license-open access	[2]	-
33	CCBY license-open access	[2]	-
34	CCBY license-open access	[2]	-
35	CCBY license-open access	[2]	-
36	CCBY license-open access	[2]	-
37	CCBY license-open access	[2]	-
38	-	[-]	※
39	-	[-]	※
40	-	[-]	※
41	-	[-]	※
42	-		※
43	-	-	※
44	-	-	※
45	-	-	※
46	-	-	※
47	-	-	※
48	-	-	※
49	-	-	※
50	-	[-]	※
A1	CCBY license-open access	[3]	-
A2	CCBY license-open access	[3]	-
A3	CCBY license-open access	[2]	-

Tables			
1	CCBY license-open access	-	-
2	-	-	※
3	CCBY license-open access	[2]	-
4	-	-	※
5	5993600503458	-	-
6	CCBY license-open access	[3]	-
7	CCBY license-open access	[3]	-
8	CCBY license-open access	[3]	-
9	CCBY license-open access	[3]	-
10	CCBY license-open access	[2]	-
11	CCBY license-open access	[2]	-
12	-	-	※
13	-	-	※

This page is intentionally left blank.

List of Abbreviations

GDE	Gas Diffusion Electrode
MPL	Microporous Layer
FE	Faradaic Efficiency
CCU	Carbon Capture and Utilization
OER	Oxygen Evolution Reaction
E^0	Standard Electrode Potential
z	Number of electrons needed for the reaction
HER	Hydrogen Evolution Reaction
GDL	Gas Diffusion Layer
PTFE	Polytetrafluoroethylene
LSV	Linear Sweep Voltammetry
MEA	Membrane Electrode Assembly
CD	Current Density
AEM	Anion Exchange Membrane
CEM	Cation Exchange Membrane
DFAP	Direct Formic Acid Production
SEM	Scanning Electron Microscopy
XCT	X-Ray Computer Tomography
TGA	Thermal Gravimetric Analysis
ICP-MS	Inductively Coupled Plasma Mass Spectrometry
WE	Working Electrode
RE	Reference Electrode
CE	Counter Electrode
RHE	Reversible Hydrogen Electrode
GC	Gas Chromatography
IEC	Ion Exchange Chromatography
CCB	Cation Conducting Binders
ACB	Anion Conducting Binders

This page is intentionally left blank.

List of Figures

Figure 1. Carbon Capture and Utilisation technologies for the valorisation of the greenhouse gas CO_2. Reproduced from [10] with permission from Elsevier. 2
Figure 2. The number of articles published between 2010 and 2022 investigating suitable electrode- and cell designs. The following keywords were used by the authors of the article to review the data in the Scopus Database: CO_2 reduction, electrode- and cell design. Reproduced from [25] enabled by the Creative Commons CC-BY license (https://creativecommons.org/licenses/by/4.0/). 3
Figure 3. Elements active for the CO_2 electroreduction in a cropped periodic table. Elements in blue are active for CO_2-to-CO, green for CO_2-to-HCOOH, and grey for the CO_2-to-C_{2+} product fraction. In pink is the HER active group. Figure 3 is adapted from reference [30] and reproduced with permission from Wiley. 7
Figure 4. Schematic representation of the investigated gas diffusion electrodes (GDEs) based on a commercial gas diffusion layer (GDL). Reproduced from [3], enabled by the Creative Commons CC-BY license (https://creativecommons.org/licenses/by/4.0/). 12
Figure 5. Schematic illustration of the reaction conditions at the investigated gas diffusion electrodes (GDEs) surface, displaying an enlarged depiction as an inset. (a) GDE with a microporous layer (MPL) that leads to a focused catalyst layer on the GDE surface. (b) GDE without MPL, thus, missing physical barrier for the catalyst nanoparticles (SnO_2, shown in yellow colour) during the GDE manufacturing. Reproduced from [1], enabled by the Creative Commons CC-BY license (https://creativecommons.org/licenses/by/4.0/). 13
Figure 6. Schematic depiction of a GDE with two representative operating states during CO_2 electroreduction: unoptimised (top) and optimised (bottom). The schematic is reused from [106] with permission from Elsevier. 17
Figure 7. Representation of structural changes on the GDE during operation. (a) Pristine GDE state at t = 0, and final states showcasing deterioration by (b) chemical changes occurring at the catalyst, (c) catalyst agglomeration, (d) carbonate formation – depicted in brown colour, and (e) binder thinning. Reproduced from [1], enabled by the Creative Commons CC-BY license (https://creativecommons.org/licenses/by/4.0/). 20
Figure 8: Illustrations of the cell set-up of the semi-continuous batch cell used in this dissertation: FlexCell PTFE, Gaskatel, Germany, a) Exterior view and b) Cross-section.[137] 24
Figure 9. Possible cell setups for the electroreduction of CO_2 to formate/formic acid. a) H-cell, b) zero gap, c) anion exchange membrane (AEM) free flow cell, d) the direct acid formic production (DFAP) flow cell (water-fed). Figure 8 a reproduced from [136] under permission from RSC, Figure 9 b - d reproduced from [1], enabled by the Creative Commons CC-BY license (https://creativecommons.org/licenses/by/4.0/). 25
Figure 10. Schematic illustration of the foil thickness gauge used for the determination of the electrical through-plane conductivity. Reproduced from [3], enabled by the Creative Commons CC-BY license (https://creativecommons.org/licenses/by/4.0/). 33
Figure 11. Schematic illustration of the experimental setup: test cell (FlexCell PTFE, Gaskatel, Germany), online GC and offline IC. Reproduced from [3], enabled by the Creative Commons CC-BY license (https://creativecommons.org/licenses/by/4.0/). 35
Figure 12. Illustrations of the flow cell set-up (ElyFlow PTFE, Gaskatel, Germany) used in this dissertation. a) Cross section view [148] and b) the additional Ti plate, which is placed between the WE holder and analyte room 1. 36
Figure 13. Procedure for the electrochemical characterisation of the investigated gas diffusion electrodes (GDEs). “Before” each electrolysis run, induced by a chronopotentiometric program step (CP), each GDE is subjected to the full set of analysis techniques, i.e., OCV, CA, PEIS, (3x CV) and 3x LSV, shown in the top line of the schematic. Reproduced from [2], enabled by the Creative Commons CC-BY license (https://creativecommons.org/licenses/by/4.0/). 37

Figure 14. SEM images of the Toray-based pristine gas diffusion layers (GDLs) and the gas diffusion electrodes (GDEs) before and after use. Images for: a-c) TP-060 (10%), d-f) TP-120 (10%), g-i) TP-060 (30%), j-l) TP-060 (30%) MPL, m)-o) TP-120 (30%) and p)-r) TP-120 (30%) MPL. a), d), g), j), p) Pristine GDLs (without catalyst). b), e), h), k), n), q) GDEs before electrochemical testing. c), f), i), l), o), r) GDEs after electrochemical testing. Reproduced from [3], enabled by the Creative Commons CC-BY license (https://creativecommons.org/licenses/by/4.0/). 45
Figure 15.SEM images of the Freudenberg-based pristine gas diffusion layers (GDLs) and the gas diffusion electrodes (GDEs) before and after use. Images for: a-c) FB-E20H, d-f) FB-H23C2, g-i) FB-H23C3, j-l) FB-H23C6, g)-i) FB-H24C5. a), d), g), j), m) Pristine GDLs (without catalyst). b), e), h), k), n) GDEs before electrochemical testing. c), f), i), l), o) GDEs after electrochemical testing. 46
Figure 16. EDX maps for Toray Carbon Paper and Freudenberg a-b) TP-060 (30%), c-d) TP-060 MPL (30%), e-f) TP-120 (30%), g-h) TP-120 MPL (30%), i-l) FB-H23C2, j-m) FB-H23C6, k-n) FB-E20H, before (left) and after CO_2 electroreduction (right). Green/Purple colour identifies Sn. Partly reproduced from [3], enabled by the Creative Commons CC-BY license (https://creativecommons.org/licenses/by/4.0/). 47
Figure 17. Exemplary XCT images of the investigated gas diffusion electrodes (GDEs) after CO_2 electroreduction. The yellow colour indicates regions with a high Sn mass density, i.e., SnO_2 as a part of the catalyst layer vs. the carbon-based substrate. a-b) Side and top view for TP-120 (30%), c-d) Side and top view for TP-120 MPL (30%). (More details in the Videos via the QR code). Reproduced from [3], enabled by the Creative Commons CC-BY license (https://creativecommons.org/licenses/by/4.0/). 48
Figure 18. Exemplary Nyquist plots derived from PEIS measurements in the FlexCell. a) TP-120 (10%) prior to the CO_2 electroreduction. R1 – R3 denote the internal resistance of the whole setup as reported in **Table 9**, resulting from the conductivity of the electrolyte and the GDE-related contributions. b) Reference experiment on a silver plate at various electrode potentials. Reproduced from [3], enabled by the Creative Commons CC-BY license (https://creativecommons.org/licenses/by/4.0/). 56
Figure 19. Evaluation of the current density at −1.15 V_{RHE} (iR-drop corrected) for the third of three LSV-scans prior to each electrolysis runs (Run 1-3). Results for the gas diffusion electrodes (GDEs) without microporous layer (MPL) are shown in green. Results for the GDEs with MPL are shown in red. The results for the reference electrode by Dioxide Materials is shown in black. (Additional details about the LSV-scans can be found in Figures S12. Error bars indicate the estimated standard deviation). Partially reproduced from [3], enabled by the Creative Commons CC-BY license (https://creativecommons.org/licenses/by/4.0/).....59
Figure 20. Evaluation of the avr. electrode potential and the resulting FE for CO_2 electroreduction to formate, H_2 and CO at different current densities ranging from –36 to –107 $mA{\cdot}cm^{-2}$. Results for the gas diffusion electrodes (GDEs) without microporous layer (MPL) are shown in green. Results for the GDEs with MPL are shown in red. Results for the reference electrode by Dioxide Materials are shown in black. a) Avr. electrode potential during 45 min of continuous CO_2 electroreduction. b) Avr. electrode potentials vs. corresponding FE for formate (Interval: 2 – 11 min). c-i) Faradaic efficiencies for formate, H_2 and CO at different current densities ranging from –36 to –107 $mA{\cdot}cm^{-2}$ (Interval: 2 – 11 min). Error bars indicate the estimated standard deviation of a typical experiment. Partly reproduced from [3], enabled by the Creative Commons CC-BY license (https://creativecommons.org/licenses/by/4.0/).....61
Figure 21. Effect of the gas diffusion layer (GDL) on the final concentration of format in the catholyte after 45 min of CO_2 electroreduction. a-g) Final concentration of formate at different current densities ranging from –36 to –107 $mA{\cdot}cm^{-2}$. h) Evolution of the final concentration depending on the resulting electrode potential. Partly reproduced from [3], enabled by the Creative Commons CC-BY license (https://creativecommons.org/licenses/by/4.0/). 69
Figure 22. Schematic illustration of the reaction conditions on the investigated gas diffusion electrodes (GDEs) in this dissertation. a) GDE with a microporous layer (MPL) that leads to a focused catalyst layer on the GDE surface. b) GDE without MPL, thus, missing physical barrier for

the catalyst nanoparticles (SnO_2, shown yellow) during the GDE manufacturing. c) Detailed schematic for the reaction interface of a GDE with MPL and a catholyte. (Most catalyst nanoparticles are in contact with the catholyte.) d) Detailed schematic for the reaction interface of a GDE without MPL and a catholyte. (In this case, some nanoparticles are lost for the reaction since they are not in contact with the catholyte.) Reproduced from [3], enabled by the Creative Commons CC-BY license (https://creativecommons.org/licenses/by/4.0/). 70
Figure 23. Influence of the catalyst loading on the avr. electrode potential for three different applied current densities (36, 71, and 107 $mA \cdot cm^{-2}$. Measurement conditions: batch reactor, 12 ml electrolyte, 1 M $KHCO_3$, continuous CO_2 supply of 20 $ml \cdot min^{-1}$, start at room temperature, electrolysis time: 45 min each). Reproduced from [2], enabled by the Creative Commons CC-BY license (https://creativecommons.org/licenses/by/4.0/). 73
Figure 24. Influence of the catalyst loading on the FE for formate after a run time of 11 min each. (Measurement conditions: batch reactor, 12 ml electrolyte, 1 M $KHCO_3$, continuous CO_2 supply of 20 $ml \cdot min^{-1}$, start at room temperature, electrolysis time: 45 min each). Reproduced from [2], enabled by the Creative Commons CC-BY license (https://creativecommons.org/licenses/by/4.0/). 75
Figure 25. Influence of the catalyst loading (a) and the binder content (b) at the FE of the evolving products. (Catalyst loading: 2.3 $mg \cdot cm^{-2}$, measurement conditions: batch reactor, 12 ml electrolyte, 1 M $KHCO_3$, continuous CO_2 supply of 20 $ml \cdot min^{-1}$, start at room temperature, electrolysis time: 45 min each). Reproduced from [2], enabled by the Creative Commons CC-BY license (https://creativecommons.org/licenses/by/4.0/). 76
Figure 26. Graphical representation of the influence of the avr. electrode potential on the obtained FE for formate. Created from the data in Figures 20 and 21. Reproduced from [2], enabled by the Creative Commons CC-BY license (https://creativecommons.org/licenses/by/4.0/). 76
Figure 27. (a) Exemplary course of the linear sweep voltammograms (LSVs) for the GDE with a catalyst loading of 13 $mg \cdot cm^{-2}$. (b) Evaluation of the cathodic current density at –1.15 V_{RHE} depending on the catalyst loading. (Measurement conditions: batch reactor, 12 ml electrolyte, 1 M $KHCO_3$, continuous CO_2 supply of 20 $ml \cdot min^{-1}$, start at room temperature, electrolysis time: 45 min each). Reproduced from [2], enabled by the Creative Commons CC-BY license (https://creativecommons.org/licenses/by/4.0/). 78
Figure 28. (a) Evaluation of the cathodic current density at –1.15 V_{RHE} to determine the influence of repeated cycling on the GDE stability for a GDE catalyst loading of 2.3 and 13 $mg \cdot cm^{-2}$. (b) Comparison of the avr. electrode potential for three current densities (36, 71 and 107 $mA \cdot cm^{-2}$). (Measurement conditions: batch reactor, 12 ml electrolyte, 1 M $KHCO_3$, continuous CO_2 supply of 20 $ml \cdot min^{-1}$, start at room temperature, electrolysis time: 45 min each). Reproduced from [2], enabled by the Creative Commons CC-BY license (https://creativecommons.org/licenses/by/4.0/). 79
Figure 29. FE of formate after a run time of 11 min each obtained from the CO_2 electroreduction reaction shown in Figure 25. (Measurement conditions: batch reactor, 12 ml electrolyte, 1 M $KHCO_3$, continuous CO_2 supply of 20 $ml \cdot min^{-1}$, start at room temperature, electrolysis time: 45 min each). Reproduced from [2], enabled by the Creative Commons CC-BY license (https://creativecommons.org/licenses/by/4.0/). 80
Figure 30. SEM images of the investigated GDEs concerning the influence of the catalyst loading before the electroreduction of CO_2 at 550x magnification, a) Freudenberg E20H GDL, b) 1.1 $mg \cdot cm^{-2}$, c) 1.3 $mg \cdot cm^{-2}$, d) 2.3 $mg \cdot cm^{-2}$, e) 4.2 $mg \cdot cm^{-2}$, f) 5.8 $mg \cdot cm^{-2}$, g) 13 $mg \cdot cm^{-2}$. Reproduced from [2], enabled by the Creative Commons CC-BY license (https://creativecommons.org/licenses/by/4.0/). 81
Figure 31. SEM images of the investigated GDEs concerning the influence of the catalyst loading after the first cycle electroreduction of CO_2 at 550x magnification, a) 1.1 $mg \cdot cm^{-2}$, b) 1.3 $mg \cdot cm^{-2}$, c) 2.3 $mg \cdot cm^{-2}$, d) 4.2 $mg \cdot cm^{-2}$, e) 5.8 $mg \cdot cm^{-2}$, f) 13 $mg \cdot cm^{-2}$. Reproduced from [2], enabled by the Creative Commons CC-BY license (https://creativecommons.org/licenses/by/4.0/). 82

Figure 32. SEM cross sections of the investigated GDEs (catalyst loading > 2.3 $mg \cdot cm^{-2}$) concerning the influence of the catalyst loading in the pristine state and after the first cycle electroreduction of CO_2 at 250x magnification, a),d) 4.2 $mg \cdot cm^{-2}$, b), e) 5.6 $mg \cdot cm^{-2}$ and c), f) 13 $mg \cdot cm^{-2}$. For a better visualisation, the fracture edges and the catalyst layer are labelled as edges and SnO_2, respectively, as well as arrows indicating the catalyst in the deeper layers. Reproduced from [2], enabled by the Creative Commons CC-BY license (https://creativecommons.org/licenses/by/4.0/). 83
Figure 33. SEM images of the investigated GDEs after repeated cycling: (a) 2.3 $mg \cdot cm^{-2}$ and (b) 13 $mg \cdot cm^{-2}$.Reproduced from [2], enabled by the Creative Commons CC-BY license (https://creativecommons.org/licenses/by/4.0/). 84
Figure 34. Raman spectra for the investigated GDEs before and after CO_2 electroreduction with a catalyst loading of (a) 2.3 $mg \cdot cm^{-2}$ and (b) 13 $mg \cdot cm^{-2}$. (Incident wavelength: 532 nm, spectra normalised to the highest vibration). Reproduced from [2], enabled by the Creative Commons CC-BY license (https://creativecommons.org/licenses/by/4.0/). 85
Figure 35. Vapor sorption measurements of GDEs with different catalyst loadings: a) 1.1 $mg \cdot cm^{-2}$ and b) 1.3 $mg \cdot cm^{-2}$, c) 4.2 $mg \cdot cm^{-2}$ and d) 5.8 $mg \cdot cm^{-2}$. Vapor adsorption isotherms of the investigated GDEs in different states – pristine and after cycle 1. Vapor sorption measurements were conducted at 25°C with a relative humidity from 0 to 80%, each humidity point was held for 60 min. Negative values are a result of the device uncertainty, common for a small amount of sample with limited adsorption. Reproduced from [2], enabled by the Creative Commons CC-BY license (https://creativecommons.org/licenses/by/4.0/). 87
Figure 36. Thermogravimetric analysis (TGA) of the GDEs before and after electroreduction experiments at catalyst loadings of (c) 2.3 $mg \cdot cm^{-2}$ and (d) 13 $mg \cdot cm^{-2}$. TGA was carried out from room temperature to 1200°C with a heating rate of 10 $K \cdot min^{-1}$ in oxygen environment. Reproduced from [2], enabled by the Creative Commons CC-BY license (https://creativecommons.org/licenses/by/4.0/). 89
Figure 37. Thermogravimetric analysis (TGA) of the GDEs before and after electroreduction experiments at catalyst loadings of (a) 2.3 $mg \cdot cm^{-2}$ and (b) 13 $mg \cdot cm^{-2}$ in the cut out of 70 – 100wt%. TGA was carried out from room temperature to 1200°C with a heating rate of 10 $K \cdot min^{-1}$ in oxygen environment. Reproduced from [2], enabled by the Creative Commons CC-BY license (https://creativecommons.org/licenses/by/4.0/). 90
Figure 38. Evaluation of the cathodic current density at −1.15 V_{RHE} depending on the different binder types: a) cation conducting binder (CCB) and b) anion conducting binder (ACB). The bold lines represent Cycle 1, and the dashed lines Cycle 2. (Measurement conditions: batch reactor, 12 ml electrolyte, 1 M $KHCO_3$, continuous CO_2 supply of 20 $ml \cdot min^{-1}$, start at room temperature, electrolysis time: 45 min each).....93
Figure 39. Evaluation of the avr. electrode potential depending on the different binder types: a) CCB and b) ACB for three current densities (36, 71 and 107 $mA \cdot cm^{-2}$). The bold lines represent Cycle 1, and the dashed lines represent Cycle 2. (Measurement conditions: batch reactor, 12 ml electrolyte, 1 M $KHCO_3$, continuous CO_2 supply of 20 $ml \cdot min^{-1}$, start at room temperature, electrolysis time: 45 min each).....94
Figure 40. Faradaic efficiencies for formate, H_2 and CO at different current densities ranging from –36 to –107 $mA \cdot cm^{-2}$ repeated cycling. Error bars indicate the estimated standard deviation of a typical experiment. Catalyst loading: 2.3 $mg \cdot cm^{-2}$, measurement conditions: batch reactor, 12 ml electrolyte, 1 M $KHCO_3$, continuous CO_2 supply of 20 $ml \cdot min^{-1}$, start at room temperature, electrolysis time: 45 min each. 96
Figure 41. SEM images of the investigated GDEs in dependence of the binder in the pristine state: a) Aquivion, b) Nafion, c) Aemion+Nafion, d) Aemion, e) Sustainion, f) Fumion, g) Piperion, and h) Pention. 98
Figure 42. Exemplary SEM images of the investigated GDEs in dependence of the binder type after cycle 2. a) Aquivion (after cycle 1), b) Nafion, c) Aemion+Nafion, d) Aemion, e) Sustainion, f) Fumion, g) Piperion, and h) Pention. 99

Figure 43. Raman spectra for the investigated GDEs before and after CO_2 electroreduction, as well as the respective binder used: a) Aquivion, b) Nafion, c) Aemion + Nafion, d) Aemion, e) Sustainion, f) Fumion, g) Piperion and h) Pention. (Incident wavelength: 532 nm, spectra normalised to the highest vibration).....100
Figure 44. Vapor sorption measurements of GDEs with different binders: a) Aquivion, b) Nafion, c) Aemion+Nafion, d) Aemion, e) Sustainion, f) Fumion, g) Piperion and h) Pention. Vapor adsorption isotherms of the investigated GDEs in different states – pristine and after cycle 2...105
Figure 45. Flow cell measurements with Sustainion as binder: obtained FEs for Formate, H_2 and CO during the current density screening in ElyFlow setup (36 to 107 $mA \cdot cm^{-2}$). Measurement conditions: GDE (2.3 $mg \cdot cm^{-2}$ catalyst loading, Sustainion as binder, FB-H23C3 GDL), electrolyte single-flow modus 10 $ml \cdot min^{-1}$, 1 M $KHCO_3$, continuous CO_2 supply of 55 sccm (36 and 71 $mA \cdot cm^{-2}$) and 85 sccm (107 $mA \cdot cm^{-2}$)., start at room temperature, electrolysis time: 30 min each. 107
Figure 46. Influence of MPL loading on a) the obtained FE of formate. Respective SEM image of the MPL loading b) 1.6 $mg.cm^{-2}$ before and c) after electroreduction of CO_2 showing a peeling of the catalyst layer due to too high MPL loading. Measurement conditions: batch reactor, 12 ml electrolyte, 1 M $KHCO_3$, continuous CO_2 supply of 20 $ml \cdot min^{-1}$, start at room temperature, electrolysis time: 45 min each.....108
Figure 47. Influence of the repeated cycling in two different cell setups: a) Comparison of the avr. electrode potential for three different current densities (36, 71, and 107 $mA \cdot cm^{-2}$) and b) FE of formate obtained after a run time of 11 min each. (Measurement conditions: batch reactor, 12 ml electrolyte, 1 M $KHCO_3$, continuous CO_2 supply of 20 $ml \cdot min^{-1}$, start at room temperature, electrolysis time: 45 min each, flow cell: electrolyte in single flow modus 10 $ml \cdot min^{-1}$, 1 M $KHCO_3$, continuous CO_2 supply of 300 $ml \cdot min^{-1}$, start at room temperature, electrolysis time 35 min each).....109
Figure 48. Current Density Screening in ElyFlow setup from 36 to 360 $mA \cdot cm^{-2}$, a) avr. electrode potential and b) resulting FE. 110
Figure 49. 6-hour electrolysis at 160 $mA \cdot cm^{-2}$: a) obtained electrode potential and b) obtained FEs of formate, H_2 and CO. (Measurement conditions: flow cell: electrolyte flow 20 $ml \cdot min^{-1}$, 1 M $KHCO_3$, continuous CO_2 supply of 300 $ml \cdot min^{-1}$, start at room temperature, electrolysis time 6 hours). 111
Figure 50. SEM images of the investigated GDEs: (a) pristine GDE, after repeated cycling in (b) the batch cell and (c) the flow cell, as well as d) after 6 hours of CO_2 electroreduction. 112

Figure A 1: All LSV-scans for the investigated GDEs. Partly reproduced from [3], enabled by the Creative Commons CC-BY license (https://creativecommons.org/licenses/by/4.0/). 132
Figure A 2. Potential vs. Time curves during each 45 min CO_2-electrolysis run at current densities ranging from –36 to –107 $mA \cdot cm^{-2}$, a)-c) Toray Carbon Paper GDLs and d)-f) Freudenberg GDLs. Partly reproduced from [3], enabled by the Creative Commons CC-BY license (https://creativecommons.org/licenses/by/4.0/). 133
Figure A 3. Thermogravimetric analysis of pure Nafion polymer dispersion (15 wt%), the Freudenberg E20H GDL and the Freudenberg E20H GDL coated with Nafion and immersed in $KHCO_3$ for 7 days. TGA was carried out from room temperature to 1200°C with a heating rate of 10 $K \cdot min^{-1}$, in oxygen environment. Reproduced from [2], enabled by the Creative Commons CC-BY license (https://creativecommons.org/licenses/by/4.0/). 134

List of Tables

Table 1. List of CO_2 electroreduction products with their respective cathode reaction, number of electrons exchanged (z) and standard reaction potential (E^0). E^0 values are reported in aqueous media under standard conditions: 1 atm and 25°C.[32] 8
Table 2. Overview of the investigated gas diffusion layers (GDLs, TP = Toray Paper Industries, FB = Freudenberg GmbH) either with (w) or without (w/o) microporous layer (MPL) and with (w) or without (w/o) hydrophobic treatment. The hydrophobic treatment for Toray Papers was either 10% or 30% PTFE related to the carbon fibre substrate. 28
Table 3. Investigated catalyst loadings and the corresponding weight of catalyst and binder (in the ratio: 90:10wt%). Reproduced from [2], enabled by the Creative Commons CC-BY license (https://creativecommons.org/licenses/by/4.0/) 29
Table 4. Overview of the investigated ionomer types as binders for the gas diffusion electrodes. 30
Table 5: Types and structural formulas of the investigated binders. Reused from [147] with permission from Elsevier. 30
Table 6: Comparison of the contact angles (1M $KHCO_3$) for pristine GDLs, GDLs with Nafion coating only and GDEs before and after CO_2 electroreduction. Contact angle measurements were performed using 1 M $KHCO_3$ electrolyte at room temperature. (Scattering of measurement results represents the standard deviation for the contact angle.) Partly reproduced from [3], enabled by the Creative Commons CC-BY license (https://creativecommons.org/licenses/by/4.0/). 50
Table 7. Results for the porosity measurements of the pristine GDLs and the GDEs before and after the CO_2 electroreduction. (Scattering of measurement results represents the estimated standard deviation for the mean flow pore diameter measurement (±10%).) Partly reproduced from [3], enabled by the Creative Commons CC-BY license (https://creativecommons.org/licenses/by/4.0/) 52
Table 8: Results for the through-plane conductivity measurements of the pristine GDLs and the GDEs before and after the CO_2 electroreduction. (Scattering of measurement results represents the standard deviation for through-plane conductivity measurements). Reproduced from [3], enabled by the Creative Commons CC-BY license (https://creativecommons.org/licenses/by/4.0/). 54
Table 9. Results of the internal resistance measurement by PEIS as conducted prior to every electrolysis run (Figure S4) in fresh 1 M $KHCO_3$ at room temperature. (Standard deviation based on estimates (± 10%)). Partly reproduced from [3], enabled by the Creative Commons CC-BY license (https://creativecommons.org/licenses/by/4.0/) 57
Table 10. Comparison of the contact angles (1M $KHCO_3$) for pristine GDL and GDEs to the GDL with Nafion coating only and change of contact angle and of the investigated GDEs as a function of the catalyst loading before and after cycle 1 and cycle 2. (Scattering represents the standard deviation). Reproduced from [2], enabled by the Creative Commons CC-BY license (https://creativecommons.org/licenses/by/4.0/) 86
Table 11. Result of the thermogravimetric analysis (TGA) for two gas diffusion electrodes (GDEs) with a catalyst loading of 2.3 and 13 $mg \cdot cm^{-2}$ before and after CO_2 electroreduction. Reproduced from [2], enabled by the Creative Commons CC-BY license (https://creativecommons.org/licenses/by/4.0/) 89
Table 12. Investigation of the influence of the implemented binder on the contact angle of the respective GDEs before and after the electroreduction of CO_2 and GDLs coated only with the respective binders. (Scattering represents the standard deviation). 103
Table 13. Results of the ICP-MS measurements determining the amount of catalyst lost during the electroreduction of CO_2. 111

Curriculum Vitae

Personal Data

Name	Verena Theußl
E-Mail	verena.theussl@gmx.at
Date of Birth	23rd February 1994
Place of Birth	Deutschlandsberg
Citizenship	Austrian

Education

3/2020 – Dissertation at Institute of Energie and Climate Research – Fundamental Electrochemistry (IEK-9, now IET-1), Forschungszentrum Jülich, Chair of material and processes of electrochemical energy storage and conversion, RWTH Aachen University, Germany.

3/2016 – 10/2019 Masters programme Technical Chemistry, Graz University of Technology, Graz, Austria.

3/2017 – 08/2017 Erasmus+, Masters programme Materia Chemistry, Universität des Saarlandes, Saarbrücken, Germany

0/2012 – 03/2016 Bachelor programme Chemstry, Graz University of Technology, Graz, Austria.

9/2008 – 07/2012 BORG Deutschlandsberg, High School with focus on natural science, Deutschlandsberg, Austria.

Work Experience

5/2024 – Forschungszentrum Jülich, Institute of Energy Technologies – Electrochemical Process Engineering (IET-4), Jülich, Germany.

3/2020 – 02/2024 Forschungszentrum Jülich, Institute of Energy and Climate Research – Fundamental Electrochemistry (IEK-9, now IET-1), Jülich, Germany.

8/2019 – 09/2019 Universidad Tecnológica Nacional, Facultad Regional Córdoba, Centro de Investigación y Transferencia en Ingenería Química Ambiental (CIQA), Cordoba, Argentina.

7/2018 – 07/2019 Graz University of Technology, Institute for Chemistry and Technology of Materials, Graz, Austria.

5/2016 – 01/2017 University of Graz, Institute for Physical and Theoretical Chemistry.